NUMERICAL INVESTIGATION ON THE ACOUSTIC IMAGING OF THE HUMAN RESPIRATORY SYSTEM AND MANUFACTURING OF THE SYNTHETIC EXPERIMENTAL MODEL

A THESIS SUBMITTED TO
THE GRADUATE SCHOOL OF NATURAL AND APPLIED SCIENCES
OF
MIDDLE EAST TECHNICAL UNIVERSITY

BY

FURKAN GINAZ ALMUS

IN PARTIAL FULFILLMENT OF THE REQUIREMENTS
FOR
THE DEGREE OF MASTER OF SCIENCE
IN
MECHANICAL ENGINEERING

AUGUST 2022

Approval of the thesis:

NUMERICAL INVESTIGATION ON THE ACOUSTIC IMAGING OF THE HUMAN RESPIRATORY SYSTEM AND MANUFACTURING OF THE SYNTHETIC EXPERIMENTAL MODEL

submitted by **FURKAN GINAZ ALMUS** in partial fulfillment of the requirements for the degree of **Master of Science in Mechanical Engineering Department, Middle East Technical University** by,

Prof. Dr. Halil Kalıpçılar
Dean, Graduate School of **Natural and Applied Sciences** ______________

Prof. Dr. M. A. Sahir Arıkan
Head of Department, **Mechanical Engineering** ______________

Assoc. Prof. Dr. Mehmet Bülent Özer
Supervisor, **Mechanical Engineering, METU** ______________

Examining Committee Members:

Prof. Dr. Yiğit Yazıcıoğlu
Mechanical Engineering, METU ______________

Assoc. Prof. Dr. Mehmet Bülent Özer
Mechanical Engineering, METU ______________

Assoc. Prof. Dr. Ender Yıldırım
Mechanical Engineering, METU ______________

Assist. Prof. Dr. Altuğ Özçelikkale
Mechanical Engineering, METU ______________

Assist. Prof. Dr. Hüseyin Enes Salman
Mechanical Engineering, TOBB ETU ______________

Date: 26.08.2022:

I hereby declare that all information in this document has been obtained and presented in accordance with academic rules and ethical conduct. I also declare that, as required by these rules and conduct, I have fully cited and referenced all material and results that are not original to this work.

Name, Surname: Furkan Ginaz Almus

Signature :

ABSTRACT

NUMERICAL INVESTIGATION ON THE ACOUSTIC IMAGING OF THE HUMAN RESPIRATORY SYSTEM AND MANUFACTURING OF THE SYNTHETIC EXPERIMENTAL MODEL

Almus, Furkan Ginaz
M.S., Department of Mechanical Engineering
Supervisor: Assoc. Prof. Dr. Mehmet Bülent Özer

August 2022, 139 pages

It is well known that physiological changes and diseases in the respiratory system affect the sound waves that form and propagate in the human body. The characteristics of these sound waves, such as frequency, amplitude, and phase, can contain critical and unique information about physiological changes and disorders. In this study, we aim to obtain a numerical model of the human respiratory system that can be used to understand the generation and propagation of acoustic waves within the human thorax and to employ acoustic imaging methods for the diagnosis of lung and respiratory system diseases. Two fundamental acoustic imaging methods, Conventional Beamformer and Matched-Field Processor have been used on the model with an exact geometry of the human respiratory system for the first time in the literature. The realistic numerical model of the human thorax has been obtained by processing the open-source Computed Tomography images through Materialise Mimics, which is a commercial image processing software. Acoustic imaging methods have been primarily investigated using the simple two-dimensional model, and findings were verified using the simple three-dimensional model and realistic numerical model. According to the literature, the selection of the steering vector is crucial in terms of the perfor-

mance of the Conventional Beamformer. Therefore, we have examined four different steering vector formulations using the two-dimensional model. Also, we have evaluated the performances of the two different Matched-Field Processors using the same model. After comparing the different steering vector formulations and processors, we have applied the most robust and successful ones considering the localization results of the abnormal region within the lung to the simple three-dimensional and realistic numerical models. Numerical analyses of the models were performed using a finite element software, COMSOL Multiphysics. In addition to numerical investigation, the manufacturing methodology and process of the synthetic experimental respiratory system model that can be used for experimental validation have been presented.

Keywords: Acoustic Imaging of Human Respiratory System, Numerical Analysis, Synthetic Experimental Model

ÖZ

İNSAN SOLUNUM SİSTEMİNİN AKUSTİK GÖRÜNTÜLEMESİNİN SAYISAL İNCELENMESİ VE SENTETİK DENEYSEL MODELİN ÜRETİMİ

Almus, Furkan Ginaz
Yüksek Lisans, Makina Mühendisliği Bölümü
Tez Yöneticisi: Doç. Dr. Mehmet Bülent Özer

Ağustos 2022 , 139 sayfa

Solunum sistemindeki fizyolojik değişikliklerin ve hastalıkların insan vücudunda oluşan ve yayılan ses dalgalarını etkilediği iyi bilinmektedir. Bu ses dalgalarının frekans, genlik ve faz gibi özellikleri fizyolojik değişiklikler ve bozukluklar hakkında kritik ve benzersiz bilgiler içerebilir. Bu çalışmada, insan göğüs kafesi içerisindeki akustik dalgaların oluşumunu ve yayılımını anlamak için kullanılabilecek insan solunum sisteminin sayısal bir modelini elde etmeyi ve akciğer ve solunum sistemi hastalıklarının teşhisi için akustik görüntüleme yöntemlerini kullanmayı amaçlıyoruz. Literatürde ilk kez insan solunum sisteminin tam bir geometrisine sahip modelde iki temel akustik görüntüleme yöntemi olan Konvansiyonel Hüzme Oluşturucu ve Eşleştirilmiş Alan İşlemcisi bu çalışmanın kapsamında uygulanmıştır. Açık kaynaklı Bilgisayarlı Tomografi görüntüleri ticari bir görüntü işleme yazılımı olan Materialize Mimics ile işlenerek insan göğüs kafesinin gerçekçi sayısal modeli elde edilmiştir. Akustik görüntüleme yöntemleri öncelikle basit iki boyutlu model kullanılarak araştırılmış ve bulgular basit üç boyutlu model ve gerçekçi sayısal model kullanılarak doğrulanmış-

tır. Literatüre göre, Konvansiyonel Hüzme Oluşturucunun performansı açısından yönlendirme vektörünün seçimi çok önemlidir. Bu nedenle, iki boyutlu modeli kullanarak dört farklı yönlendirme vektörü formülasyonunu inceledik. Ayrıca, aynı modeli kullanan iki farklı Eşleştirilmiş Alan İşlemcisinin performanslarını değerlendirdik. Farklı yönlendirme vektör formülasyonları ve işlemcileri karşılaştırdıktan sonra, akciğer içindeki anormal bölgenin lokalizasyon sonuçlarını göz önünde bulundurarak en başarılı ve tutarlı olanları basit üç boyutlu ve gerçekçi sayısal modellere uyguladık. Modellerin sayısal analizleri, sonlu eleman yazılımı olan COMSOL Multiphysics kullanılarak gerçekleştirilmiştir. Ayrıca deneysel doğrulama için kullanılabilecek sentetik bir deneysel solunum sistemi modelinin üretim metodolojisi ve süreci sunulmuştur.

Anahtar Kelimeler: İnsan Solunum Sisteminin Akustik Görüntülenmesi, Sayısal Analiz, Sentetik Deneysel Model

to my family, friends, and all the beautiful songs

ACKNOWLEDGMENTS

I would foremost like to express my endless thanks and deepest gratitude to my advisor, Assoc. Prof. Mehmet Bülent Özer, who guided and helped me throughout my study and never spared his support and efforts.

I would like to express my gratitude to Prof. Dr. Mehmet Çalışkan, Assoc. Prof. Zühre Sü Gül, and my colleagues we worked together in Mezzo Stüdyo for supporting and encouraging me to work in the field of acoustics.

I would like to thank my parents, Meral ve Zeki Almus, and my brother, Alhaz Almus, who have always supported me throughout my life and never stopped believing in me.

I would like to thank my friends, all the people of Cumtıs and Lilith, who taught me how to laugh, have fun, share, and trust. I would also like to express my special thanks to Bertan Kurşun for his valuable feedback on my study.

I would like to thank Btech Innovation Inc., especially Osman Tunç and Beril Demirbakan, for their support and assistance throughout my research.

I would like to thank to Middle East Technical University Scientific Research Fund (METU/BAP) for funding my research (BAP Project No: GAP-302-2022-10846).

TABLE OF CONTENTS

LIST OF TABLES

TABLES

LIST OF FIGURES

FIGURES

LIST OF ABBREVIATIONS

2D	Two-Dimensional
3D	Three-Dimensional
CT	Computed Tomography
MRI	Magnetic Resonance Imaging
US	Ultrasonography
BE	Boundary Element
FE	Finite Element
PTX	Pneumothorax
CB	Conventional Beamformer
MFP	Matched-Field Processor
MVDR	The Minimum Variance Distortionless Response
SPL	Sound Pressure Level

LIST OF SYMBOLS

ω	Radian frequency
u	Particle-fluid velocity
S	Cross-sectional area of the pipe
p	Pressure
ρ	Density
p_0	Ambient pressure
p'	Acoustic pressure
ρ_0	Equilibrium density
ρ'	Fluctuating density
T	Temperature
s	Specific entropy
e	Specific internal energy
B	Bulk modulus
c	Speed of sound
$\mathbf{u_{solid}}$	Displacement vector
σ	Cauchy stress tensor
$\boldsymbol{P}$	First Piola-Kirchoff stress tensor
$\mathbf{J}$	Jacobian operator
$\boldsymbol{S}$	Second Piola-Kirchoff stress tensor
T	Transpose operator
$\mathbf{x_s}$	Position vector
a	Transfer function
$q(t)$	Source strength

$\mathbf{h}$	Steering vector
H	Hermitian operator
k	Wave number
$\mathbf{C}$	Cross-spectral matrix
α	Attenuation
E	Young's modulus
ν	Poisson's ratio
λ	Wavelength

CHAPTER 1

INTRODUCTION

1.1 Motivation of the Study

It is well known that physiological changes and diseases in the respiratory system affect the sound waves that form and propagate in the human body. The characteristics of these sound waves, such as frequency, amplitude, and phase, have been studied in the literature for many years using a variety of procedures, as they can contain critical and unique information about physiological changes and disorders[1]. Several techniques and methods, such as Auscultation, Palpation, and Percussion, have been developed and used in clinical practice as a result of these studies. Auscultation is the earliest technique that has been described and documented in the literature. Auscultation is a practical, effective, and safe procedure that has been used for over 200 years [2], mainly for diagnosing respiratory system illnesses by listening to the noises that occur within the audible frequency range in the body.

While auscultation and other methods are practical and straightforward procedures, they produce more superficial and subjective information when compared to today's imaging technologies such as Computed Tomography (CT), Magnetic Resonance Imaging (MRI) or Ultrasonography (US), which are developed with the advancement of technology and are now more widely utilized for diagnostic purposes. The subjectivity and superficiality of these methods are not surprising; its clear that the inadequacy of the output is related to the nature of the method. For example, the most important thing that determines the performance of the auscultation is the doctor's skill to hear and interpret what they hears. Although these methods are still used for preliminary diagnosis despite these shortcomings, modern imaging techniques are used to get more accurate results and make a definitive diagnosis since they produce more objective, detailed, and quantifiable results; however, they have some drawbacks. For instance, CT can diagnose various lung disorders but exposes the patient to radiation. Although emitted radiation from a one-time CT scan does not carry significant risk, the risk for patients increases with each scan received. US and MRI are much safer when compared with CT, however, they are unable to generate a sufficiently detailed image due to the impedance mismatch between the lung and thorax [3], and high attenuation of ultrasonic sound waves due to the poroviscoelastic structure of parenchyma [4]. Additionally, these imaging techniques are not available worldwide due to their high-costs. Considering these drawbacks, it can be said that it is vital to develop effective, safe, and inexpensive imaging technologies and use them as an alternative to currently used methods.

As previously stated, the ability to give pathologically essential and valuable information on the formation and mechanical propagation of acoustic waves, in other terms sound waves in the range of audible frequency, in the respiratory system promises to develop novel imaging technologies. Thus, utilizing various analytical, numerical, and experimental methods, measuring internally originated or externally introduced acoustic waves with novel hardware and software, and visualizing, interpreting, and verifying acquired data will help develop new imaging techniques and technologies. Our motivation in this study is to understand the sound propagation within the human respiratory system and investigate the potential and limits of acoustic imaging techniques for the diagnosis of the respiratory system diseases.

1.1.1 Diagnostic Motivation

Whether or not we understand how acoustic waves propagate through the thorax, the essential aim is to produce meaningful and objective results and put them into practice that can be utilized in disease diagnostics and treatment. Lung sounds have been extensively studied and classified in the literature [1, 5] and have been used in clinical practice for a long time. However, systematic and quantitative methods, unlike auscultation, which produce objective and detailed results, have not been developed yet.

It is common to generate acoustic images using well-known methods such as acoustic beamforming or acoustic holography over acoustic signal in various applications such as underwater surveillance [6], noise source identification, and improvement of noise characteristics of machines [7] or noise suppression for hearing aid devices [8]. These methods are used to investigate the acoustic behavior of systems and obtain useful information about the specified medium and sound/noise sources. However, there has been little research on the potential of these methods to be used for diagnosing lung diseases considering audible frequency range, not the ultrasonic frequency range. To develop cost-effective, practical, safe, and non-invasive medical imaging technologies, it is critical to examine and discuss these techniques in diagnosing lung disorders and future medical applications.

1.1.2 Motivation of the Synthetic Experimental Model

Human and/or animal trials are the most often used experimental method in the literature [3, 9, 10] for validating the results of analytical and numerical analyses. Most experimental validations involved processing and analyzing acoustic signal data from human and animal bodies measured over the chest region. One could argue that such experimental validation may create inconsistency and limitations for future research. To begin, no information about the subjects' medical histories, lung sizes, fat tissue thickness, or other vital information is available. Uncertainties regarding the subjects' respiratory systems have the ability to alter the obtained results significantly. Another issue is the complexity of human and animal bodies. Vibrations emitted by another organ or breathing process, for example, can readily alter the measurements recorded. Additionally, while the lung volume is assumed to be constant in the simulation models, this assumption is incorrect for the experiment, as subjects must breathe regularly. The other issue is that human subjects are difficult to control and manipulate. Although it is relatively easy to model and assess numerous respiratory disorders such as collapsed lung called pneumothorax (PTX), pulmonary fibrosis, tumor, or pneumonia, in the numerical models, it is impossible to simulate such diseases using human or animal subjects. For instance, one cannot implant a tumor or deflate the subject's lung for experimentation.

The experimental approaches used thus far are insufficient to verify the analytical and numerical results. Verification studies are typically qualitative rather than quantitative when considering the above procedure. Therefore, realistic, synthetic, and controllable experimental models are required to validate the results of analytical and numerical models and perform quantitative and repeatable experiments. Today, additive manufacturing techniques make it possible to create such complicated models. Also, various respiratory system diseases and physiological changes can be more easily modeled, visualized, and evaluated experimentally using 3D printers. Such a synthetic model can help us investigate the formation and propagation of acoustic waves in the pulmonary system and gain significant knowledge for future application in diagnosis/diagnostic purposes.

1.2 Lung Acoustics and Acoustic Diagnostic Techniques

The structure and function of the lungs change due to various conditions such as lung consolidation, pneumothorax, lung tumor, etc., and detectable alterations frequently accompany these changes in sound production and propagation within the human respiratory system. Lung sounds are known to contain spatial and/or spectral information, which can be obtained and observed by taking many acoustic measurements simultaneously at different locations over the chest wall. If acoustic data obtained from multi-sensor recordings are processed and analyzed correctly, the extent and location of trauma to the body or other pathologhy can be determined [11, 12, 13, 14]. While these studies provide preliminary data on acoustic imaging of the human respiratory system, they do not provide a method or technique for performing such imaging.

Kompis et al. [15] published one of the earliest studies on the issue, describing a method for generating a 3D acoustic image of the human chest. His methodology was based on free-field sound propagation via the human respiratory system, assuming a constant sound speed and damping factor per length, and a triangulation method, which relies on the geometric relationship between hypothetical sound sources and microphones, to find the location of sound sources. The results of this early investigation demonstrated that the acoustic images of a subject with lung consolidation were considerably different from those of healthy subjects, indicating that spatial information could be extracted, and abnormalities could be located.

Another attempt for an acoustic imaging method was proposed by Ozer et al. [16]. He proposed Boundary Element (BE) model for sound propagation within the lungs. Results obtained from the sound propagation model revealed and verified the widely-used assumption that compression waves dominate the obtained response and shear waves can be neglected in the frequency range of interest (20-1000 Hz) numerically and experimentally. Then, numerical results were processed for the localization of the monopole sound source using Bartlett's Beamformer, also known as Linear Processor, with the obtained results from the experiment where lung phantom was used as an experimental model. Sound localization results indicated that coupling Bartlett's Beamformer with the BE model produces more accurate results than coupling with the free-field sound propagation model, even when considerable errors are introduced to phase speed and attenuation rate.

Another critical point that can be concluded from Ozer's study was that the acoustic source localization algorithm might be used to identify and localize lung abnormalities if they behave like sound sources. An example of this behavior was shown in Kompis's study [15], where the region with lung consolidation is revealed with high intensity on acoustic images. Henry et al.[17] extended Ozer's study and verified the mentioned conclusion in the case of wheeze, which is the continuous and coarse noise that occurs during breathing due to the regional narrowing of the airways (i.e., asthma). In the study, Bartlett's beamformer accurately predicted the location of the narrowing region of the airway, assuming this region acts as a monopole sound source. Another algorithm was proposed by Salehin et al. [18] for the localization of sound sources that are based on the decomposition of the wavefield into a collection of eigenfunctions. The study's most significant finding was that the frequency of acoustic waves is inversely proportional to the radius of the zone where sound sources can be located. In the literature, there have been other investigations [19, 20, 21, 22] on acoustic lung imaging techniques, but no method that has been employed in this manner for practical or diagnostic purposes has been known as of today.

The studies mentioned above provide promising results about the development of such an acoustic imaging method; however, it is known that more accurate and precise analytical, numerical, and experimental models are required to comprehend mechanical wave propagation through the thorax. In the early attempts at creating those models [15, 16, 23], a human respiratory system that generally consists of the bronchial airway, parenchyma, rib cage, and soft tissue are modeled as simple circular or cylindrical shell-like structures. Considering computational and technical capabilities in those days, modelling complex and realistic analytical or numerical acoustic wave propagation models of the human thorax and producing them for experimentation was not easy.

Although today it is not easy to solve the analytical wave propagation model by considering shear waves in the rib cage and fat tissue, various techniques (such as image processing and numerical analysis techniques) allow us to model the human respiratory system geometrically and the sound propagation within thorax numerically. The most complex part of the human respiratory system can be shown as the bronchial tree. Several analytical models for airway geometry and acoustic propagation through the airway have been proposed over the past few decades, such as Horsfield's airway model [24], but all of these models depend on many assumptions. These assumptions can make it unlikely that models can be used for the dynamic and subject-specified analysis of the human body for diagnostic purposes. Many discussions can be conducted about those assumptions, but probably the most important result would be that subject-specified models are required for such diagnostic techniques. In the last two decades, advanced image-processing algorithms and methods [25, 26, 27] have been proposed for such subject specified geometrical models which can be used with numerical analysis techniques, which are usually generated by processing CT images. It can be said that this kind of modeling approach can enable us to perform subject specified analyses of each organ, system, or whole body.

First time in the literature, Peng et al.[28] developed a complete geometrical model of the human respiratory system (consisting of the bronchial airway, parenchyma, rib cage, soft tissue, and scapulae) using an image processing technique and performed a frequency-domain acoustic analysis of the chest under surface excitation using the Finite Element (FE) Method. Their study has demonstrated, by verifying with human and animal experiments, that such numerical models can be used to examine sound propagation in the thorax. In the following years, similar computational acoustic models of the human respiratory system for different lung cases (e.g., healthy lung, PTX, pulmonary fibrosis, and local tumor) were revealed and studied using the same geometrical modeling approach, and the results were validated using experimental measurements obtained from human and animal subjects [3, 10]. Since these studies [3, 10, 28] share almost the same numerical and experimental methodology, we can summarize their significant results, item by item, as follows:

- Experimental studies [3, 10, 28] showed that the decrease in the transmitted acoustic energy increased as the frequency increased. This can be explained by the fact that the sound attenuation of the parenchyma tissue increases as the frequency increases, which is consistent with previous experimental studies [29].
- Experimental results [28] showed that similar trends were observed across all subject groups and numerical models, although there were significant differences between subjects, such as anatomical and size differences, unknown medical histories, measurement errors due to noise and measurement locations. However, these errors may create significant limitations [3]. Therefore, the effect of these errors on the results and the inter-variability of the subjects should be examined.
- Numerical and experimental studies [3, 10, 28] revealed that at high frequencies (250-1000 Hz) a significant decrease in transmitted acoustic energy is observed in the PTX state compared to the healthy state. At low frequencies (20-250 Hz), there was no significant difference in transmitted acoustic energy between healthy and PTX states. One possible explanation about this observation is that PTX acts as an acoustic barrier to sound waves since the wavelength is small at high frequencies (PTX as filled air between lung tissue and chest wall creates additional impedance mismatch).
- Although the acoustic excitation techniques were different between the studies (one study [28] used surface excitation, the other studies [3, 10] used acoustic insonification), similar trends and results were obtained for the healthy and PTX states. However, Palnitkar's study [3] showed that acoustic insonification is not ideal technique to detect pulmonary fibrosis. Surface excitation provided more significant differences in response between the healthy and fibrosis states. These

studies did not compare the effect of these excitation techniques on the responses of healthy and local tumor states.

- Even similar trends were observed for both excitation techniques, studies [3, 28] showed that compression waves are dominant over the shear waves in the case of airway insonification which is consistent with previous study [30].

1.3 Research Objective

We will begin to our study with simple models and work our way up to more complicated simulation models since our main goal is to investigate the potential use of the acoustic imaging techniques for the human respiratory system, which is a vast and difficult topic. As a result, we may divide the study into four research questions to address the objectives of this study which are listed below:

- What kind of acoustic response will be encountered when different sized abnormal regions are placed on a simple 2D numerical model of the respiratory system, and what output will acoustic imaging techniques provide?
- Can the results obtained from acoustic imaging techniques be used for diagnostic purposes? If they can be used, how and under what conditions?
- Can the results which are obtained from the simulations made with the simple 2D model be verified using the simple and realistic 3D models?
- Can a 3D synthetic experimental model be produced for experimental validation of numerical analysis of exact geometry?

1.4 Contribution of the Thesis

First of all, within the scope of this study, Conventional Beamformer was applied for the first time in the literature to detect the abnormal region(s) in simple and realistic human respiratory models, using the responses obtained from the numerical analysis of these models. Four different steering vectors (used to obtain the inverse of the transfer function), available in the literature, were applied separately for the 2D configuration, and their performances were compared. Conventional Beamformer results showed that this method could be employed to locate the approximate region of the abnormality.

In addition, two different Matched-Field Processors were used on simple and realistic respiratory system models and their performances were compared to detect the location of the abnormality. Linear Processor, which performed better performance among all techniques, was used on a complete numerical model of the human respiratory system for the first time in the literature.

Lastly, within the scope of this study, the production methodology of a synthetic experimental model which has an exact human respiratory system geometry was demonstrated, and the experimental model, except for the fat tissue, was successfully manufactured using an additive manufacturing techniques.

1.5 The Outline of the Thesis

The thesis outline can be defined as follows: Chapter I briefly introduces lung acoustics. Chapter 2 presents theoretical backgrounds of acoustic wave propagation in solid and fluid mediums and the acoustic imaging techniques. Chapter 3 provides the results obtained from simple 2D and 3D models of the human respiratory system. In Chapter 4, acoustic images obtained from the realistic numerical model are presented. In Chapter 5, we provide the details of the production process of the synthetic experimental model. In Chapter 6, we present a conclusion and discussion on the findings and possible future work ideas for the extension of this study.

CHAPTER 2

THEORY

2.1 Acoustic Wave Motion

Aristotle (384–322 BC) defined the sound phenomena as "sound takes place when bodies strike the air, by its being moved in a corresponding manner; the air being contracted and expanded and overtaken, and again struck by the impulses of the breath and the strings, for when air falls upon and strikes the air which is next to it, the air is carried forward with an impetus, and that which is contiguous to the first is carried onward; so that the same voice spreads every way as far as the motion of the air takes place" [31]. Even if he had defined it more than two thousand years ago, he clearly understood and showed that sound is formed and propagated by pressure variation of the surrounding medium, which is a very accurate explanation. But he probably made this definition for the term "sound" at the time, considering the audible frequency range and fluidic medium. In the scope of this thesis, we consider all mechanical vibrations and compression (longitudinal) and shear (transverse) waves at any frequency with the term "acoustic wave" [32] which includes sound waves also.

As a more up-to-date and inclusive definition, an acoustic wave is a mechanical oscillation of pressure that travels through a medium like solid, liquid, gas, or plasma. This wave transmits the energy from one point in the medium to another [33]. Depending on the type of medium, acoustic wave itself induces compression waves and shear waves (thermal waves are neglected in the scope of this study). A compression wave is an oscillation of the particle that moves through a medium perpendicular to the direction of the wave motion. This type of waves can be found in fluids that are compressible. Sound, infrasonic and ultrasonic waves are examples of compression wave. Shear waves, which are commonly occur in elastic solid medium, also arise as a result of the oscillation of the particles, but unlike compression waves, the oscillating motion of the particle is perpendicular to the direction of the wave motion.

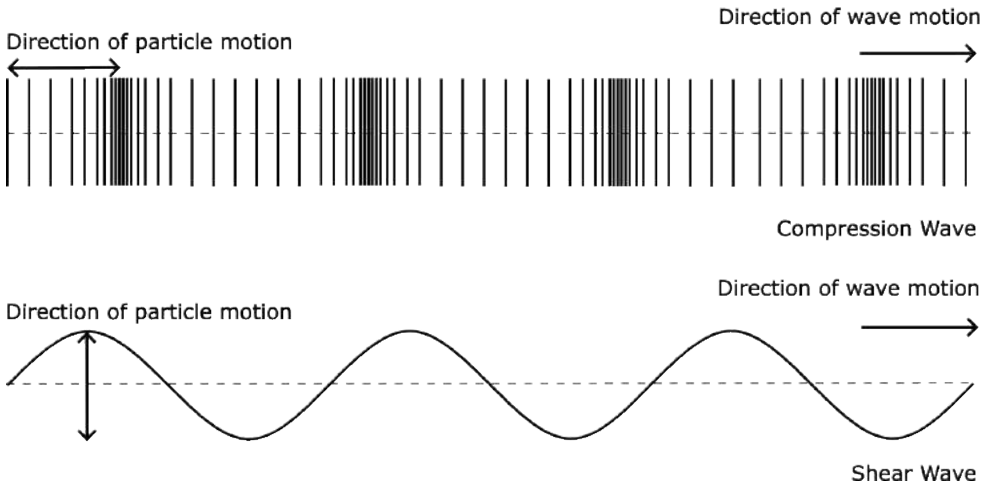

Figure 2.1: Representation of compression and shear waves

2.1.1 Wave Equation in Fluidic Media

The acoustic wave equation for the compressible and inviscid fluidic media is governed by three physical parameters: acoustic pressure, fluid-particle velocity, and medium density. These parameters are not independent of each other. Equations that show their relations can be derived by using three main laws (conservation of momentum, conservation of mass and ideal gas). To better understand the physics of the acoustic wave equation and the relations between these physical parameters, the simplest representation might be the one-dimensional harmonic excitation with a radian frequency (ω) of a pipe with a finite length which is shown in Figure 2.2.

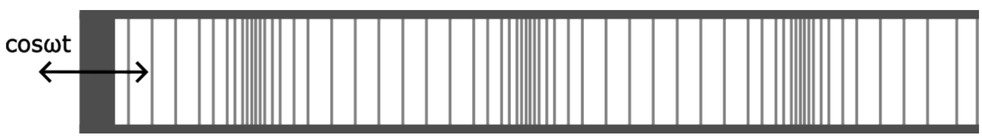

Figure 2.2: One-dimensional harmonic excitation of a pipe

Newton's law of conservation of momentum states that if a force is applied to a small volume of gas, it will accelerate [34]. The harmonic excitation at the inlet of the pipe creates pressure variations on opposite sides of the small volume which provide the forcing. Figure 2.3 illustrates the momentum balance for the infinitesimal element in a pipe where S is the cross-sectional area of the pipe, p is the pressure, ρ is the density of the fluid and u is fluid-particle velocity in x direction.

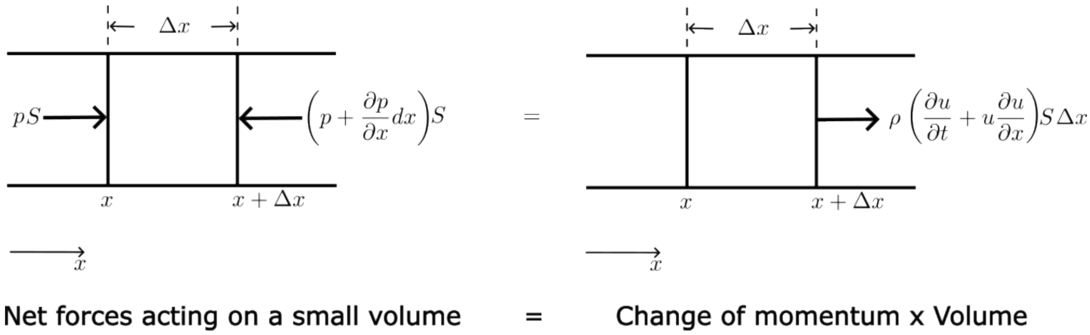

Figure 2.3: Conservation of momentum for infinitesimal volume of fluid

Conservation of momentum can be formulated by assuming Δx is small enough to neglect the change in the cross-section area as follows:

$$-\frac{\partial p}{\partial x} = \rho\left(\frac{\partial u}{\partial t} + u\frac{\partial u}{\partial x}\right) \tag{2.1}$$

where

$$p = p_0 + p' \tag{2.2}$$

$$\rho = \rho_0 + \rho' \tag{2.3}$$

$$u = u_0 + u' \tag{2.4}$$

Equation 2.2 and Equation 2.3 state that total pressure and density of the fluid are composed of the equilibrium or ambient pressure (p_0), the acoustic pressure (p'), the equilibrium density (ρ_0), and fluctuating density (ρ'). The acoustic pressure and the fluctuating density are very small compared to equilibrium pressure and density. For

Equation 2.4, equilibrium velocity can be neglected since the medium is assumed as stationary fluid (i.e. $u_0 = 0$), so total velocity (u) is equal to particle velocity (u'). Assuming equilibrium pressure and density do not vary with time and space, Equation 2.1 can be modified as follows:

$$-\frac{\partial p'}{\partial x} = \rho_0 \frac{\partial u}{\partial t} \tag{2.5}$$

Equation 2.5, which is called the linearized Euler equation, implies that pressure changes over infinitesimal distance (Δx) cause acceleration of a mass/unit volume of fluid (i.e. ρ_0) by the magnitude of $\partial u/\partial t$. This equation shows the relationship between acoustic pressure and fluid-particle velocity. Two more equations are needed to understand the acoustic motion, derive the acoustic wave equation, and obtain the exact relationship between these parameters.

The second equation can be derived using the conservation of mass, which is shown in Figure 2.4. Conservation of mass states that the change of unit mass within the infinitesimal volume with respect to time must be equal to the net mass flow through the infinitesimal volume. The law of conservation mass shows the relationship between fluid-particle velocity and fluid density [34].

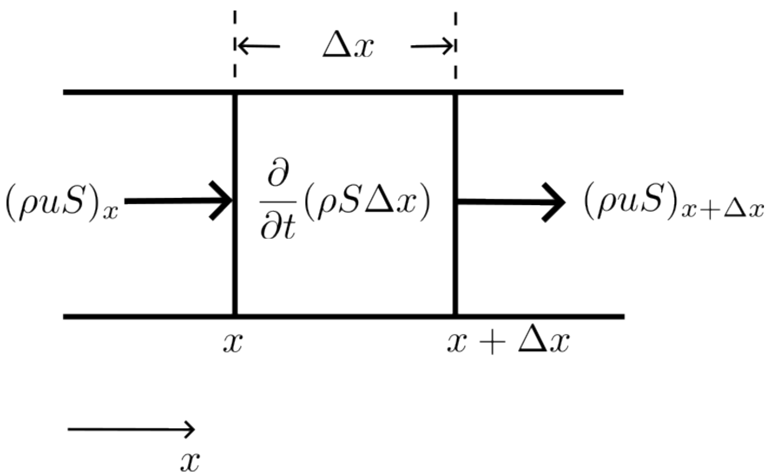

Figure 2.4: Conservation of mass for infinitesimal volume of fluid

Figure 2.4 can be represented mathematically by assuming the cross-sectional area of pipe (S) is constant with respect to time and space, as follows:

$$\frac{\partial \rho}{\partial t} = -\frac{\partial}{\partial x}(\rho u) \tag{2.6}$$

It is assumed that equilibrium pressure does not vary with time and space, so Equation 2.6 can be rewritten by using Equation 2.2 as:

$$\frac{\partial \rho'}{\partial t} = -\rho_0 \frac{\partial u}{\partial x} \tag{2.7}$$

Equation 2.7, which is called the continuity equation, shows the relationship between fluctuating density and fluid-particle velocity. So far, two main equations (Equation 2.5 and Equation 2.7) are obtained which describe relations between acoustic pressure and fluid-particle velocity, and fluid-particle velocity and fluctuating density respectively. However, one more equation is needed to reveal the relationship between acoustic pressure and fluctuating density and provide a unique solution.

The third equation can be derived by using ideal gas law and thermodynamic relations. The change in the internal energy per unit mass is shown in Equation 2.8 where e is the specific internal energy, α is equal to $(1/\rho)$, T is the temperature, and s is the specific entropy.

$$\mathrm{d}e = -p\,\mathrm{d}\alpha + T\,\mathrm{d}s \tag{2.8}$$

Equation 2.8 states that pressure is a function of fluid density and the specific entropy, so the relationship between them can be written as:

$$p = p(\rho, s) \tag{2.9}$$

Pressure fluctuation can be obtained by taking the derivative of the Equation 2.9 with respect to fluid density and specific entropy as follows:

$$dp = \left.\frac{\partial p}{\partial \rho}\right|_s d\rho + \left.\frac{\partial p}{\partial s}\right|_\rho ds. \tag{2.10}$$

It can be assumed that compression and rarefaction motion of the fluid is an isentropic and reversible process (i.e. $\mathrm{d}s = 0$) for the audible frequency range (20 Hz-20 KHz) [34]. Therefore, Equation 2.9 can be modified by using Equation 2.2 and Equation 2.3 as:

$$\frac{p'}{\rho'} = \frac{B}{\rho_0} = c^2 \tag{2.11}$$

where B is the bulk modulus, and c is the speed of sound. The bulk modulus is an elastic property that describes the reduction in the volume of a material subjected to pressure. Equation 2.11 is called the equation of state. The relation between the first and second terms of Equation 2.11 results from empirical studies. This equation implies that there is proportionality between acoustic pressure and fluctuating density.

So far, we have obtained the three equations (Equation 2.5, 2.7, and 2.11) needed. By manipulating these three equations analytically, one-dimensional linear acoustic wave equation for inviscid and compressible fluid can be derived as:

$$\frac{\partial^2 p'}{\partial x^2} = \frac{1}{c^2}\frac{\partial^2 p'}{\partial t^2} \tag{2.12}$$

It is also possible to extend Equation 2.12 for the three-dimensional case with rectangular coordinates (same methodology can be applied for the cylindrical and spherical coordinates). We can write the pressure gradient with respect to the (x, y, z) as follows:

$$\begin{aligned} -\frac{\partial p'}{\partial x} &= \rho_0 \frac{\partial u}{\partial t} \\ -\frac{\partial p'}{\partial y} &= \rho_0 \frac{\partial v}{\partial t} \\ -\frac{\partial p'}{\partial z} &= \rho_0 \frac{\partial w}{\partial t} \end{aligned} \tag{2.13}$$

If we use Laplace Operator, above pressure gradient equations can be expressed as a single equation as:

$$-\nabla p' = \rho_0 \frac{\partial \vec{u}}{\partial t} \tag{2.14}$$

where

$$\vec{u} = (u, v, w) \tag{2.15}$$

Equation 2.7 can be also written using same methodology for the three-dimensional case as follows:

$$\frac{\partial \rho'}{\partial t} = -\rho_0 \nabla \cdot \vec{u} \tag{2.16}$$

By manipulating Equation 2.11, Equation 2.14 and Equation 2.16 analytically, three-dimensional linear acoustic wave equation for inviscid and compressible fluid can be derived as:

$$\nabla^2 p' = \frac{1}{c^2} \frac{\partial^2 p'}{\partial t^2} \tag{2.17}$$

2.1.2 Acoustic-Structure Interaction

When acoustic waves encounter a solid structure, it creates an external pressure on the surface of the solid medium. This pressure creates internal stresses within the medium, causing small displacements. For solid mediums, these displacements can be used to derive the equation of motion under the harmonic loading. Governing equation for this type of interaction is the conservation of momentum [35] which can be written for the three-dimensional case as follows:

$$\rho_{solid} \frac{\partial^2 \mathbf{u_{solid}}}{\partial t^2} = \mathbf{f_v} + \nabla \boldsymbol{\sigma} \tag{2.18}$$

where ρ_{solid} is the density of the deformed medium, $\mathbf{u_{solid}}$ is the displacement vector, $\mathbf{f_v}$ is the force per deformed volume, and σ is the Cauchy stress tensor. This symmetrically structured tensor, which is called also "True Stress" represents the stress which is defined as the current force per deformed surface area of a infinitesimal element.

The Cauchy stress tensor assumes a geometric linearity of the volume by considering small displacements. The problem with the mentioned stress model stems from this assumption. The local density of each infinitesimal deformed element will be different under the loading due to geometric non-linearity. This problem can be solved by using other stress tensor models derived from the Cauchy stress tensor. The first stress tensor model can be expressed as [35]:

$$\boldsymbol{P} = \mathbf{J}\boldsymbol{\sigma}\mathbf{F}^{-T} \tag{2.19}$$

where $\boldsymbol{P}$ is the first Piola-Kirchhoff stress tensor (also called "Engineering Stress"), $\mathbf{F}$ is the deformation gradient tensor, $\mathbf{J}$ is Jacobian of the deformation gradient tensor, and T is the transpose operator. The $\boldsymbol{P}$ is non-symmetric two-point tensor that relates the current force acting on the deformed area per undeformed area [36]. To obtain the equation of motion for this tensor, we should substitute Equation 2.19 into Equation 2.18 which gives

$$\rho_{solid,0}\frac{\partial^2 \mathbf{u}}{\partial t^2} = \mathbf{F}_{\mathrm{V}} + \nabla \boldsymbol{P} \tag{2.20}$$

where $\mathbf{F}_{\mathrm{V}}$ is a body force in the deformed configuration, and $\rho_{solid,0}$ is the density in the undeformed configuration.

Another stress tensor model can be written as following [35]:

$$\boldsymbol{S} = \mathbf{J}\mathbf{F}^{-1}\boldsymbol{\sigma}\mathbf{F}^{-\mathrm{T}} \tag{2.21}$$

where $\boldsymbol{S}$ is the second Piola-Kirchhoff stress tensor. Substituting Equation 2.21 into the Equation 2.18 gives

$$\rho_{solid,0}\frac{\partial^2 \mathbf{u}}{\partial t^2} = \mathbf{F}_{\mathrm{V}} + \nabla \mathbf{F}\boldsymbol{S}. \tag{2.22}$$

Equation 2.22 shows the equation of motion with the second Piola-Kirchoff stress tensor. The $\boldsymbol{S}$ is symmetric tensor that relates the resulting transformed forces in the deformed configuration with the area of undeformed configuration [36].

More stress tensors are available in the literature, which are used for different continuum mechanics problems. However, these tensors are not in the scope of this thesis. Above mentioned stress tensors (Cauchy, the first Piola-Kirchoff, and the second Piola-Kirchoff) and equation of motions are used in this study.

2.2 Acoustic Imaging and Localization Methods

Acoustic imaging and sound source localization methods have been widely used in different applications such as radar/sonar, communication, underwater surveillance, and biomedical technologies. Although its purpose of use varies depending on the problem, the general purpose of these methods is to determine the strength and/or location of sound sources or location of objects that act as sound sources (such as objects with highly reflective surfaces). These methods are based on some signal processing techniques. To explain in more detail, information about the acoustic field and location/strength of sound sources can be obtained by processing sound signals which are generally obtained by using a phased array of microphones or hydrophones through the spatial and/or temporal filtering techniques. A lot of research has been done in the past decade, especially for underwater and communication applications. As a result of these studies, many advanced techniques have been developed over the years, especially after the advances in computation technologies and data acquisition systems, however the performance of each technique depends on the problem or application itself. In other words, the complexity, geometry, homogeneity, or other state properties of each medium can have a major impact on the performance of the chosen method.

Two fundamental methods are available for acoustic imaging and sound source localization that appear in the literature [37]: Conventional Beamformer (i.e. Matched-Beam Processor) and Matched-Field Processor. Existing advanced methods generally are developed and modified versions of these two fundamental methods for different problems and applications. In depth examination of the literature showed that there has not been much practice and research on the acoustic imaging of the human respiratory system; therefore only these two main techniques have been included in the scope of this thesis.

2.2.1 Conventional Beamformer

Conventional Beamformer, also called as Delay-And-Sum Beamformer, is the most commonly known and used method to obtain acoustic intensity image of the field by processing acoustic signals which are generally recorded by an array of microphones [38]. Assume that we have a single sound source and N number of microphones within the region of interest which is shown in the Figure 2.5.

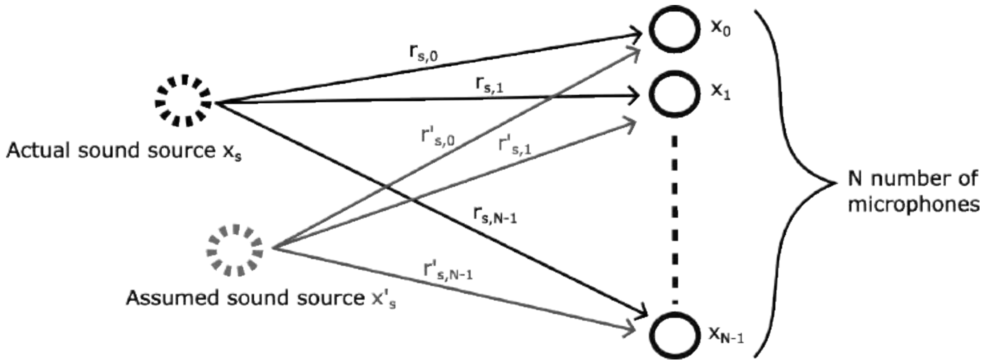

Figure 2.5: Positions of actual and assumed sound sources and array of microphones

For the given configuration, $\mathbf{x_s}$, $\mathbf{x'_s}$ and $\mathbf{x_i}$ where $\mathbf{i = 0, ..., N - 1}$ represent the locations of actual sound source, assumed sound source and each microphone respectively. $\mathbf{r_{s,i}}$, and $\mathbf{r'_{s,i}}$ are absolute distances between actual or assumed sources and each microphone. Since the method is based on the relative relationship between obtained signals and positions of microphones, a reference point must be chosen within the field (by the relative relationship, we mean the coherence of the signals obtained by each microphone with respect to the reference microphone and the coherence between actual and assumed source microphones with respect to each microphone location). This reference point can be chosen arbitrarily [39]. $\mathbf{x_0}$ is chosen as a reference microphone for this configuration.

The obtained signal at each microphone in terms of pressure can be described in time domain as follows:

$$\mathbf{p_i}(t) = a(\mathbf{x}_0, \mathbf{x}_i, \mathbf{x}_s)q(t) \tag{2.23}$$

where $\mathbf{p_i}(t)$ is the pressure signal at the i-th microphone, $\mathbf{a}(x_0, x_i, x_s)$ is the transfer vector that consists of all the information about time delays and attenuation of signals between each microphone, and $q(t)$ is the strength of actual or assumed sound sources. Transfer vector can be written by assuming that there is no-flow within the field and monopole sound source under free-field conditions as [39]:

$$a\left(\mathbf{x}_0, \mathbf{x}_i, \mathbf{x}_s\right) = \frac{r_{s,0}}{r_{s,i}} e^{-jk(r_{s,i}-r_{s,0})} \tag{2.24}$$

where k is the wave number. Equation 2.24 shows that the transfer vector is a function of the distances between sources and microphones, medium properties, and signal characteristics. ($k = \omega/c$ where ω is the frequency of the signal and c is the speed of sound of the medium). For simplicity, we assume that our medium is homogenous (i.e. speed of sound is a constant) and our signal consists of a single frequency. With this assumption, Equation 2.23 can be written in the frequency domain as:

$$p_F(\mathbf{x}'_s) = \mathbf{h}^H(\mathbf{x}'_s)\mathbf{p} \tag{2.25}$$

where $\mathbf{h}$ is called as the steering vector which is a function of the distance between each microphone and assumed sound source, and H is the Hermitian operator. Ideally steering vector should be inverse of the transfer vector. Output of the Equation 2.25 is the weighted sum of the signals where weights obtained from steering vector [40]. According to Sarradj [39], there are at least four different steering vector formulations in the literature which are used for different near-field acoustic beamforming applications which are discussed in the following sections.

Equation 2.25 can be rewritten using auto-power spectrum filter (E) which repesents the power distribution over the frequency by neglecting the phase delays as follows:

$$\begin{aligned} B\left(\mathbf{x}_s'\right) &= E\left\{p_F\left(\mathbf{x}_s'\right) p_F^*\left(\mathbf{x}_s'\right)\right\} = \mathbf{h}^H\left(\mathbf{x}_s'\right) E\left\{\mathbf{p}\mathbf{p}^H\right\} \mathbf{h}\left(\mathbf{x}_s'\right) \\ &= \mathbf{h}^H\left(\mathbf{x}_s'\right) \mathbf{C}_{mn} \mathbf{h}\left(\mathbf{x}_s'\right) \end{aligned} \tag{2.26}$$

where $\mathbf{C}_{mn}$ is called as the Cross-Spectral Matrix (CSM), $B(\mathbf{x}_s)$ is the Conventional Beamformer output, and m and n are microphone numbers. CSM is used to describe the relationship between microphones by comparing the power spectra of the obtained signals in pairs. For the ideal and accurate application of the acoustic source localization, two important conditions must be satisfied by the Conventional Beamformer output which are listed below:

Beamformer's output must provide maximum outcome when the locations of the actual and assumed sound sources are same

$$B\left(\mathbf{x}_s = \mathbf{x}_s'\right) > B\left(\mathbf{x}_s \neq \mathbf{x}_s'\right) \tag{2.27}$$

Beamformer's output must provide correct source strength when the first condition is satisfied

$$B\left(\mathbf{x}_s = \mathbf{x}_s'\right) = E\left\{qq^*\right\}. \tag{2.28}$$

It can be said that meeting given conditions successfully depends on the selected steering vector that includes the sound propagation model. The four steering vector formulations, which were presented previously by Sarradj [39], are shown in the following section.

2.2.1.1 Formulation I

The first formulation is based on the comparison of the signal amplitudes by neglecting phase relation. Sound localization is achieved by the compensation of the phase delays between the N number of microphones and the source through the steering vector. This steering vector, which is the most basic method that is available in the literature, is mostly used for far-field applications where the plane wave propagation model is applicable that satisfies the first condition (Equation 2.27) rather than the second condition (Equation 2.28) [41].

$$h_i^{\mathrm{I}} = \frac{1}{N} e^{-jk(r_{s,i} - r_{s,0})}. \tag{2.29}$$

2.2.1.2 Formulation II

Another commonly used steering vector formulation [42, 43] can be written as follows:

$$h_i^{\mathrm{II}} = \frac{1}{N} \frac{r_{s,i}}{r_{s,0}} e^{-jk(r_{s,i} - r_{s,0})}. \tag{2.30}$$

Besides the phase delays between microphones and source, the second formulation also performs the compensation of the signal amplitudes. This formulation satisfies the latter condition more successfully by considering the obtaining the actual source strength rather than the actual location of the source [39].

2.2.1.3 Formulation III

The third formulation, shown in the Equation 2.31, is mainly used for aeroacoustic applications as it provides better performance at the satisfaction of the latter condition (Equation 2.28) like the second formulation [40]. The idea of this formulation can be described as passing the signals through the filter without being undistorted while all signals are exposed to the same amount of attenuation [39]. In other words, this method relies on the minimization of the attenuated responses passed the filter by using white noise [44].

$$h_i^{\mathrm{III}} = \frac{1}{r_{s,0} r_{s,i} \sum_{j=1}^{N} \left(1/r_{s,j}^2\right)} e^{-jk(r_{s,i} - r_{s,0})} \tag{2.31}$$

2.2.1.4 Formulation IV

The last formulation uses the least-square technique to minimize the error between microphones and source that is similar to the previous formulation by assuming that the weight vector is parallel to the propagation vector when $x_s = x_s'$ to maximize the output of the steering vector [45, 46].

$$h_i^{\mathrm{IV}} = \frac{1}{r_{s,i}\sqrt{N\sum_{j=1}^{N}\left(1/r_{s,j}^2\right)}} e^{-jk(r_{s,i}-r_{s,0})} \tag{2.32}$$

2.2.1.5 Comparison of the Formulations

So far, we have described four steering vector formulations used for different sound source localization and acoustic mapping applications. All of these formulations have certain advantages and disadvantages. Therefore, choosing the proper formulation based on the application is very important. According to the comparative studies [39, 47], the first and fourth formulations are more suitable methods for accurately estimating the position of the sound source, while the second and third formulations are more ideal for obtaining the correct source power. In Chapter 3, the performances of these four different steering vector formulations are compared for the 2D numerical model of human respiratory system.

2.2.2 Matched Field Processor

Matched Field Processor (MFP) is a technique that has gained interest, especially in underwater acoustics during the 1990s, and is still used today in different applications such as underwater surveillance [48]. The reason for this interest is that the method provides more robust and accurate results than the Conventional Beamformer since it also can be applied to nonhomogenous mediums by considering the environmental effects. The elementary idea behind the technique is the comparison of the two different data sets: data sets of measured and replica signals.

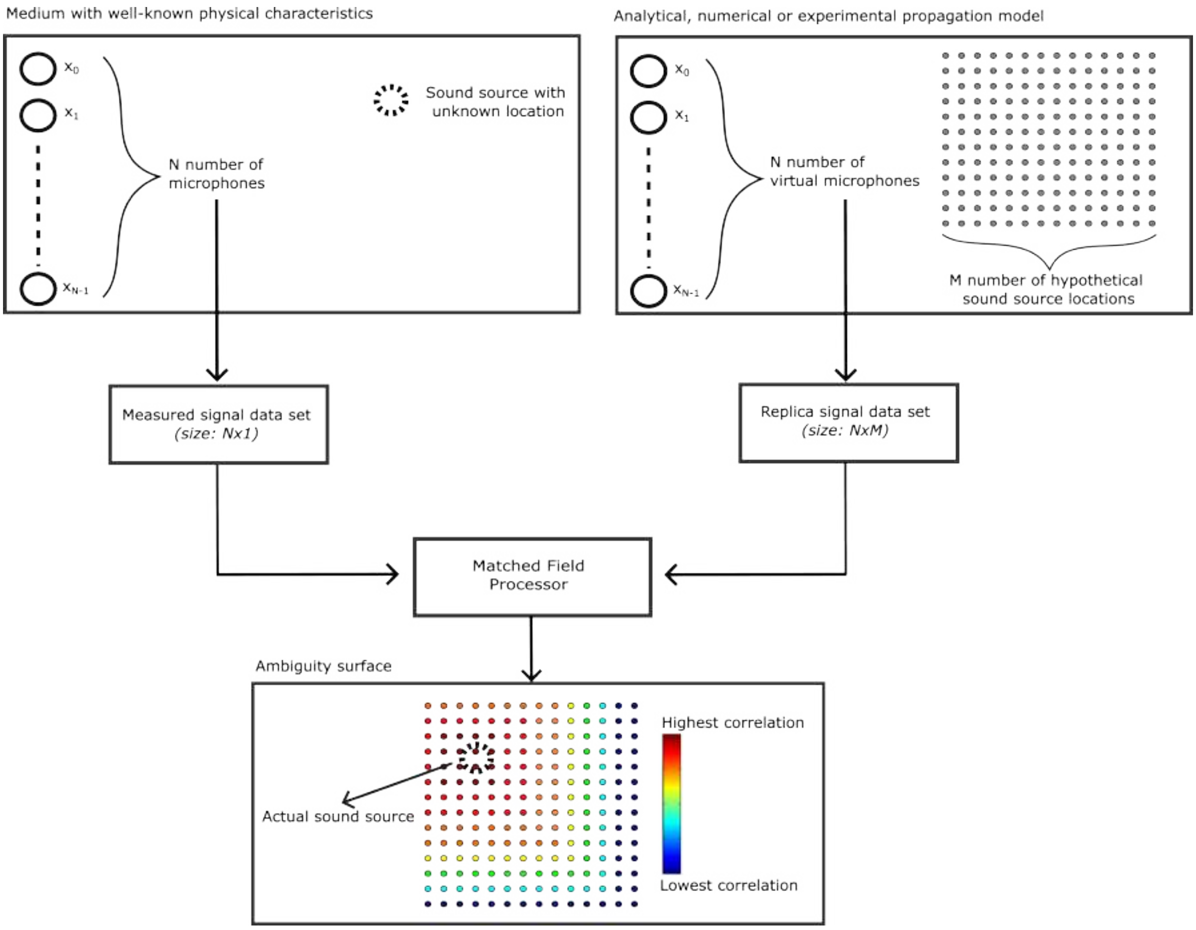

Figure 2.6: The basic operating principle of Matched Field Processing

To give a better explanation how this comparison between data sets is made for the sound source localization, we can go through the example case illustrated in Figure 2.6. Let us consider a sound source whose location is unknown in a medium whose specific characteristics such as speed of sound, attenuation, and density, are known. The response of the sound source can be measured using array of sensors (e.g. microphones), and compared with the replica data that can be obtained by using analytical, numerical or experimental models. Suppose that we can accurately construct the domain, model the sound propagation and collect the response for each possible location of the sound source. In that case, cross-correlation of data sets will present the similarity of each replica data set to the measured one. MFP states that the replica data set with the highest correlation is the candidate for the location of the sound source [48].

The same procedure can also be applied to the cases where the location of the sound source is known but some properties of the medium, such as attenuation, are unknown [48, 49]. MFP states that the value used for the unknown parameter that results in the maximum output of the processor is the closest value to the interested environmental parameter.

Several processor formulations and benchmark studies for different applications are available in the literature [48, 49, 50]. In the scope of this thesis, two different processors are selected and applied for the acoustic imaging of the human respiratory system: the Linear Processor, also known as the Conventional Processor, and the Bartlett Processor, and the Minimum Variance Distortionless Response (MVDR), also known as the Capon Processor.

The Linear Processor is a simple and robust method, but one main disadvantage of the method is that side lobes can dominate the main lobe so that high correlation at non-source locations might be obtained [48]. As mentioned in Chapter 1, the Linear Processor is the only processor that has been applied for the sound source localization within the human respiratory system [16, 17]. On the other hand, MVDR provides excellent suppression of side lobe responses and main lobe dominance; however, it is not as robust as a Linear Processor. Especially when there is a mismatch in environmental parameters and external noise, MVDR gives less accurate localization results comparing with the Linear Processor [51]. Both processors are defined more detailed in the following subsections as given in [48].

2.2.2.1 The Linear Processor

The main idea behind the Linear Processor is the direct correlation of the measured signals and replica signals. Assuming that we have N number of microphones, $\mathbf{x}_j$ is the position vector of each microphone where $j = 0, 1, ..., N-1$, $\mathbf{x}_s$ is the position vector of the sound source, and ω is the frequency of the sound source. Then, we can define the data set of measured signals, i.e. $\mathbf{F}(\mathbf{x}_s)$, as follows:

$$\mathbf{F}(\mathbf{x}_s) = [F_1(\mathbf{x}_s, \omega), \ldots, F_{N-1}(\mathbf{x}_s, \omega)] \, . \tag{2.33}$$

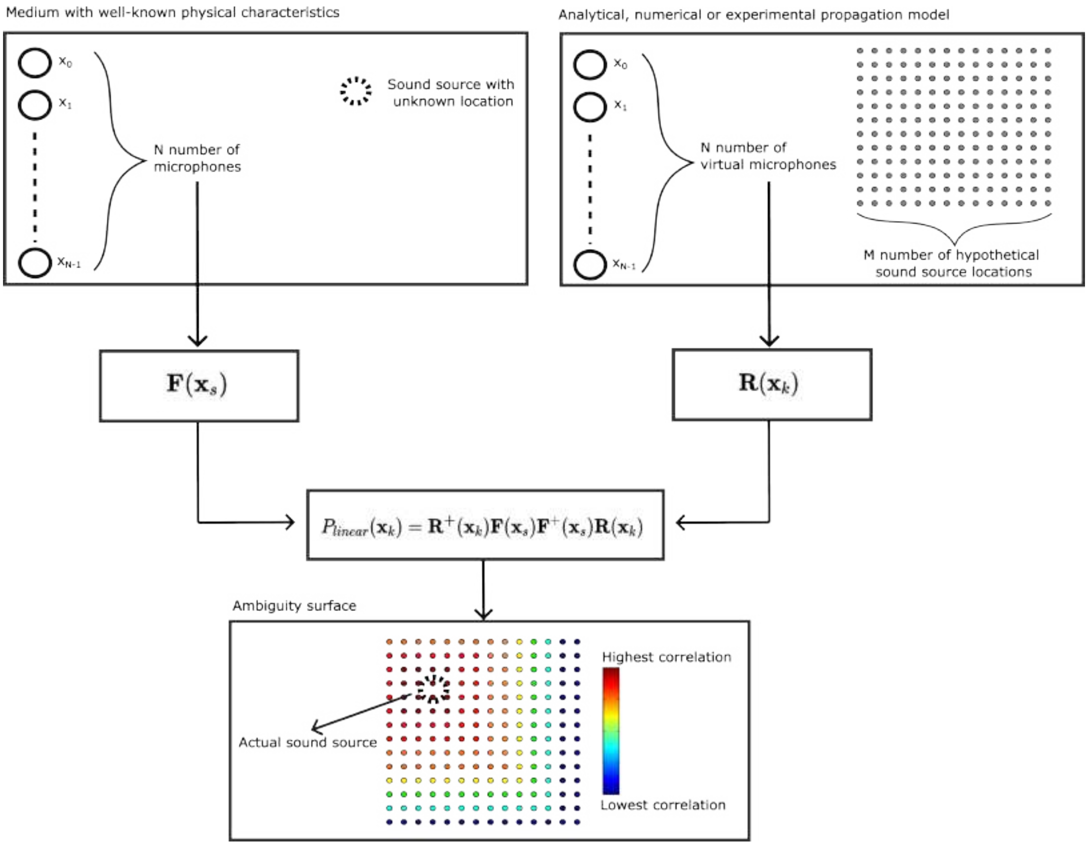

Figure 2.7: The basic operating principle of the Linear Processor

So far, we have defined the measured signal data set for a single sound source and frequency. One more data set is needed for the comparison, which consists of the replica signals. Assuming that we have N number of virtual microphones whose position vectors are the same with the actual microphones (i.e. $\mathbf{x}_i$), M is the number of possible sound source points within the acoustic field, $\mathbf{x}_k$ is the position vector of the each replica sound source where $k = 0, 1, ..., M - 1$. With this assumptions, the data set of the replica signals, $\mathbf{R}(\mathbf{x}_k)$, can be written as follows:

$$\mathbf{R}(\mathbf{x}_k) = [R_0(\mathbf{x}_k, \omega), \ldots, R_{N-1}(\mathbf{x}_k, \omega)] \,. \tag{2.34}$$

Next, we can write the Linear Processor which gives the correlation of the measured signal with each replica signal by assuming that both data sets are normalized to 1 with respect to L2 norm [48] (i.e. $||\mathbf{F}|| = 1$ and $||\mathbf{R}|| = 1$):

$$P_{linear}(\mathbf{x}_k) = \mathbf{R}^{+}(\mathbf{x}_k)\mathbf{F}(\mathbf{x}_s)\mathbf{F}^{+}(\mathbf{x}_s)\mathbf{R}(\mathbf{x}_k) \tag{2.35}$$

where $P_{linear}(\mathbf{x}_k)$ is the Linear Processor which contains the information about the similarity of each data set of replica signal to the measured signal, and $+$ corresponds to complex conjugate. In theory, the highest output of the Linear Processor should present the most likely candidate for the location of the sound source within the acoustic field. The basic operating principle of the Linear Processor is illustrated in Figure 2.7.

2.2.2.2 The Minimum Variance Distortionless Response (MVDR)

In the literature, several studies have been conducted to improve the performance of the Linear Processor resulting in different Matched Field Processing approaches [48], and MVDR is one of the processors that emerged from these studies. The processor was firstly proposed by Capon in 1967 [52]. The essence of the technique is the minimization of the noise to suppress the side lobes without distorting the measured signal by applying digital filter to replica signals. MVDR processor can be defined briefly as follows (for more detailed derivation, see [48]):

$$P_{mvdr}(\mathbf{x}_k) = \frac{\mathbf{1}}{\mathbf{R}'^{+}(\mathbf{x}_k)[\mathbf{F}(\mathbf{x}_s)\mathbf{F}^{+}(\mathbf{x}_s)]^{-1}\mathbf{R}'(\mathbf{x}_k)} \tag{2.36}$$

where

$$\mathbf{R}'(\mathbf{x}_k) = \frac{[\mathbf{F}(\mathbf{x}_s)\mathbf{F}^{+}(\mathbf{x}_s)]^{-1}\mathbf{R}(\mathbf{x}_k)}{\mathbf{R}^{+}(\mathbf{x}_k)[\mathbf{F}(\mathbf{x}_s)\mathbf{F}^{+}(\mathbf{x}_s)]^{-1}\mathbf{R}(\mathbf{x}_k)}. \tag{2.37}$$

In principle, the MVDR processor's highest output should represent the most likely position of the sound source, similar to the Linear Processor. Figure 2.8 depicts the MVDR processor's working principle.

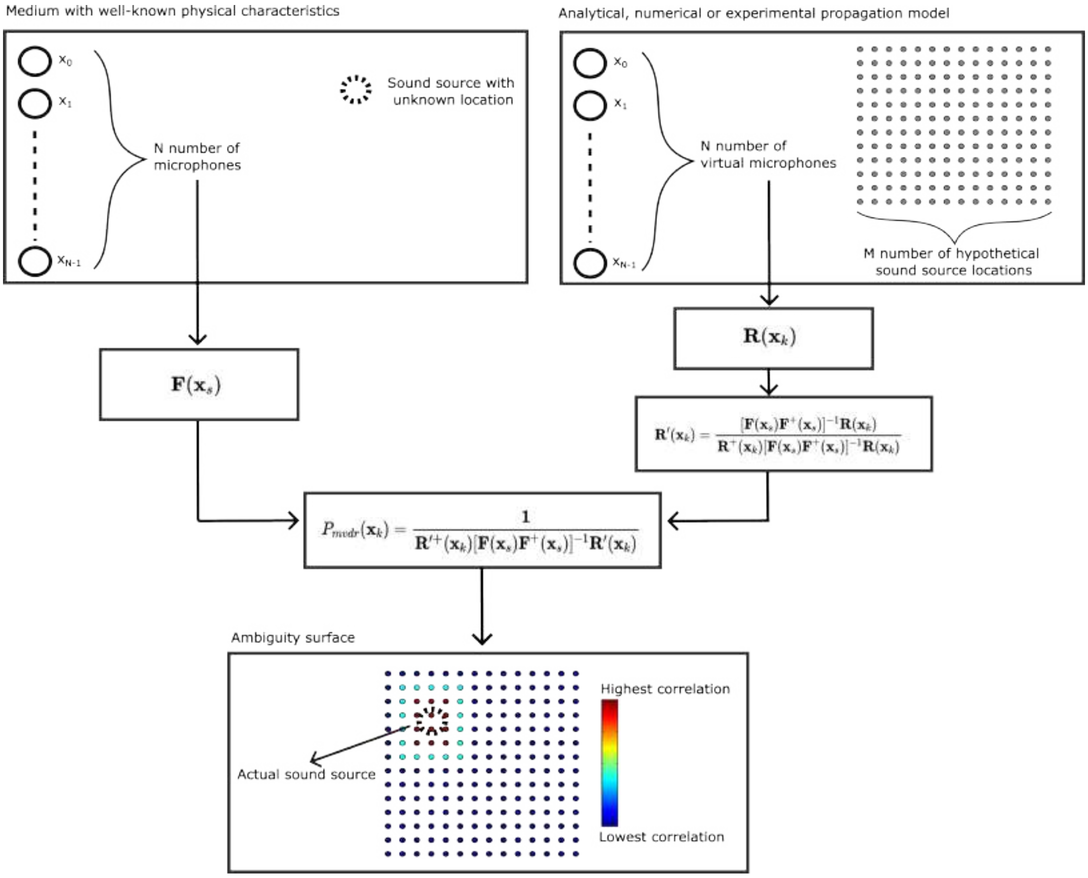

Figure 2.8: The basic operating principle of the MVDR processor

2.2.2.3 Comparison of the Processors

According to Tolstoy [53], although the MVDR gives a more specificied result than the Linear Processor, the mismatches in the environment affect the MVDR results more. Comparative study [53] showed that the performance of the Linear Processor is more robust and consistent as the side lobes are suppressed when using the MVDR. The MVDR, on the other hand, performs much better in obtaining the environment parameters.

CHAPTER 3

NUMERICAL INVESTIGATION OF ACOUSTIC IMAGING AND LOCALIZATION TECHNIQUES

3.1 Acoustic Modeling of Representative Human Respiratory System

Advanced numerical analysis techniques, modeling and simulation software, and image processing algorithms that emerged with the developing technology have enabled us to conduct important scientific studies in many fields. These studies have obtained significant findings over the last couple of decades. These numerical techniques are generally used to solve complex problems when it is not possible to model such problems analytically. On the other hand, experimental analysis techniques are less preferred as they are much more complex, expensive, and have more limitations than numerical analysis techniques. Especially in the medical field, problems such as clinical research permission required for experimental studies and the inability to easily control and manipulate subjects' physiology due to ethical reasons have caused these numerical methods to be preferred and used more frequently. For example, using these methods, we can numerically model a fractured femur bone and design the most suitable implant by comparing the bone plates' different materials and geometric properties to be used in the treatment [54]. As an example of another use case, a complete 3D model of the human eye can be created and used to investigate the causes of eye-related diseases such as Presbyopia [55] and can provide crucial subject-specified information that may be useful for the treatment of the patient.

In this study, the techniques mentioned above were used to understand the sound propagation within the human respiratory system and investigate the potential and limitations of the sound localization techniques for diagnostic purposes. This chapter provides results obtained using the simple 2D and 3D representative human respiratory system models. The following sections present geometry, material selection, and finite element modeling details.

Figure 3.1: Numerical model of broken femur bone and plate [53] (left), opto-mechanical parametric model of the human eye [54] (middle), eye deformation and ray tracing results obtained from simulation [54] (right).

3.1.1 Geometry

In the first attempts, the create numerical models of the human respiratory system, very simple geometries were preferred. The purpose of using these models is that they can be easily modeled and verified by analytical and experimental methods due to their simplicity. These models also provide computational efficiency, allowing us to perform more repeatable simulations. Two examples of simple modeling approaches are given in Figure 3.2, which were used previously by Wodicka [15], and Royston [9] in their studies.

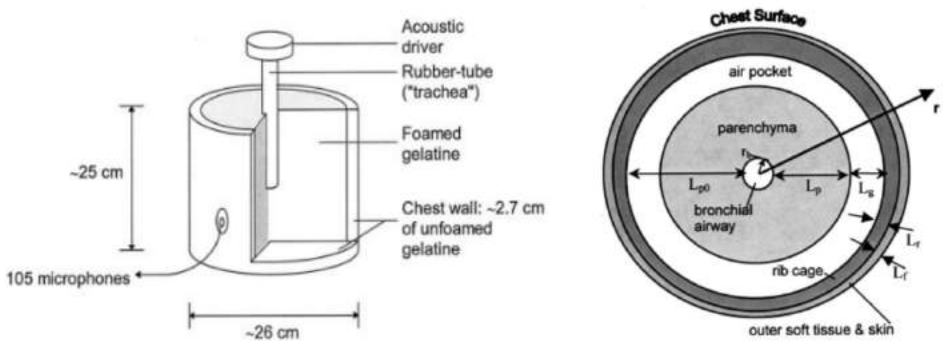

Figure 3.2: Schematic drawings of the 3D human respiratory system [15] (left), and the 2D human respiratory system with pneumothorax [9] (right).

Our first aim in this study is to verify the applicability of the sound localization techniques, so preliminary studies were conducted using simple 2D and 3D models. Schematic drawings of the 2D and 3D human respiratory systems used in simulations are given in Figure 3.3 and Figure 3.4, respectively.

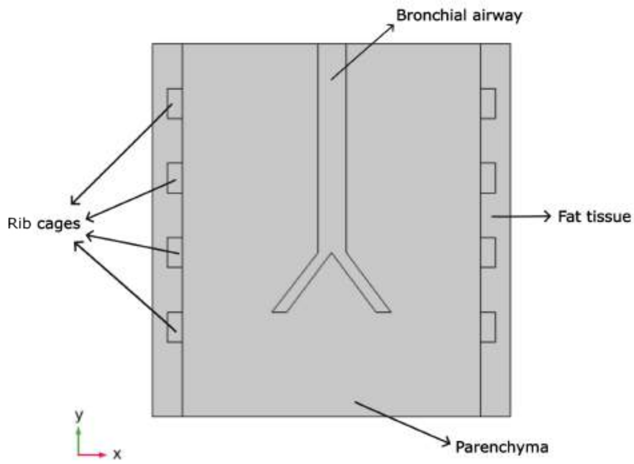

Figure 3.3: Simple 2D numerical model of the human respiratory system on a XY plane.

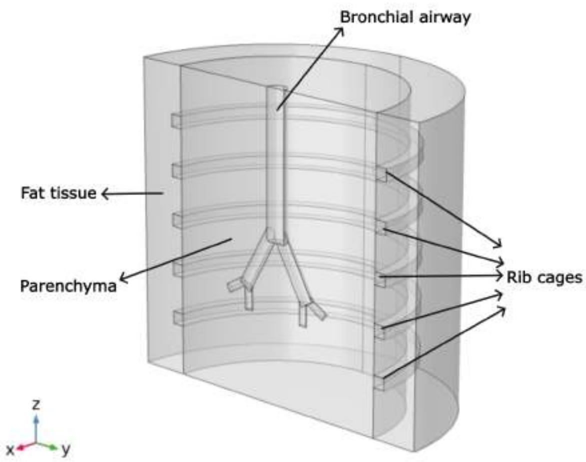

Figure 3.4: Simple 3D numerical model of the human respiratory system on a YZ cut-plane.

The dimensions of the parenchyma, rib cage, and fat tissue structures used in the simple model were determined according to Vovk's study [56], which are shown in Figure 3.5. For the dimensions of the bronchial airway, Weibel's study [57] has been followed. Considering the frequency range of interest and corresponding wavelength in this study, the thickness of the bronchial airway was neglected. For the sound propagation within the airway, only the first three branches were modeled and used since compression waves are much more dominant in this region, and the acoustic pressure is very low at the remaining branches [58]. Dimensions of the bronchial airway are given in Figure 3.6.

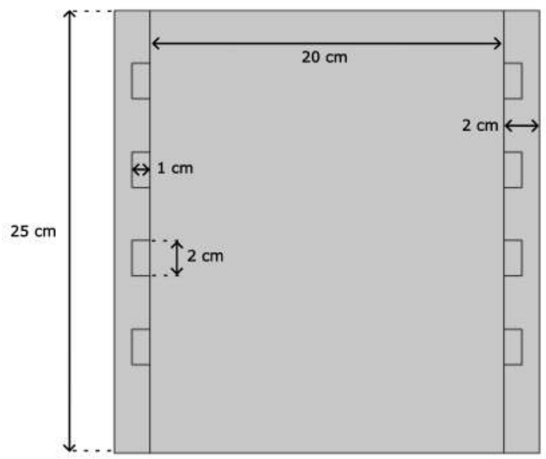

Figure 3.5: Dimensions of the parenchyma, rib cage and fat tissue.

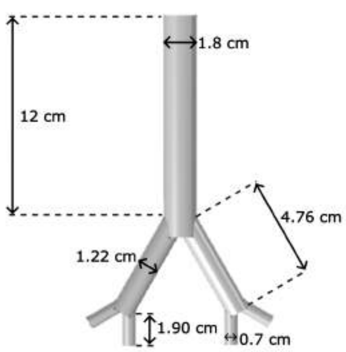

Figure 3.6: Dimensions of the bronchial airway.

3.1.2 Material Selection

In this study, our primary aim is to investigate the applicability of sound source localization techniques and the usability of the synthetic human respiratory system for experimental analyses. For this reason, the material selection is made according to the accessibility of the materials and the producibility of the experimental model. Of course, the human tissues' mechanical and acoustical properties have been taken into account during the material selection, but using exactly the right properties has not been our priority. The acoustical and mechanical properties of the selected materials to imitate the bronchial airway, parenchyma, fat tissue, and rib cage are given in Table 3.1.

In the literature, It has been hypothesized that parenchymal tissue can be described as a homogeneous isotropic material sustaining solely acoustic compression waves (i.e., lossy fluid) for frequencies over 100 Hz [59, 60]. Ozer showed that polyurethane foam has similar mechanical properties to parenchyma tissue in terms of speed of sound, density, and sound attenuation [16]. Therefore, polyurethane is selected as the lung material in this study. As previously mentioned, the thickness of the bronchial airway is neglected in this study, considering the frequency range. As a result of this assumption, the air is assigned as a material of the human airway.

It is known that compression waves dominate the parenchyma and bronchial airway [16], but this phenomenon is not valid for the remaining non-parenchymal regions. Besides the compression waves, shear waves in the fat tissue of muscle, the vascular system, and fat and the rib cage should also be considered. Considering the mechanical behavior of these tissues, PDMS and PMMA are chosen as materials to mimic the acoustic wave propagation through the fat tissue and rib cage on the basis of previous studies [61, 62], respectively.

Up to this point, we have assigned materials to mentioned tissues considering the healthy respiratory system. However, in the scope of this thesis, we aim to detect the abnormalities within the lung and obtain region-specific information so that we also need to model these unhealthy regions. An in-depth examination of the literature on pulmonary system diseases reveals that some diseases are caused by the partial or complete filling of the lungs with fluids. For example, pneumothorax is the shrinkage of a part or all of the lung, described as "collapse", and the filling of the precipitated area with air. As another example, pleurisy, which is seen in the form of water accumulation in the lungs, is one of the acute lung diseases. Water is selected as the material to model these abnormalities in this study.

Table 3.1: Acoustical and mechanical properties of the tissues

Bronchial airway		
Speed of sound	c_{air}	$343[m/s]$
Density	ρ_{air}	$1.2[kg/m^3]$
Parenchyma		
Speed of sound	c_{lung}	$30[m/s]$
Density	ρ_{lung}	$160[kg/m^3]$
Attenuation	α_{lung}	$150[dB/m]$
Fat tissue		
Speed of sound	c_{fat}	$1450[m/s]$
Density	ρ_{fat}	$970[kg/m^3]$
Young's Modulus	E_{fat}	$0.75[MPa]$
Poisson's ratio	ν_{fat}	0.49
Rib cage		
Density	ρ_{rib}	$1190[kg/m^3]$
Young's Modulus	E_{rib}	$2855[MPa]$
Poisson's ratio	ν_{rib}	0.35
Abnormal region		
Speed of sound	c_{water}	$1480[m/s]$
Density	ρ_{water}	$997[kg/m^3]$

3.1.3 Finite Element Modeling

Finite element analysis of the human respiratory system was conducted by using COMSOL Multiphysics [63]. Pressure Acoustics, Transient, and Pressure Acoustics, Frequency Domain modules were used to simulate the acoustic wave propagation through the bronchial airway, parenchyma, and abnormal region for both time and frequency domains, respectively. Solid Mechanics module was used to simulate rib cage and fat tissue. The Acoustic-Structure Interaction module was applied to couple the Pressure Acoustics and Solid Mechanics physics. Parenchyma, bronchial airway, and abnormality were modeled using the linear elastic fluid model, and the linear elastic isotropic solid model was used to model the remaining tissues.

Table 3.2: Selected physic modules for finite element analysis

Region	**Physic Module**	**Fluid/Solid Model**
Bronchial airway	Pressure Acoustics, Transient/Frequency	Linear elastic fluid
Parenchyma	Pressure Acoustics, Transient/Frequency	Linear elastic fluid
Abnormal region	Pressure Acoustics, Transient/Frequency	Linear elastic fluid
Rib cage	Solid Mechanics	Isotropic solid
Fat tissue	Solid Mechanics	Isotropic solid

3.1.3.1 Boundary Conditions

Boundary conditions must be defined in order to solve the governing differential equations of the numerical models used in the study. The impedance boundary condition was defined for the regions where the Pressure Acoustic module has been employed. It was assumed that the surrounding medium is air for the impedance boundary condition. A free-free boundary condition was defined for outside the fat tissue where the Solid Mechanical module is used [3]. For the acoustic excitation of the numerical model, a harmonic pressure wave with the magnitude of 1 Pascal was introduced to the airway inlet.

3.1.3.2 Mesh Generation

In order to obtain the correct and accurate solutions to numerical problems, it is necessary to use a sufficient number of mesh elements. In the literature, It is stated that the greatest element size should be at least six times smaller than the acoustic wavelength of the medium to obtain acceptable results for the pressure acoustic problems [64]. The mesh was generated according to this criterion in the regions where the Pressure Acoustic module is used. There was no such criterion in the regions where the Solid Mechanics module was used; the proper mesh size that it converges to the solution has been obtained by trial and error. Considering the highest frequency used in the study (i.e. 600 Hz), finite element mesh consists of 3770 domain elements and 379 boundary elements for the 2D configuration, 354140 domain elements, 21572 boundary elements, and 2698 edge elements for the 3D configuration, respectively.

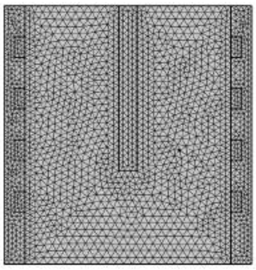

Figure 3.7: Generated mesh for 2D configuration (600 Hz).

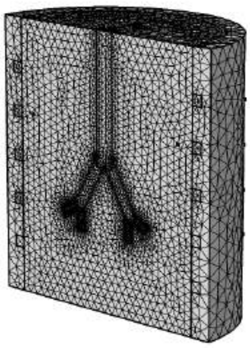

Figure 3.8: Generated mesh for 3D configuration (600 Hz).

3.2 Application of Acoustic Imaging and Localization Techniques

Two main methods were employed in this study for the acoustic imaging of the chest: Conventional Beamformer and Matched-Field Processor. For the application of the Conventional Beamformer, the open source project [65] developed by the research group called Aircraft Noise, and Climate Effects within TU Delft is used [40, 66].

Matched-Field Processor is implemented using software developed by us. Both techniques are employed via MATLAB [67]. 16 and 32 number of measurement points or microphones were used to obtain the normal velocity data with respect to the surface of the fat tissue for 2D, and 3D configurations, which are represented as blue dots shown in Figure 3.9 and Figure 3.10, respectively.

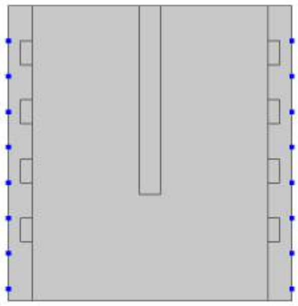

Figure 3.9: Location of microphones represented by blue dots for 2D configuration.

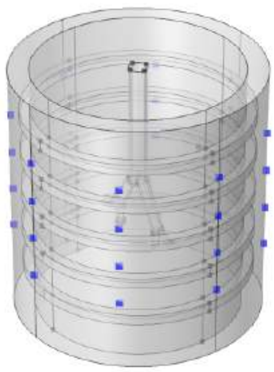

Figure 3.10: Location of microphones represented by blue dots for 3D configuration.

3.3 Simulation and Acoustic Imaging Results for the 2D Configuration

In this section, results of transient and frequency domain simulations and acoustic imaging methods for 2D configuration of the human respiratory system are presented.

3.3.1 Time Domain Analysis of the Model

The signals obtained for the healthy and different-sized abnormal regions of the 2D human respiratory system are presented separately for each microphone in Figures: 3.11-3.22. The signals were obtained by the time-dependent recording of the velocity vector normal to the human chest at selected microphone points through the numerical simulations. Microphone configuration and numbering are presented below the figures. Multiple transient analyzes were carried out by introducing 200, 400, and 600 Hz acoustic pressure waves of 1 Pascal magnitude to the bronchial airway. The duration of the signal was 0.1 s for each frequency. Time-step was taken as one-200Th of the period.

Results obtained from the microphone which is closest to the anomalous region (Mic No:4) in Figure 3.11 (d), Figure 3.15 (d), and Figure 3.19 (d) show that increasing the water pocket size causes a decrease in signal amplitude while creating a phase in the arrival time of the signals. This is because, in a steady state, the pocket of water acts as a sound barrier due to high impedance mismatch when the pocket size is larger than the wavelength but transmits the first signal to the nearest microphone, especially in the first few periods. This conclusion can be explained by the fact that the speed of sound in water is much higher than the speed of sound of the parenchyma tissue. This phase difference has been obtained for all frequencies, but the highest difference has been obtained at 600 Hz. On the other hand, increasing the frequency causes the signal amplitude to increase significantly for this microphone. However, in this study, attenuation was taken as a constant for all frequencies. Since attenuation is known to be proportional to frequency, this assumption is not correct. Therefore, it can be tricky to comment on this significant amplification of signals.

Figure 3.11 (c) and Figure 3.13 (c) show that the signals from the microphones (Mic No:3 and Mic No:11) placed just behind the rib cage bones contain too much noise and do not provide a harmonic, clean, and meaningful response for 200 Hz. Although this is valid for both microphones, the amount of noise is more significant for the microphone near the abnormal area. The noise disappears when we excite the system at relatively high frequencies, and no such behavior is observed in the results obtained from mentioned microphones (see Figure 3.15 (c), Figure 3.17 (c), Figure 3.19 (c), and Figure 3.21 (c)).

Transient and frequency domain analyses have been conducted to examine whether these abnormal regions act as sound sources or not, which is one of the leading research questions of the thesis. Assuming that it acts as a sound source, the highest response should be obtained at the microphones closest to this abnormal region, which are Mic No:3, Mic No:4, and Mic No:5 for 2D configuration. When we compare microphone signals with each other, Figure 3.13 (d) shows that in both cases of water pocket, the highest amplitudes have been obtained at Mic No: 12 for 200 Hz, which contradicts our assumption. For 400 Hz and 600 Hz, we have obtained responses with the highest amplitudes at Mic No:4 and Mic No:5 for some cases, as well as Mic No:12 (Figure 3.15, Figure 3.17, Figure 3.21, and Figure 3.23).

As a result, the amplitude information looks pretty complicated and random considering the obtained data. Obtaining more detailed information from the acoustic images that we have created using these signals would be more meaningful. In the next section, results obtained from Conventional Beamformer are presented and discussed. Before presenting them, we would like to mention the most crucial result over these signals: when we examined the first period of the signal, we saw that the first sound wave reached Mic No:4. This can be seen in Figure 3.23, Figure 3.24, and Figure 3.25 which present the acoustic pressure fields along the first period of the excitation. Results show that during the first period of the insonification, the abnormal region acts like a sound source. In addition, this situation was observed for all water pocket sizes and frequencies. When we investigated the changes in pressure fields as a result of changes in the frequency and size of the water pocket, we concluded that the phase difference becomes more noticeable as the frequency of the excitation and the size of the abnormal region increase. Based on the mentioned result, we can hypothesize that acoustic imaging methods may give a more sensitive and detailed image when using the first-period data obtained from high frequency and extensive abnormal region simulations.

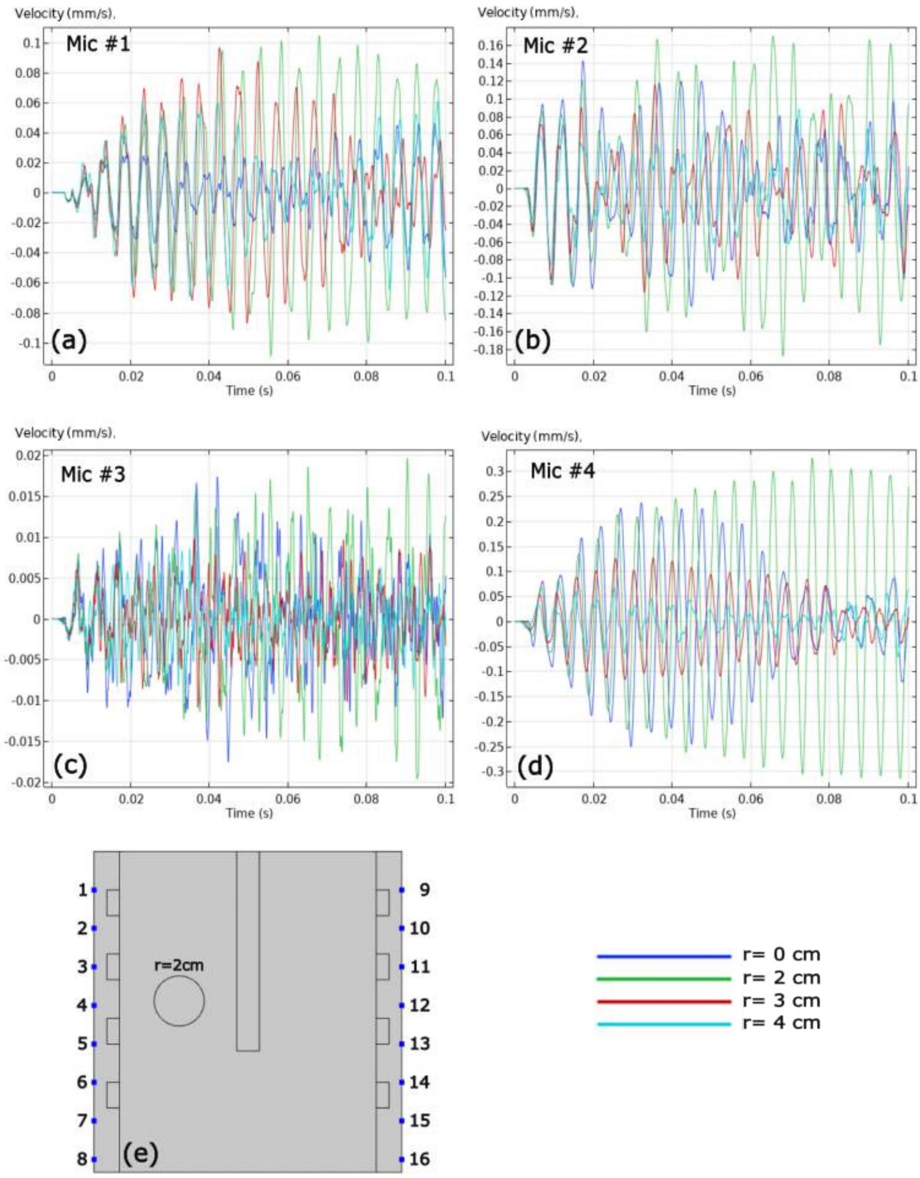

Figure 3.11: Obtained transient responses from the upper-left side of the chest model for 200 Hz ($\lambda_{lung} = 15cm$), considering the different sizes of the water pocket (r is the radius of the water pocket).

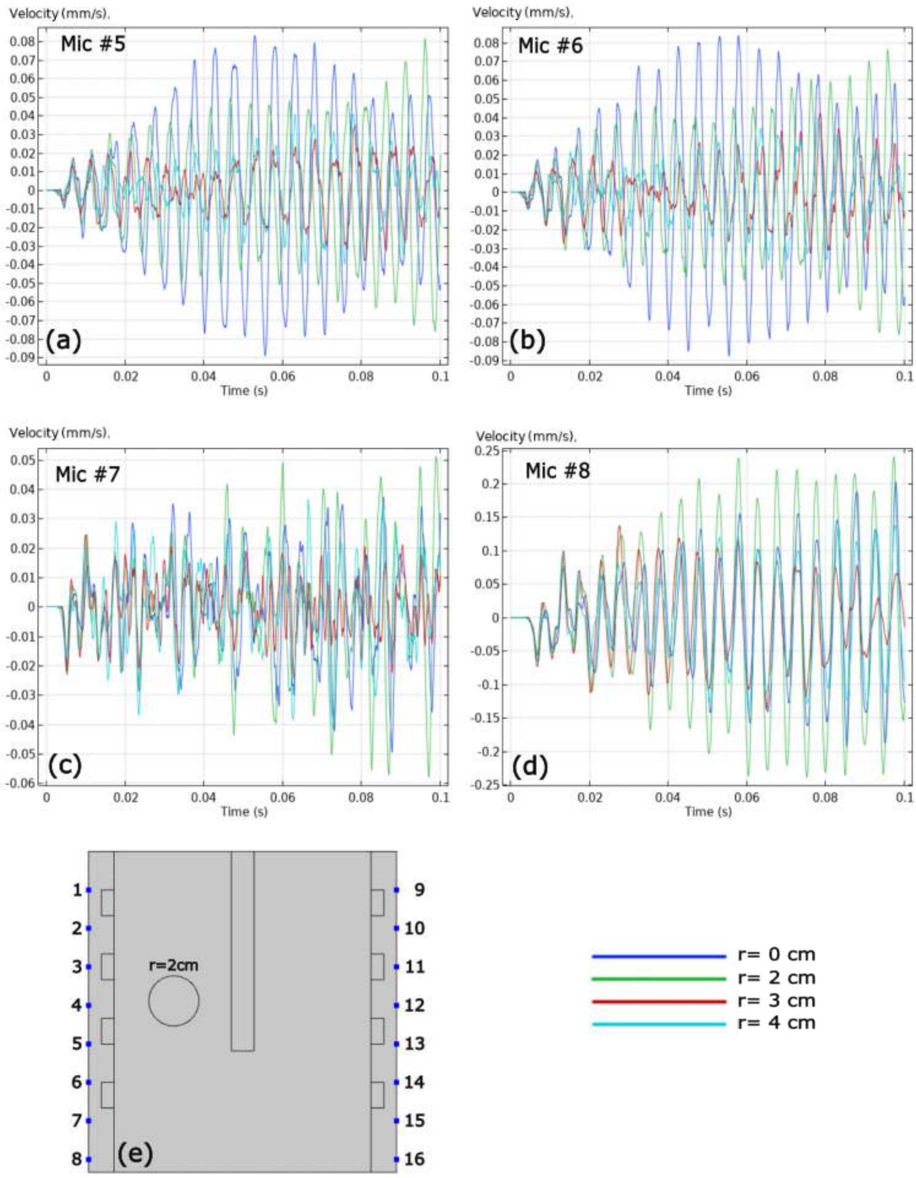

Figure 3.12: Obtained transient responses from the bottom-left side of the chest model for 200 Hz ($\lambda_{lung} = 15cm$), considering the different sizes of the water pocket (r is the radius of the water pocket).

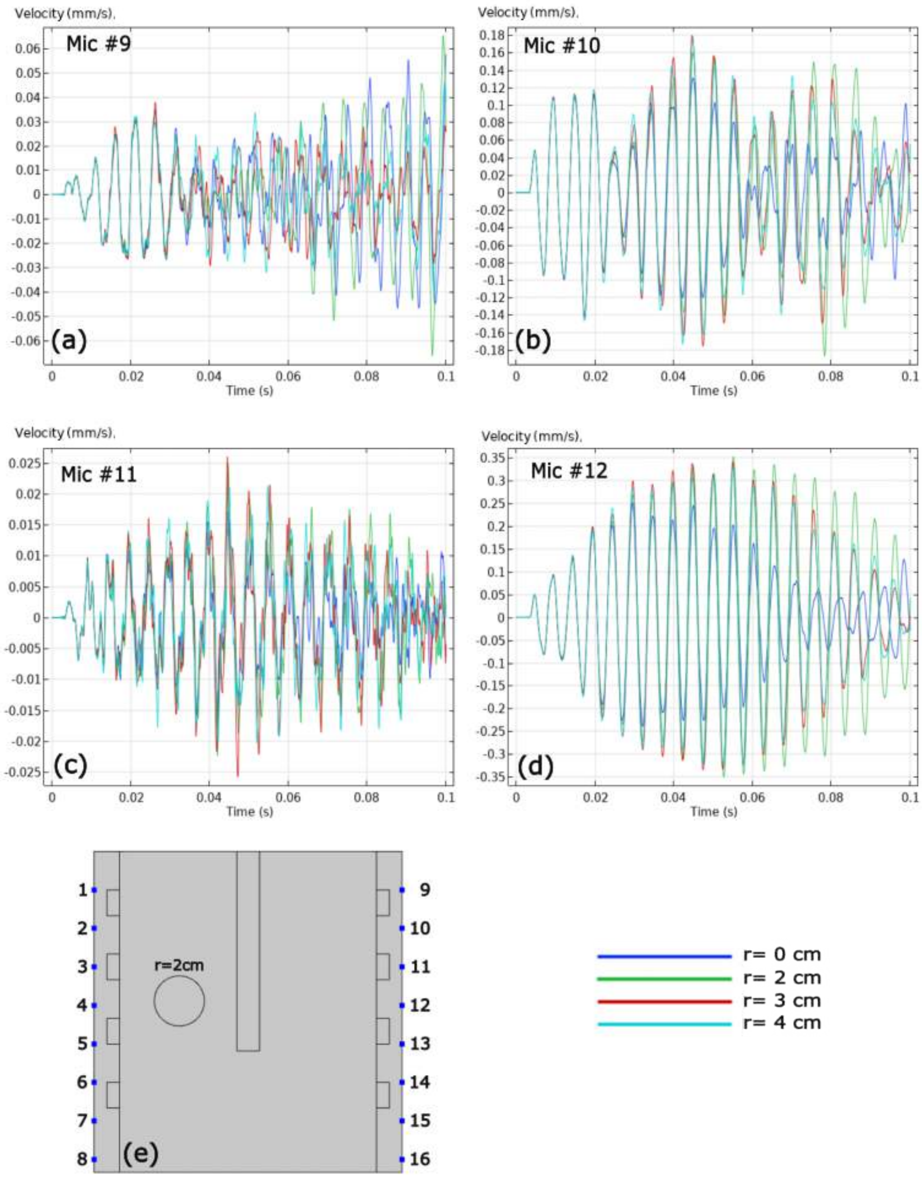

Figure 3.13: Obtained transient responses from the upper-right side of the chest model for 200 Hz ($\lambda_{lung} = 15cm$), considering the different sizes of the water pocket (r is the radius of the water pocket).

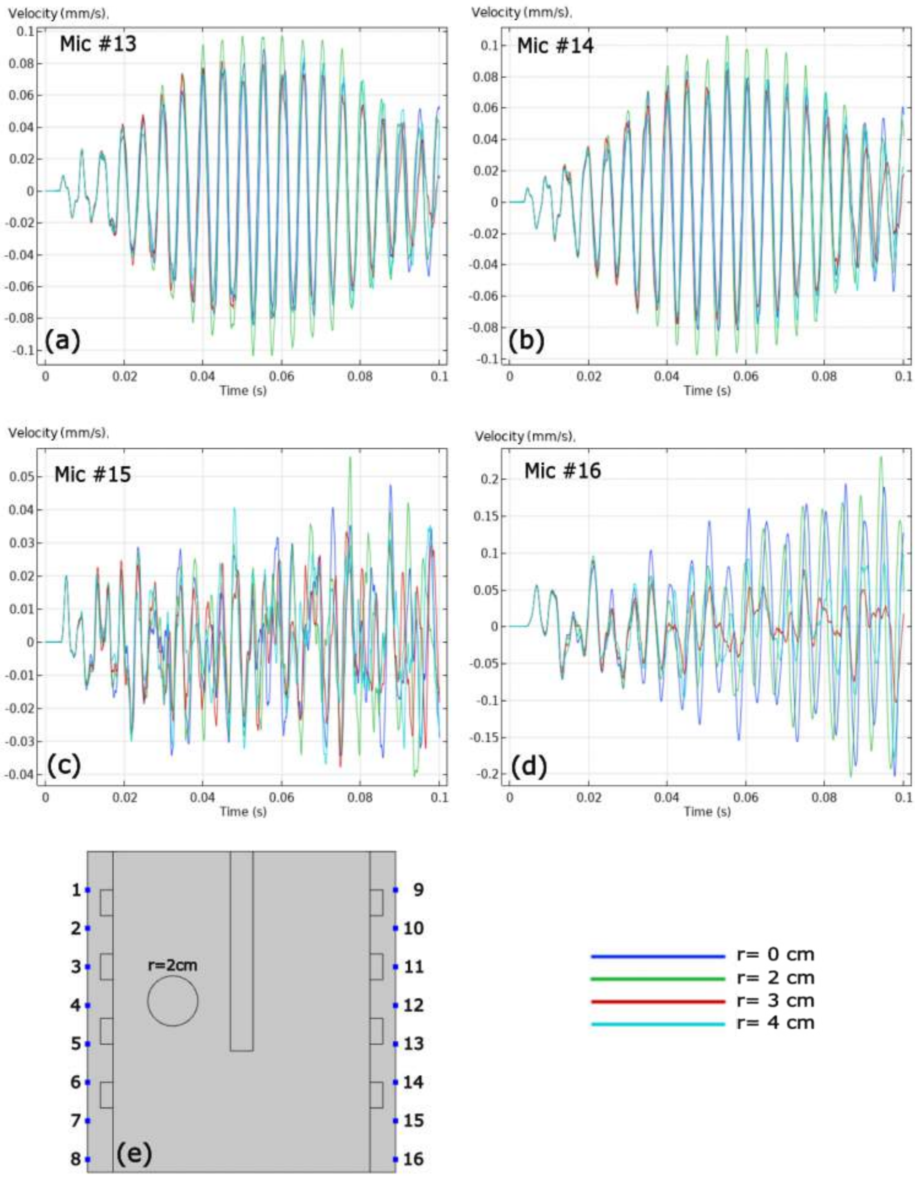

Figure 3.14: Obtained transient responses from the bottom-right side of the chest model for 200 Hz ($\lambda_{lung} = 15cm$), considering the different sizes of the water pocket (r is the radius of the water pocket).

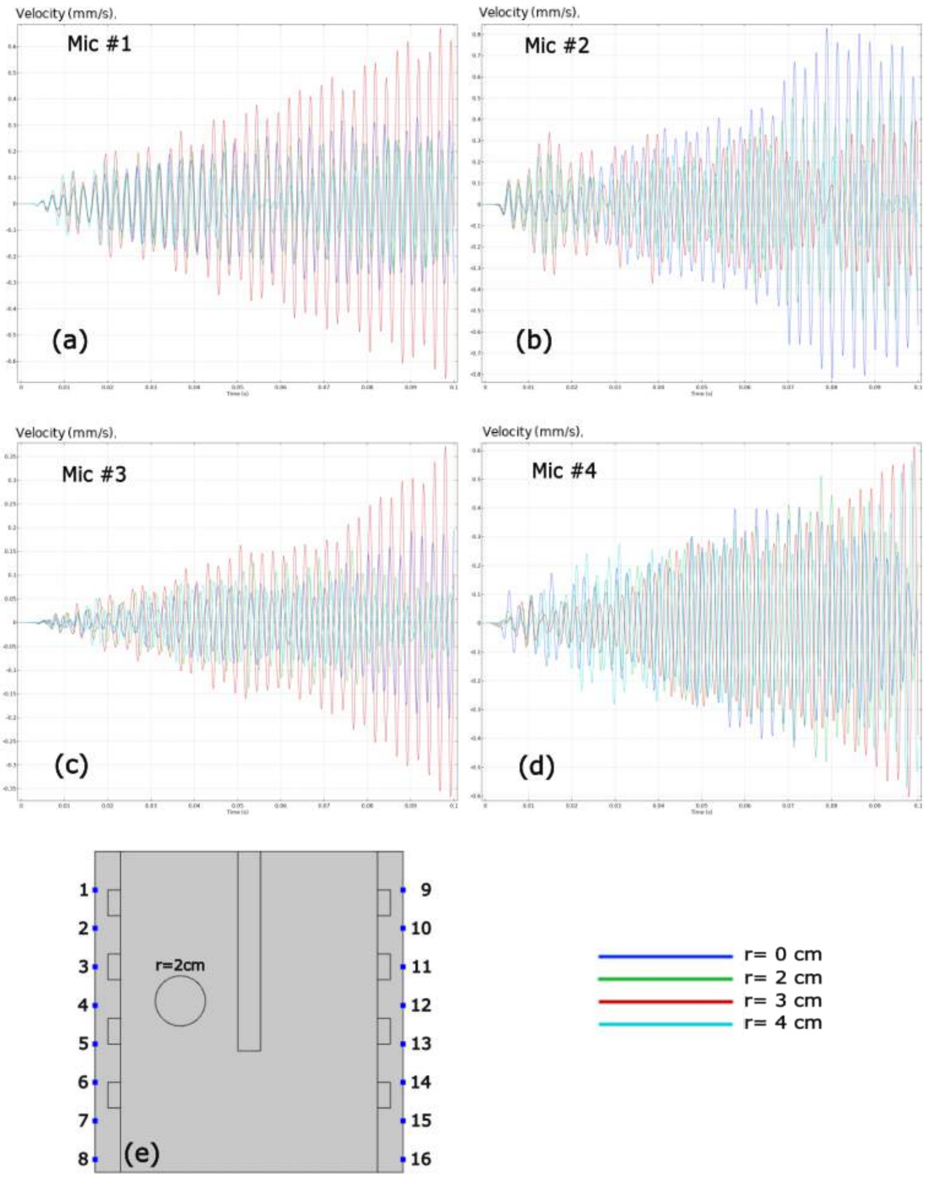

Figure 3.15: Obtained transient responses from the upper-left side of the chest model for 400 Hz ($\lambda_{lung} = 7.5cm$), considering the different sizes of the water pocket (r is the radius of the water pocket).

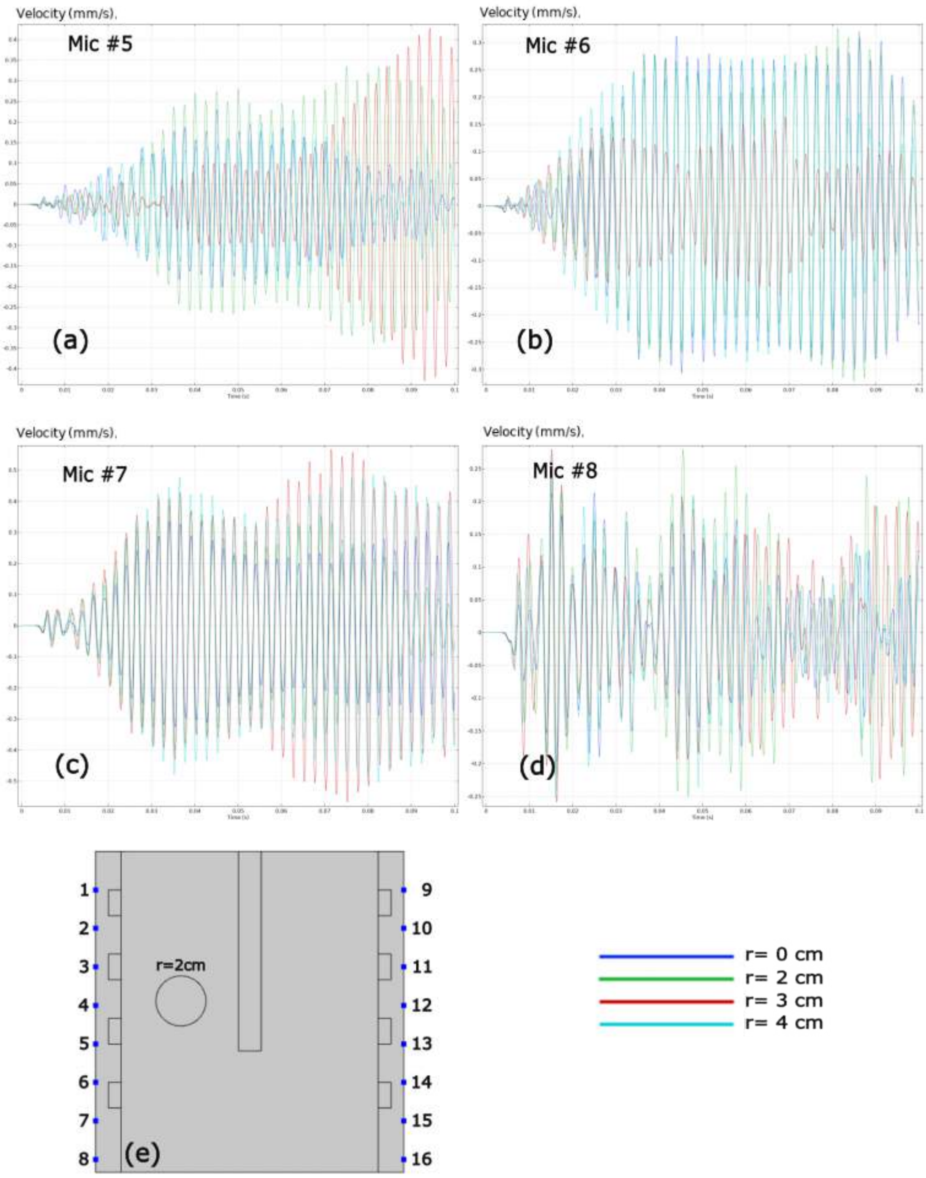

Figure 3.16: Obtained transient responses from the bottom-left side of the chest model for 400 Hz ($\lambda_{lung} = 7.5cm$), considering the different sizes of the water pocket (r is the radius of the water pocket).

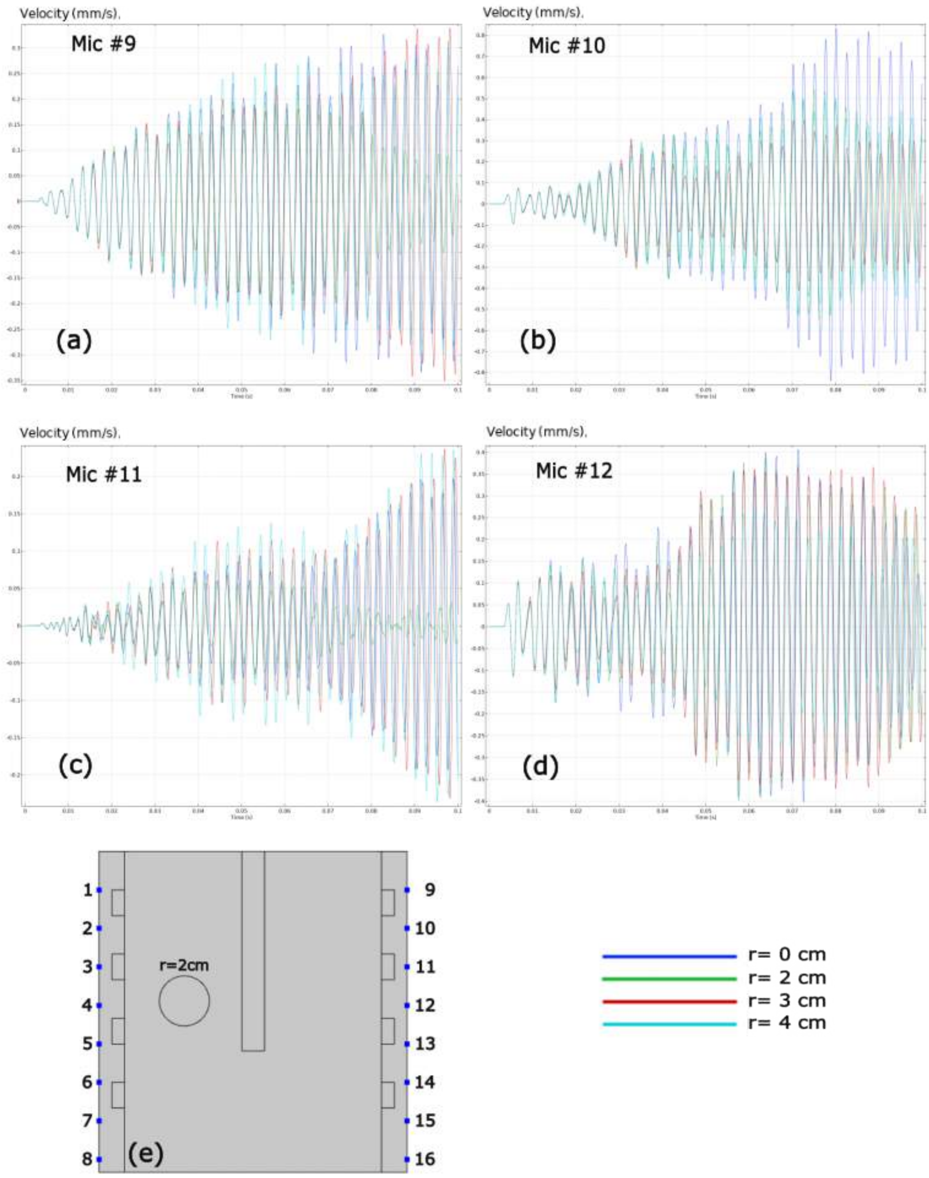

Figure 3.17: Obtained transient responses from the upper-right side of the chest model for 400 Hz ($\lambda_{lung} = 7.5cm$), considering the different sizes of the water pocket (r is the radius of the water pocket).

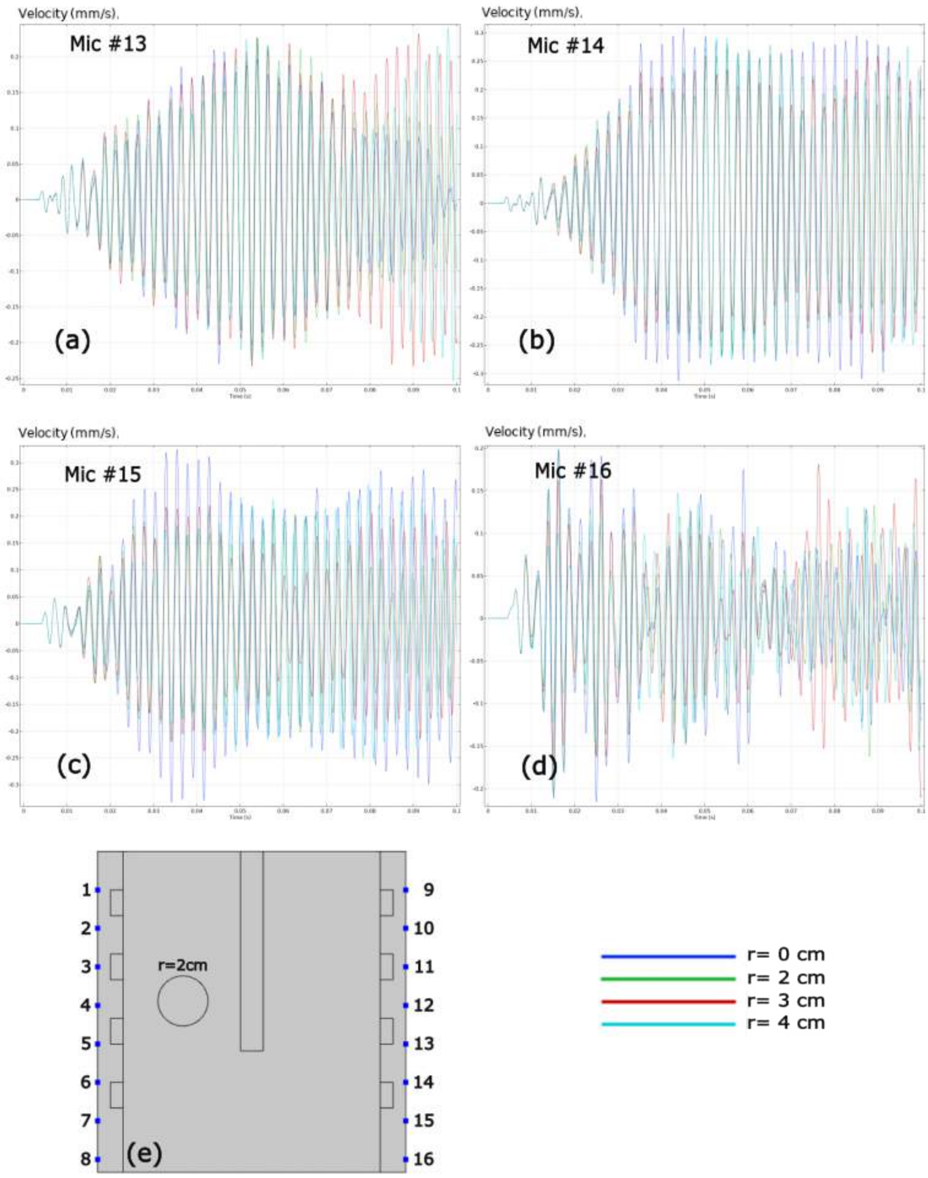

Figure 3.18: Obtained transient responses from the bottom-right side of the chest model for 400 Hz ($\lambda_{lung} = 7.5cm$), considering the different sizes of the water pocket (r is the radius of the water pocket).

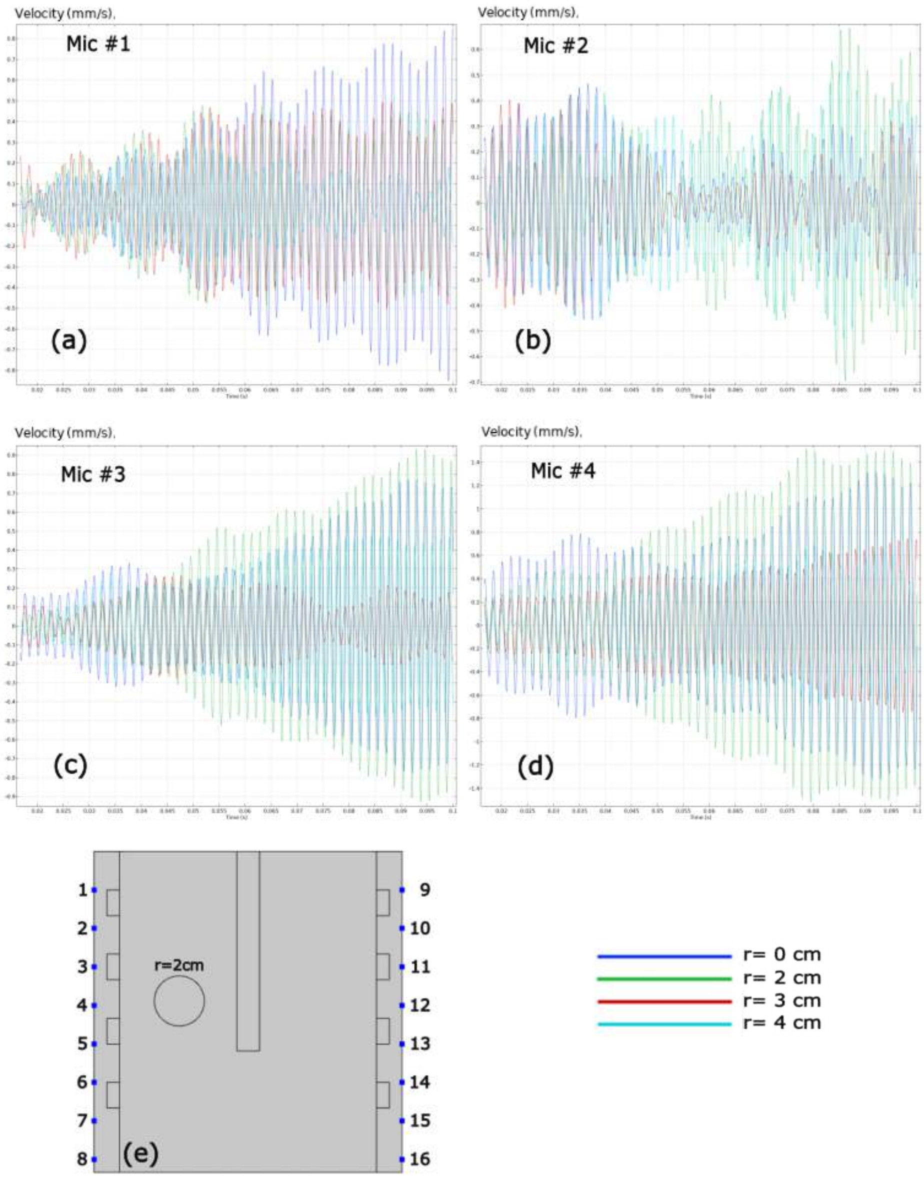

Figure 3.19: Obtained transient responses from the upper-left side of the chest model for 600 Hz ($\lambda_{lung} = 5cm$), considering the different sizes of the water pocket (r is the radius of the water pocket).

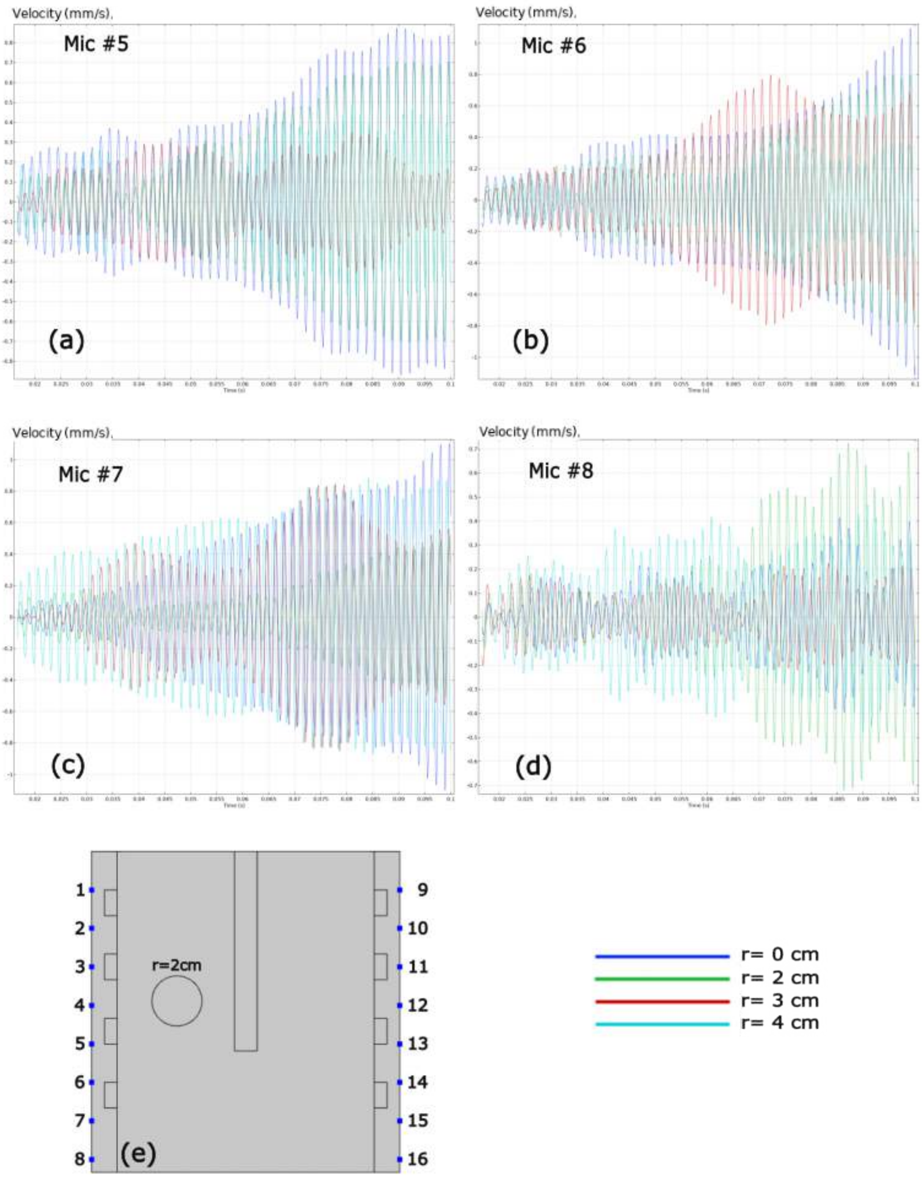

Figure 3.20: Obtained transient responses from the bottom-left side of the chest model for 600 Hz ($\lambda_{lung} = 5cm$), considering the different sizes of the water pocket (r is the radius of the water pocket).

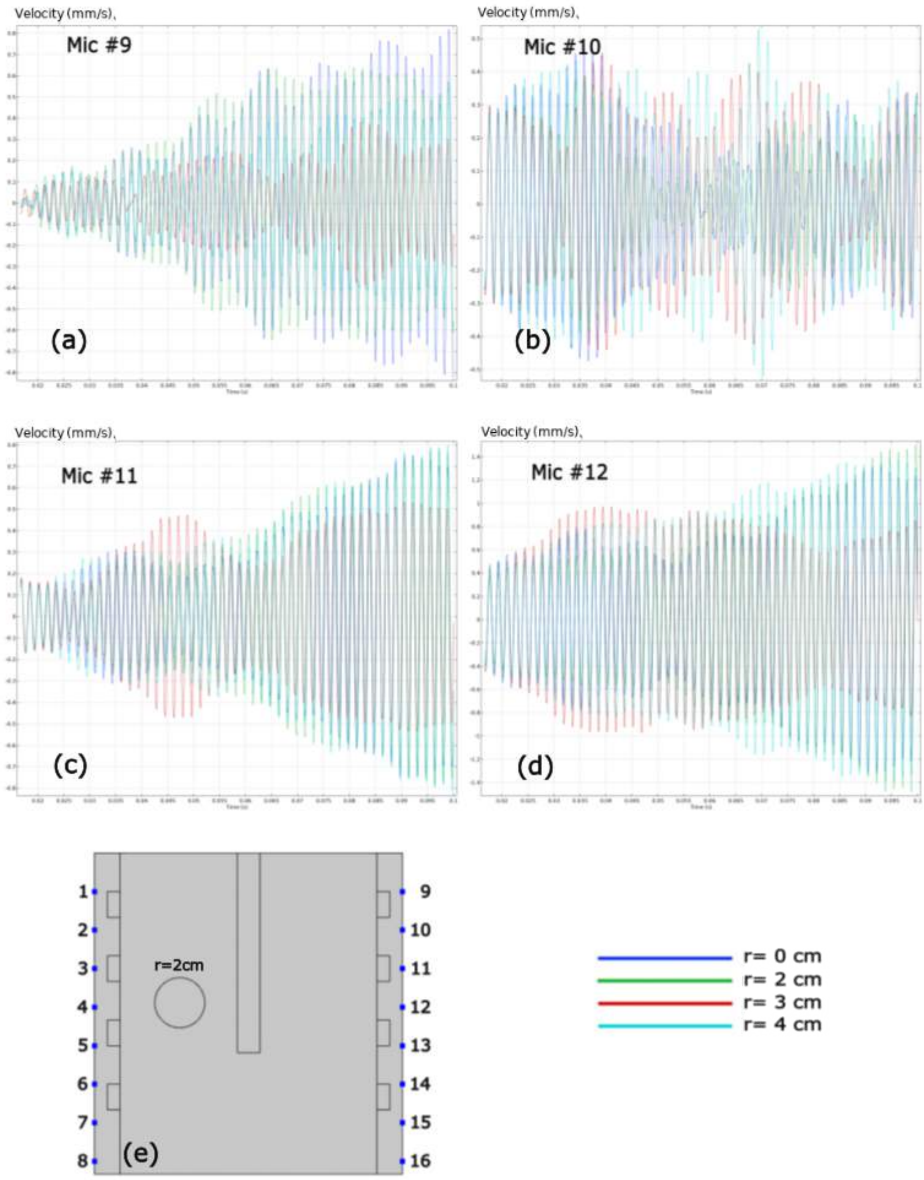

Figure 3.21: Obtained transient responses from the upper-right side of the chest model for 600 Hz ($\lambda_{lung} = 5cm$), considering the different sizes of the water pocket (r is the radius of the water pocket).

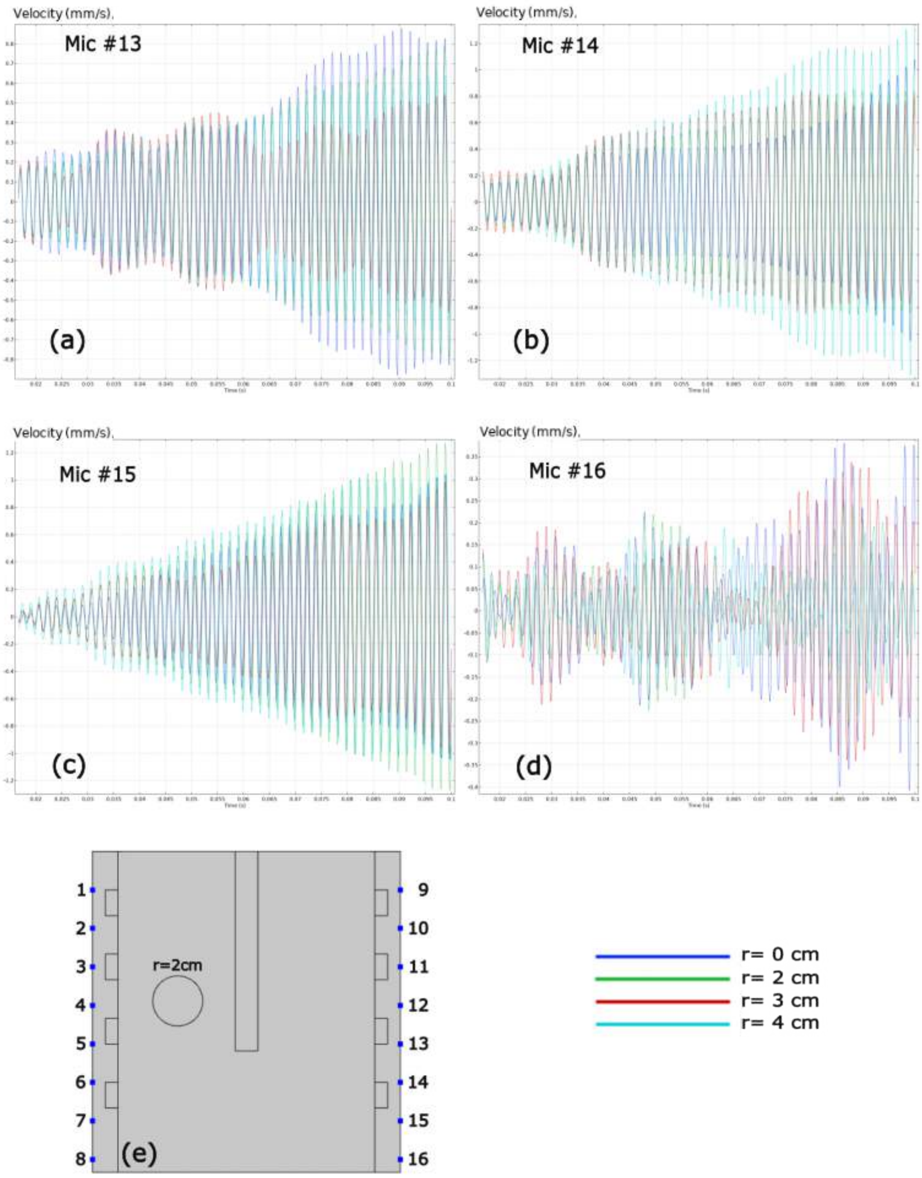

Figure 3.22: Obtained transient responses from the bottom-right side of the chest model for 600 Hz ($\lambda_{lung} = 5cm$), considering the different sizes of the water pocket (r is the radius of the water pocket).

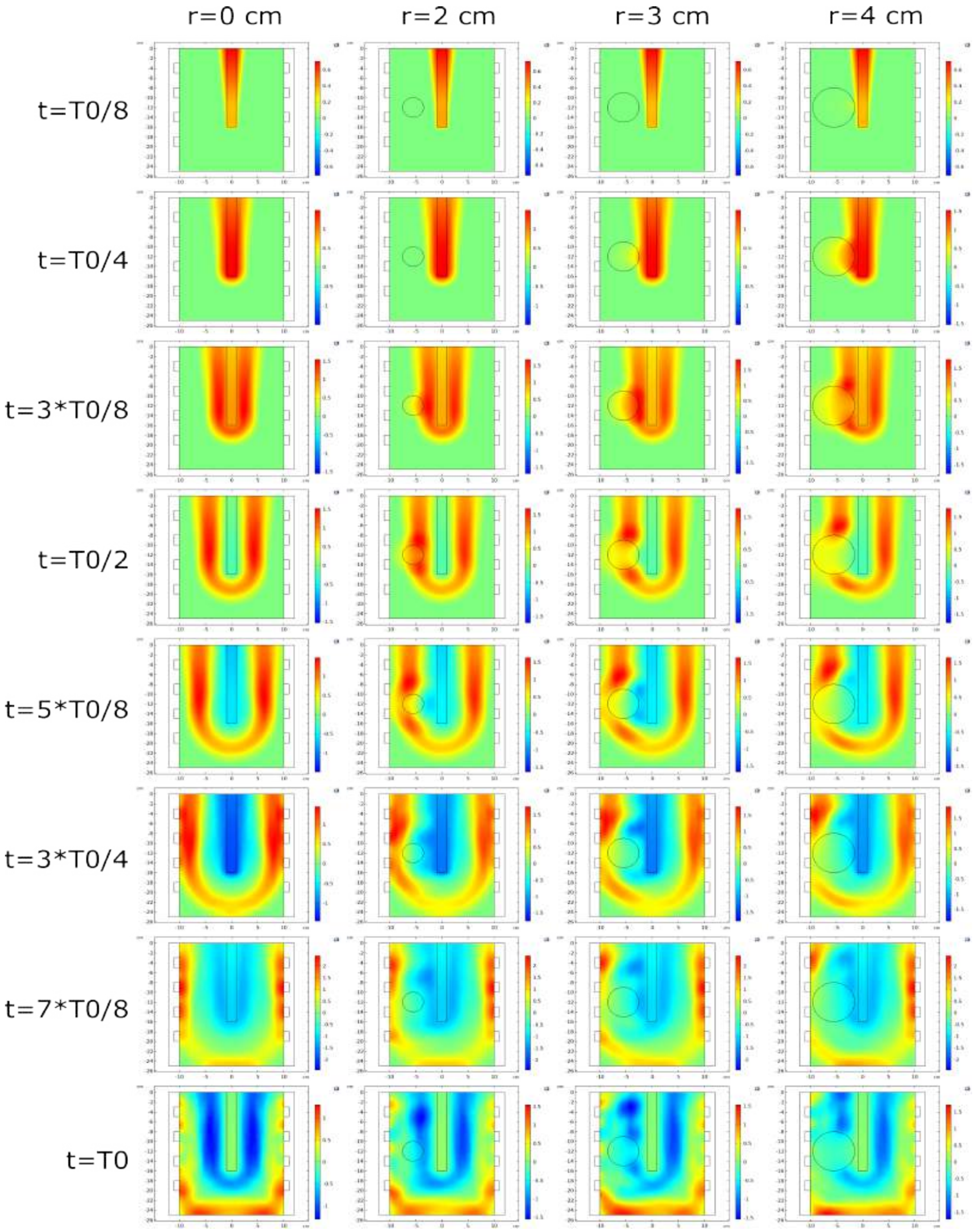

Figure 3.23: Acoustic pressure fields (SPL [dB]) during the first-period of excitation considering the different sizes of the water pocket (r is the radius of the water pocket, $f0 = 200Hz$, and $T0$ is the period of the signal where $T0 = 0.005s$). Dimensions are given in cm.

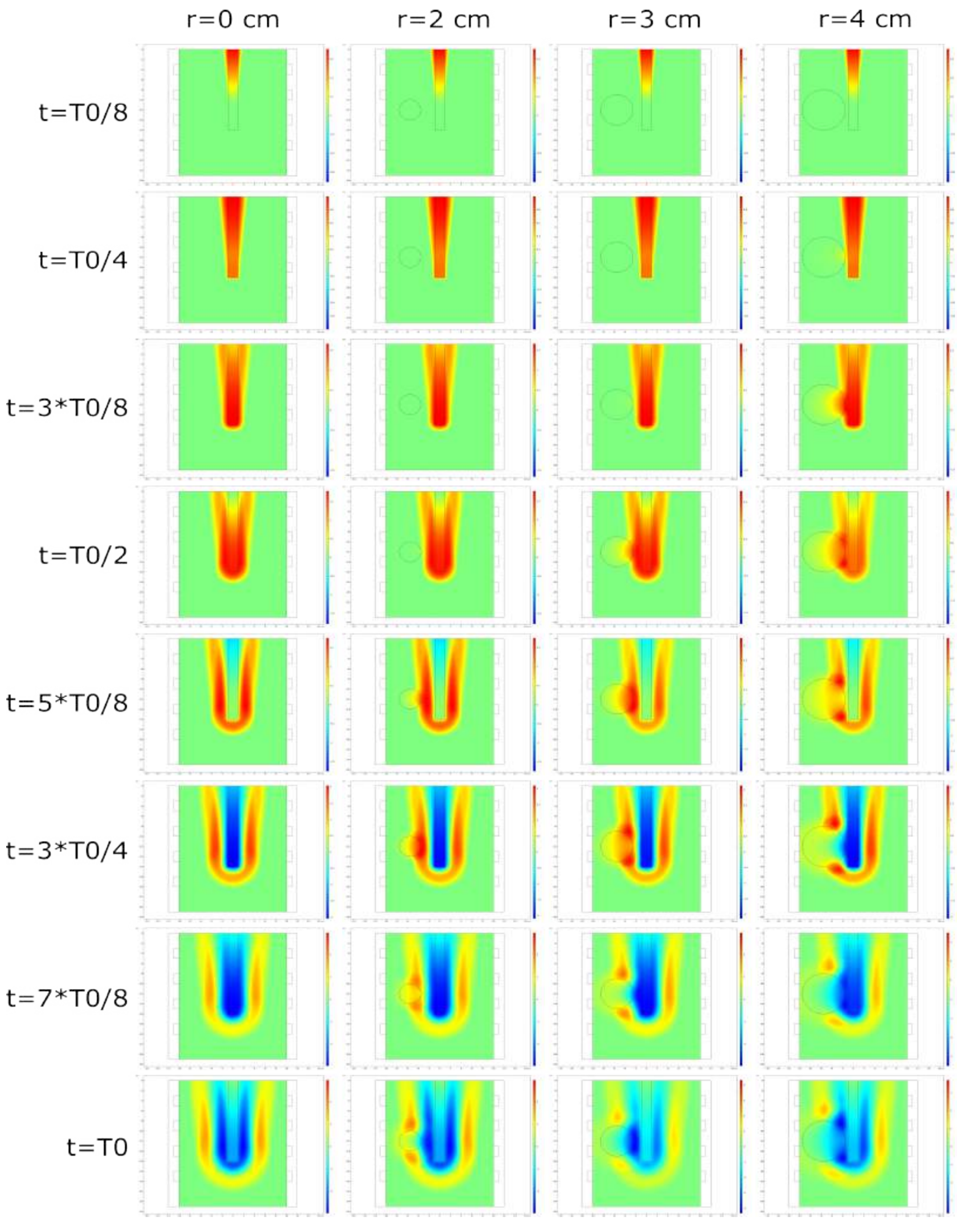

Figure 3.24: Acoustic pressure fields (SPL [dB]) during the first-period of excitation considering the different sizes of the water pocket (r is the radius of the water pocket, $f0 = 400Hz$, and $T0$ is the period of the signal where $T0 = 0.0025s$). Dimensions are given in cm.

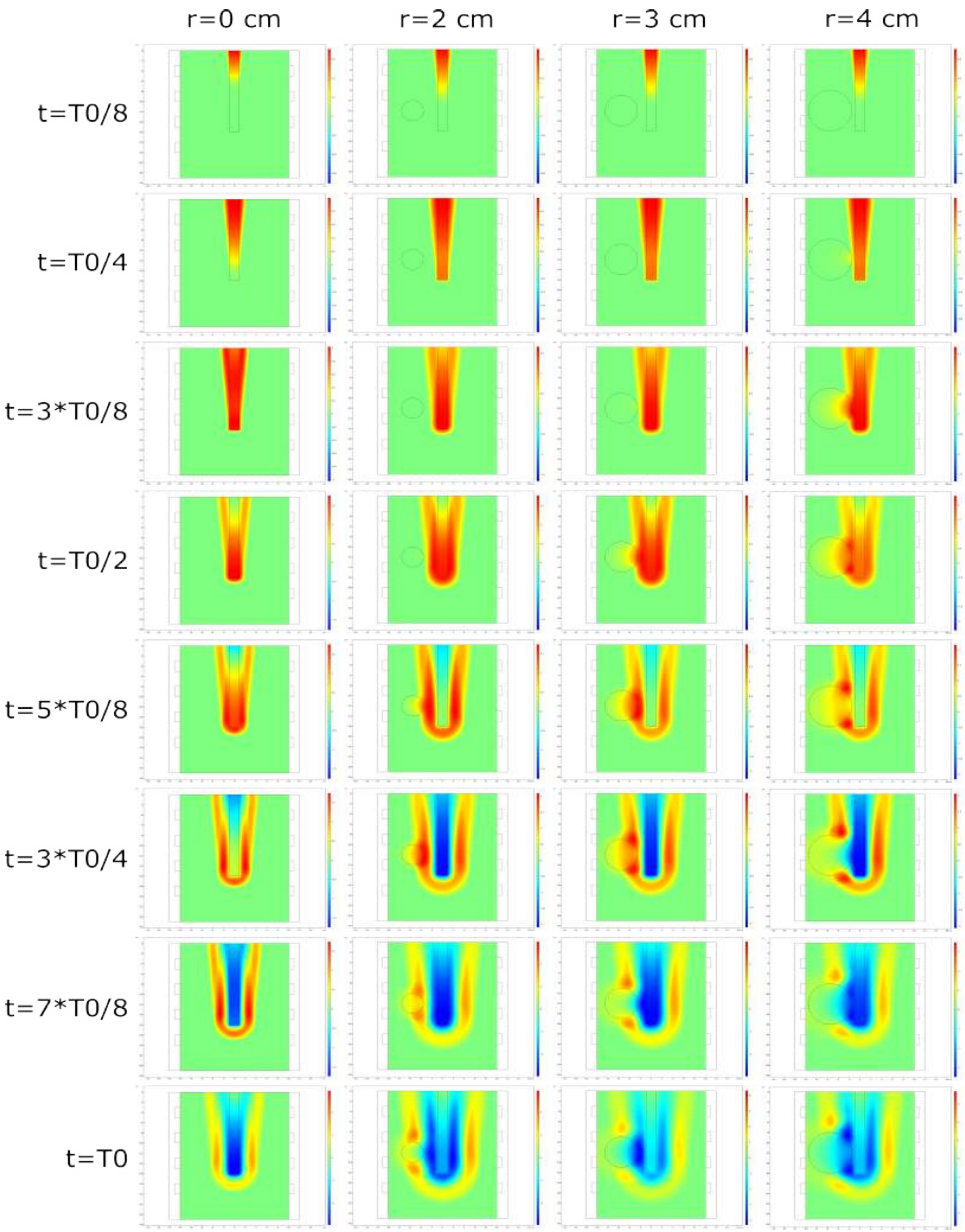

Figure 3.25: Acoustic pressure fields (SPL [dB]) during the first-period of excitation considering the different sizes of the water pocket (r is the radius of the water pocket, $f0 = 600Hz$, and $T0$ is the period of the signal where $T0 = 0.0016s$). Dimensions are given in cm.

3.3.2 Results of the Conventional Beamformer

Figure 3.26, Figure 3.27, and Figure 3.28 show the acoustic images of the human chest processing the signal over 0.1 seconds for different pocket sizes and frequencies. The time-domain response was transformed to the frequency-domain using a Fast-Fourier Transform before processing through the beamformer. The sampling rate was taken as one-200Th of the period, and the speed of sound was taken as 40 m/s, considering the non-homogeneity of the region. Attenuation of the acoustic waves within the parenchyma was neglected. The dynamic range of the results was taken as 3-6 dB considering the attenuation of the lung. Each column of the figures represents the different steering vector formulations (for example, "I" corresponds to the Formulation I mentioned in section 2.2.1.1).

First of all, it was observed from Figure 3.26, Figure 3.27, and Figure 3.28 that only Formulation I and Formulation IV present an observable pressure field among the steering vector formulations, while Formulation II and Formulation III do not provide proper pressure distribution of the region in all cases. They only gave source strength assuming the source was placed at the center of the region. The source strengths obtained with Formulation II and Formulation III were close, but when we consider the amplitude of the source strength, it is not realistic. Also, discussing the source strength results might be tricky because we used velocity data as an input instead of pressure data.

For healthy subjects (i.e., r=0 cm), Formulation I and Formulation IV presented the expected result, a symmetrical pressure distribution at all frequencies. Figure 3.26 shows that Formulation I gave more accurate information about the location of the water pocket when the radius is 4 cm. For the anomalous region with a 2 cm radius, the results of both formulations were pretty similar for 200 Hz. Figure 3.27 reveals that Formulation I and Formulation IV reflected an abnormal region as a sound source. However, many side lobes appeared in the field, which made it impossible to identify the region. Figure 3.28 shows that both formulations failed to localize the abnormal area through the acoustic images.

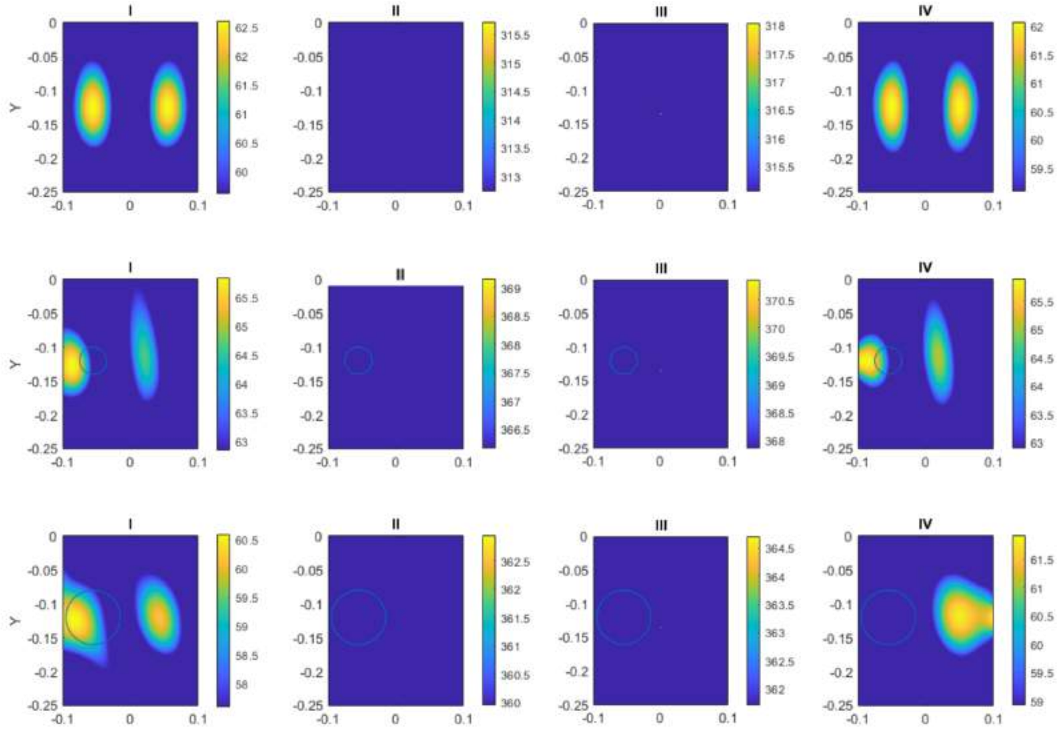

Figure 3.26: Acoustic pressure fields (SPL [dB]) obtained by processing signals of 0.1 seconds length at 200 Hz through Conventional Beamformer by using four different steering vector formulations (each column represents each formulation, each row presents the different cases (from up to down: healthy, 2cm water pocket and 4 cm water pocket). Dimensions are given in m.

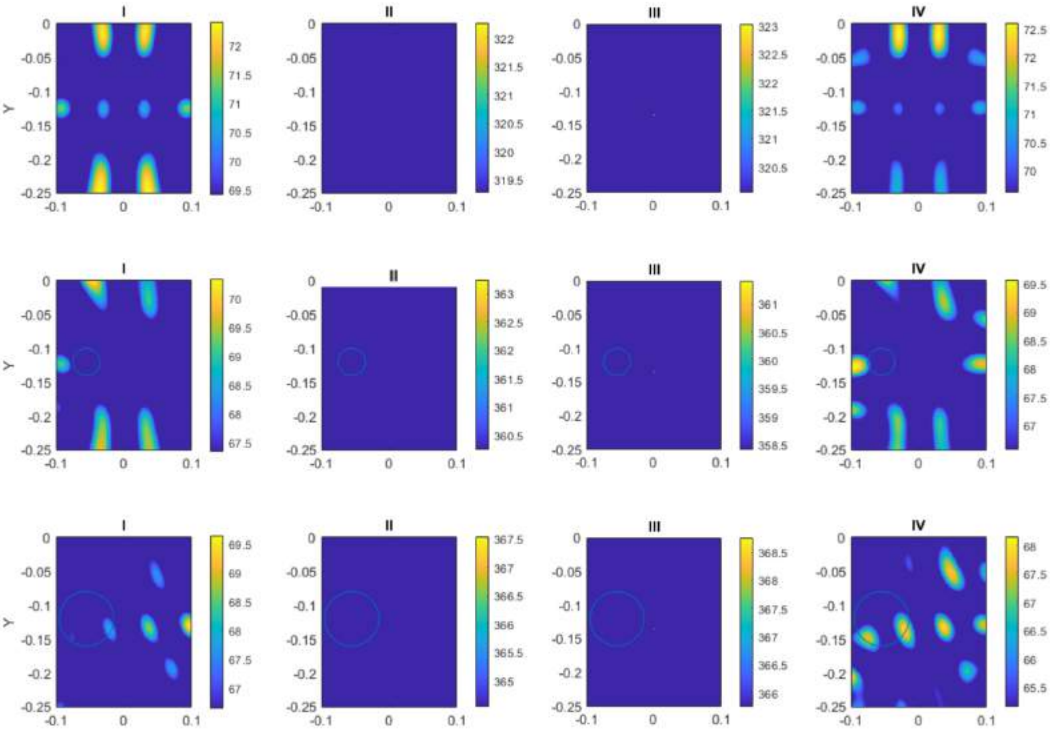

Figure 3.27: Acoustic pressure fields (SPL [dB]) obtained by processing signals of 0.1 seconds length at 400 Hz through Conventional Beamformer by using four different steering vector formulations (each column represents each formulation, each row presents the different cases (from up to down: healthy, 2cm water pocket and 4 cm water pocket). Dimensions are given in m.

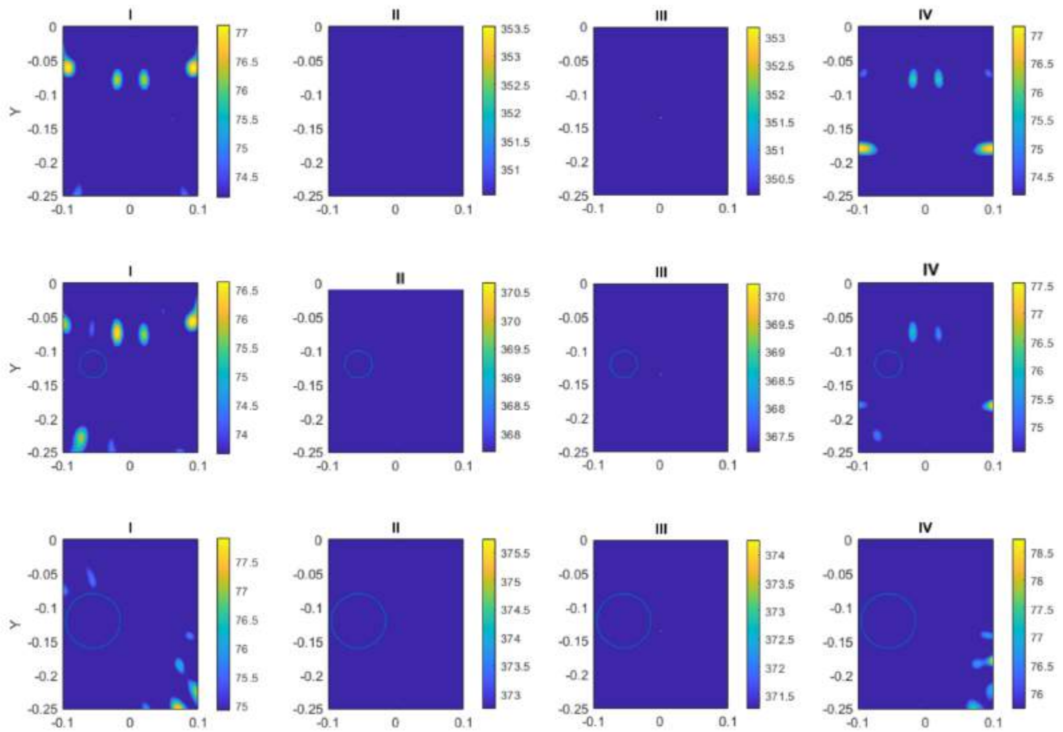

Figure 3.28: Acoustic pressure fields (SPL [dB]) obtained by processing signals of 0.1 seconds length at 600 Hz through Conventional Beamformer by using four different steering vector formulations (each column represents each formulation, and each row presents the different cases (from up to down: healthy, 2cm water pocket and 4 cm water pocket). Dimensions are given in m.

Conventional Beamformer has not provided stable and meaningful results so far. Considering the frequency of the insonification and the abnormal region's size, we could not obtain any patterns or significant correlations between the pressure fields. The method presented complex and random results to correlate and interpret, like the signal results in the previous section when we used 0.1 seconds of the signal. In the following figures, pressure fields are presented using the first period of each case instead of processing the complete signal. We used such a short signal because we have seen noticeable phase differences between the arrival time of the acoustic waves at the beginning of the excitation, which was explained in detail in the previous section (see Figure 3.23, Figure 3.24, and Figure 3.25).

Figure 3.29, Figure 3.30, and Figure 3.31 show similar results when we process short signals instead of long signals using Formulation II and Formulation III. However, the results from Formulation I and Formulation IV show that they differed significantly from both previous results, and the pressure fields are also very different. Figures show that Formulation 4 predicted the position of the abnormal region up to a certain degree in each case. In contrast, the results presented by Formulation 1 referred to the opposite field as the sound source. It can be seen from the figures that Formula IV provided more accurate images in terms of localization of the region when we increased the frequency and the pocket size.

For the first time, we have obtained meaningful results, implying that Formulation IV can be used to locate the abnormal region. Of course, many parameters that might affect the results, such as frequency, sampling rate, number and position of microphones, and mechanical properties of the abnormal region, have not been taken into account up to now. To understand the effect of these parameters and to reveal the potential of the method, a lot of comparative studies should be done on the numerical and experimental models, but for now, it can be said that this method helps us to narrow the field of interest for the 2D configuration even though it does not give an exact location. In addition, It can be seen in Figure 3.32 (b), Figure 3.32 (c), and Figure 3.32 (d) that Formulation IV gave good and stable results for the different locations of the abnormal region when it was placed between the bronchial airway and the rib cage.

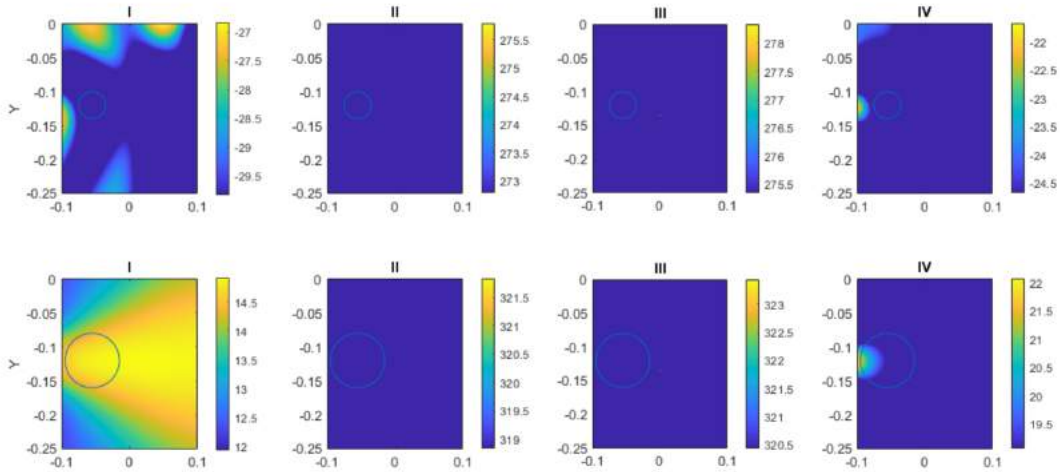

Figure 3.29: Acoustic pressure fields (SPL [dB]) obtained by processing signals of 0.003 seconds length at 200 Hz through Conventional Beamformer by using four different steering vector formulations (each column represents each formulation, and each row presents the different cases (from up to down: water pocket with a radius of 2 cm and 4 cm). Dimensions are given in m.

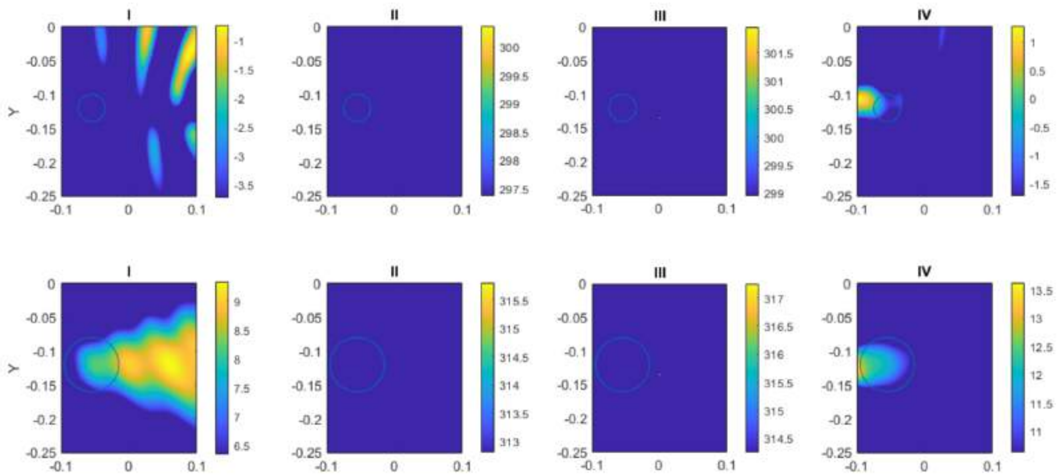

Figure 3.30: Acoustic pressure fields (SPL [dB]) obtained by processing signals of 0.003 seconds length at 400 Hz through Conventional Beamformer by using four different steering vector formulations (each column represents each formulation, and and each row presents the different cases (from up to down: water pocket with a radius of 2 cm and 4 cm). Dimensions are given in m.

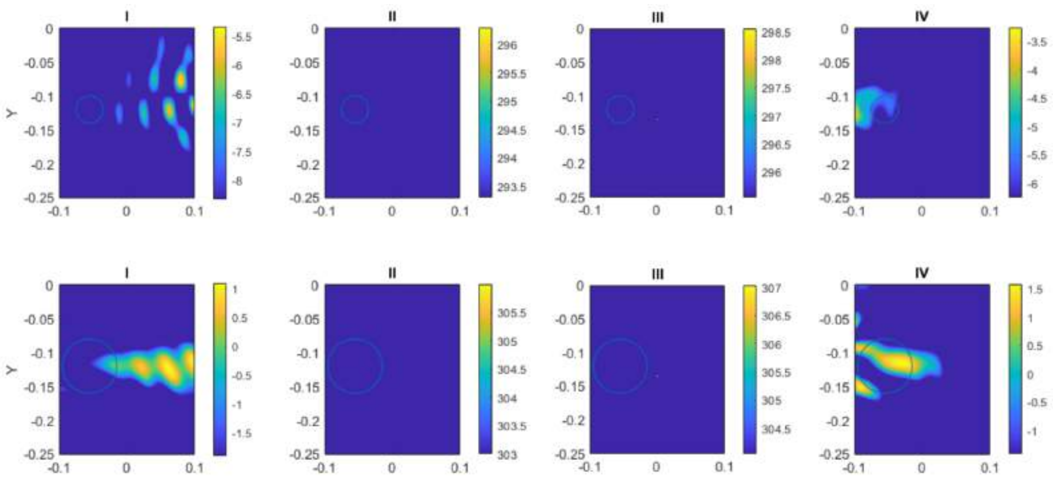

Figure 3.31: Acoustic pressure fields (SPL [dB]) obtained by processing signals of 0.003 seconds length at 600 Hz through Conventional Beamformer by using four different steering vector formulations (each column represents each formulation, and each row presents the different cases (from up to down: water pocket with a radius of 2 cm and 4 cm). Dimensions are given in m.

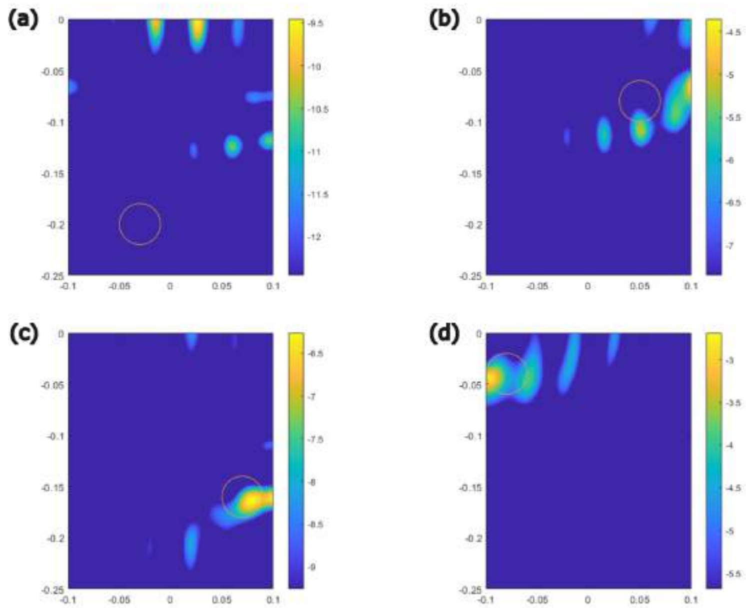

Figure 3.32: Acoustic pressure fields (SPL [dB]) obtained by processing signals of 0.0016 seconds length at 600 Hz through Conventional Beamformer by Formulation IV for different locations of the abnormal region. Dimensions are given in m.

3.3.3 Frequency Domain Analysis of the Model

The microphone configuration of the frequency domain analysis was the same as the one used in the previous section. In the numerical simulations, a pressure wave with 1 Pascal magnitude was introduced to the bronchial airway, and velocity normal to the y axis was measured from all measurement points.

Figure 3.33 shows the frequency-dependent velocity response of the selected points (Mic No:2, 4, 6, 10, 12, and 14) from the left and right sides of the 2D model. The results obtained from Mic No:10, Mic No:12, and Mic No:14 show that the body's right side was not affected by the presence of the water pocket at low frequencies; visible changes were observed at 500 Hz and above, starting from the first natural frequency. Results obtained from Mic No:2, Mic No:4, and Mic No:6 show that above 550 Hz, increasing the pocket size resulted in a decrease in the response. Most observable changes were observed at Mic No:4 for relatively high frequencies, which is the closest microphone to the abnormal region. Between 400 Hz-500 Hz, a 4 cm water pocket created a very high response, especially at Mic No:2 when we compare it with other cases. The highest amplitudes were obtained in microphones placed in the middle of the body (Mic No:4 and Mic No:12), which can be explained by the propagation of sound waves first in the bronchial airway and then in the parenchyma region.

Figure 3.34 shows the steady-state pressure field for different frequencies and pocket sizes. For 100 Hz, the presence of a water pocket increased the amplitude on both sides of the torso. This increase in amplitude was also proportional to the size of the pocket. We did not see any significant difference between healthy and 2 cm water pocket cases for 200 Hz. However, in the 4 cm case, the pressure field indicates that the abnormal region acted as a sound barrier, so the amplitudes on the left side of the torso were lower than in other cases. The pressure fields for 300 Hz, 400 Hz, 500 Hz, and 600 Hz reveal that the sound barrier effect of the water pocket was again valid and became dominant by increasing the pocket size. In cases other than 100 Hz, there was no significant change on the right side of the region.

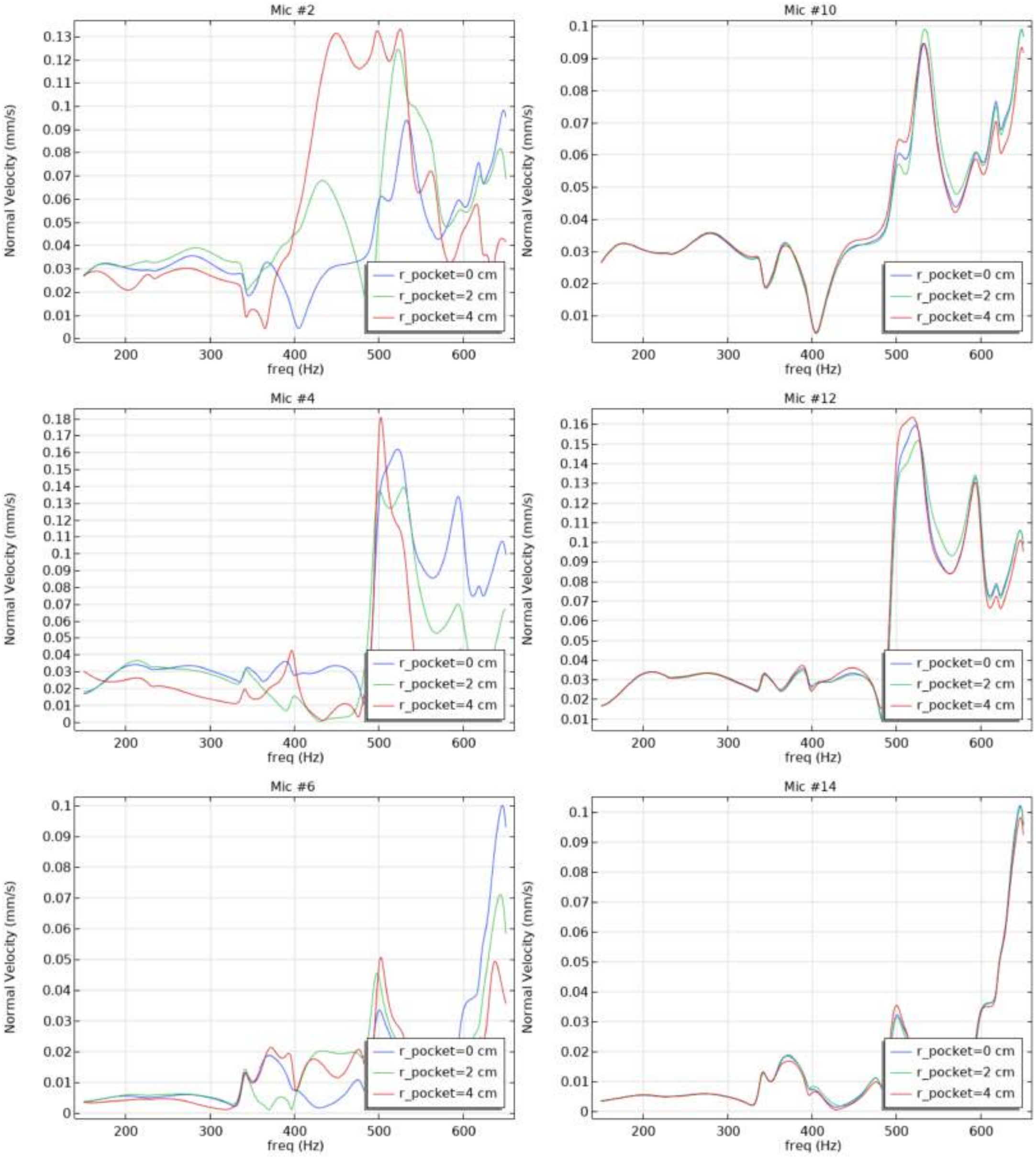

Figure 3.33: Frequency-dependent velocity responses of the selected points.

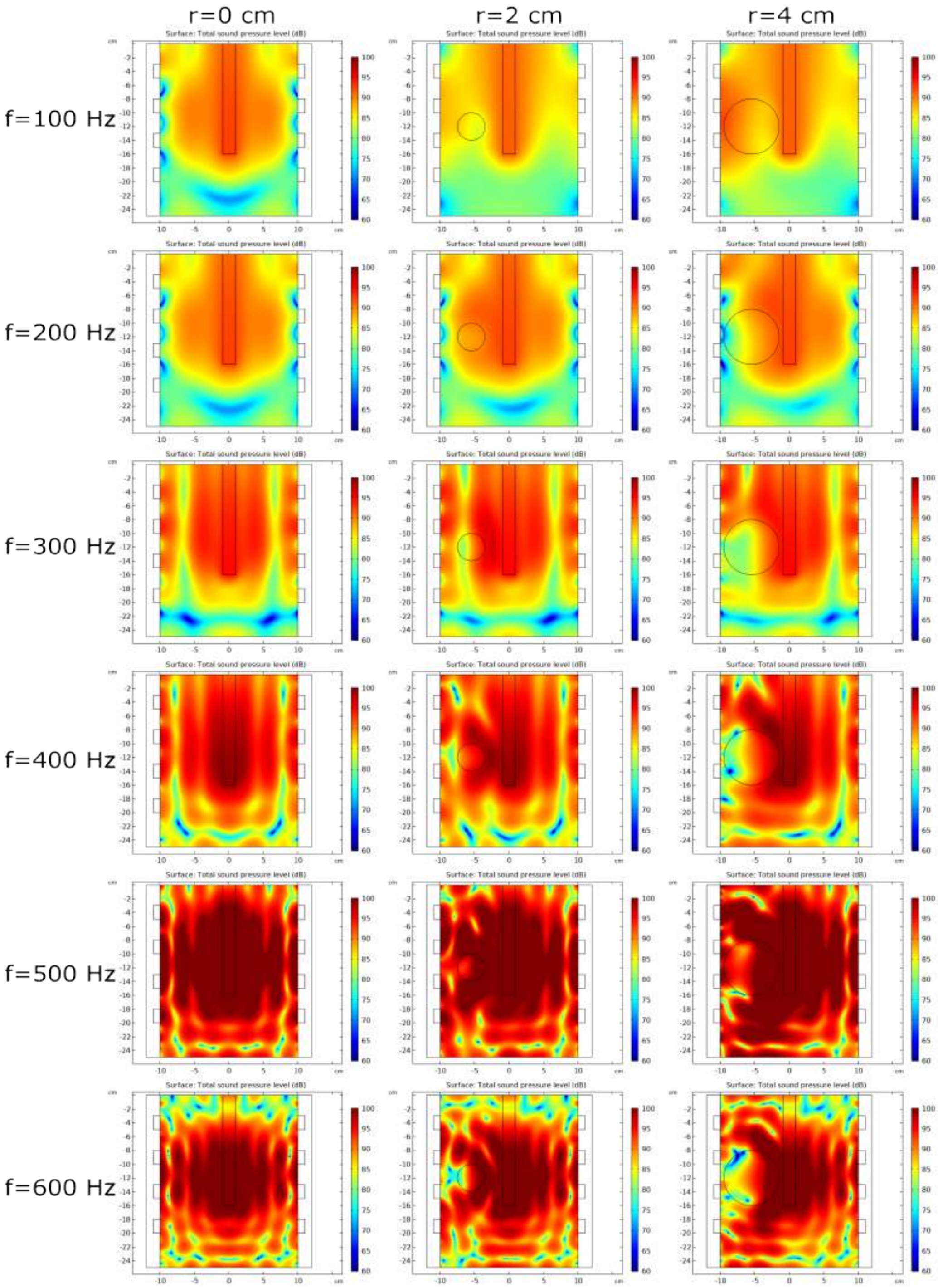

Figure 3.34: Steady-state acoustic pressure fields (SPL [dB]) of the 2D model for different frequencies and pocket sizes. Dimensions are given in cm.

3.3.4 Results of Matched-Field Processors

In this section, we present the results obtained through two different Matched-Field Processors: The Linear Processor and The Minimum Variance Distortionless Response (MVDR). The basic idea behind this technique is simply the comparison of the two different data sets to see if they are similar to each other or not, which we call experimental and replica data sets in this study. Ideally, the experimental data set should contain the steady-state response of the unhealthy human or animal, and replica data set might be obtained using different approaches. In this section, presented results were acquired by processing both experimental and replica data sets, which were obtained through numerical simulations. The distance between grid points used to create the replica data set was taken as 1 cm for each case.

Figure 3.35, Figure 3.36, and Figure 3.37 present the results for 200 Hz, 400 Hz, and 600 Hz, respectively, to investigate the two main questions: can we express the acoustic field within the lungs and the airways using multiple monopole sound sources, and can the abnormality be appeared as a region with high sound intensity? The first columns of the (subfigures (a), (b), and (c)) show the output of the Linear Processor, and the latter columns (subfigures (e), (b), and (c)) show the results of the MVDR. For 200 Hz, the water pocket did not significantly affect the Linear Processor's output significantly, while the bronchial airway became more visible in the output of the MVDR when we increased the size of the water pocket (see Figure 3.35). Figure 3.36 (a), (b), and (c) show that the region above the pocket has appeared as the sound source, and the region with high intensity became more local when we increased the size of the pocket. Figure 3.36 (d), (e), and (f) show that for the high radius of the water pocket, a more intense region has appeared only within the airway next to the abnormal region. In Figure 3.37 (a), (b), and (c), The Linear Processor reveals that the abnormal region acted as a sound barrier at 600 Hz. That behavior can also be observed in the previous results. The right column of the figure shows that the MVDR did not present meaningful results for the 600 Hz.

The results of the Linear Processor show that we can express the acoustic field with multiple monopole sound sources, especially in healthy situations. MVDR offers narrower but less significant acoustic fields for all cases. This output is expected as the method compresses the side lobes that may carry important information about the medium. Considering the acoustic imaging of the 2D model, results show that the performance of the Linear Processor was more robust than the MVDR, and the results were very similar to steady-state results of the 2D model (see the previous section). However, none of the methods accurately indicated the location of the water pocket. We can say that water pockets did not appear as a sound source in the acoustic field results presented by these techniques to answer the second question.

Matched-field methods have not yielded a good result for diagnostic purposes so far. However, we noticed that these techniques generally check how similar two different data sets are to each other and do not interest in what data sets contain. According to the literature, creating numerical models of the human respiratory system with various diseases and performing acoustic analysis is achievable. Based on this achievement, we can assume that we can create replica data sets for different positions and sizes of water pockets to process signals obtained from unhealthy persons for diagnostic purposes.

At this point, we do not have experimental results available as we are investigating the potential of acoustic imaging techniques. Instead of experimental results, we have used the available numerical results by adding specific errors. Our aim in doing this was to check the processors' tolerances and performances against errors by creating a mismatch between experimental and replica data sets. These mismatches were obtained by changing simulation parameters. Figure 3.38, Figure 3.39, and Figure 3.40 present the results of cases with errors for 200 Hz, 400 Hz, and 600 Hz, respectively. The Left and right columns of the figures present the results of the Linear Processor and the MVDR, respectively. Figures only show the grid point with the highest output of each processor since, according to the theory, the highest output of the methods shows the result with the maximum likelihood result. As our aim is to locate the center of the water pocket, rather than to create the image of the acoustic field, the location of the point with the highest probability was presented. In subfigures (a), (b), (e), and (d), replica data sets were created using all possible positions of the 2 cm water pocket. In subfigures (c), (d), (g), and (h), we have used the 4 cm water pocket to generate replica data sets. The first and fourth rows of the subfigures present the results when we placed the water pocket at a point that was not included in grid points of replica data sets. The second and third rows present the results when we processed data sets that have a mismatch in pocket sizes and location (for subfigures (b) and (f), radius of the pocket sizes are taken as 2 cm and 4 cm for replica data sets and experimental data set, respectively, and for subfigures (c) and (g), radius of the pocket sizes are taken as 4 cm and 2 cm for replica data sets and experimental data set, respectively).

Figure 3.38, Figure 3.39, and Figure 3.40 show that the Linear Processor correctly identified the location of the water pocket in most cases. However, the right columns of the figures show that MVDR failed when we created a mismatch between the water pocket dimensions (see subfigures (f) and (g)). In Figure 3.38, Figure 3.39, and Figure 3.40, the subfigures (c) show the highest error in estimating the center of the water pocket. On the other hand, the figures also show that increasing the frequency of the excitation led to a decrease in the error when we located the water pocket with a 2 cm radius using replica data sets of a 4 cm water pocket.

The results of the Linear Processor are promising for the idea of using a water pocket when generating replica data sets. However, it is essential to examine its performance in different error situations because, in the actual case, the error will be observed not only in dimensions of the abnormal region but also in different parameters such as speed of sound or fat tissue thickness. The results of various case studies to understand the Linear Processor's error tolerance are presented in the following pages. The characteristics of the replica and experimental data sets used are shown in the tables below.

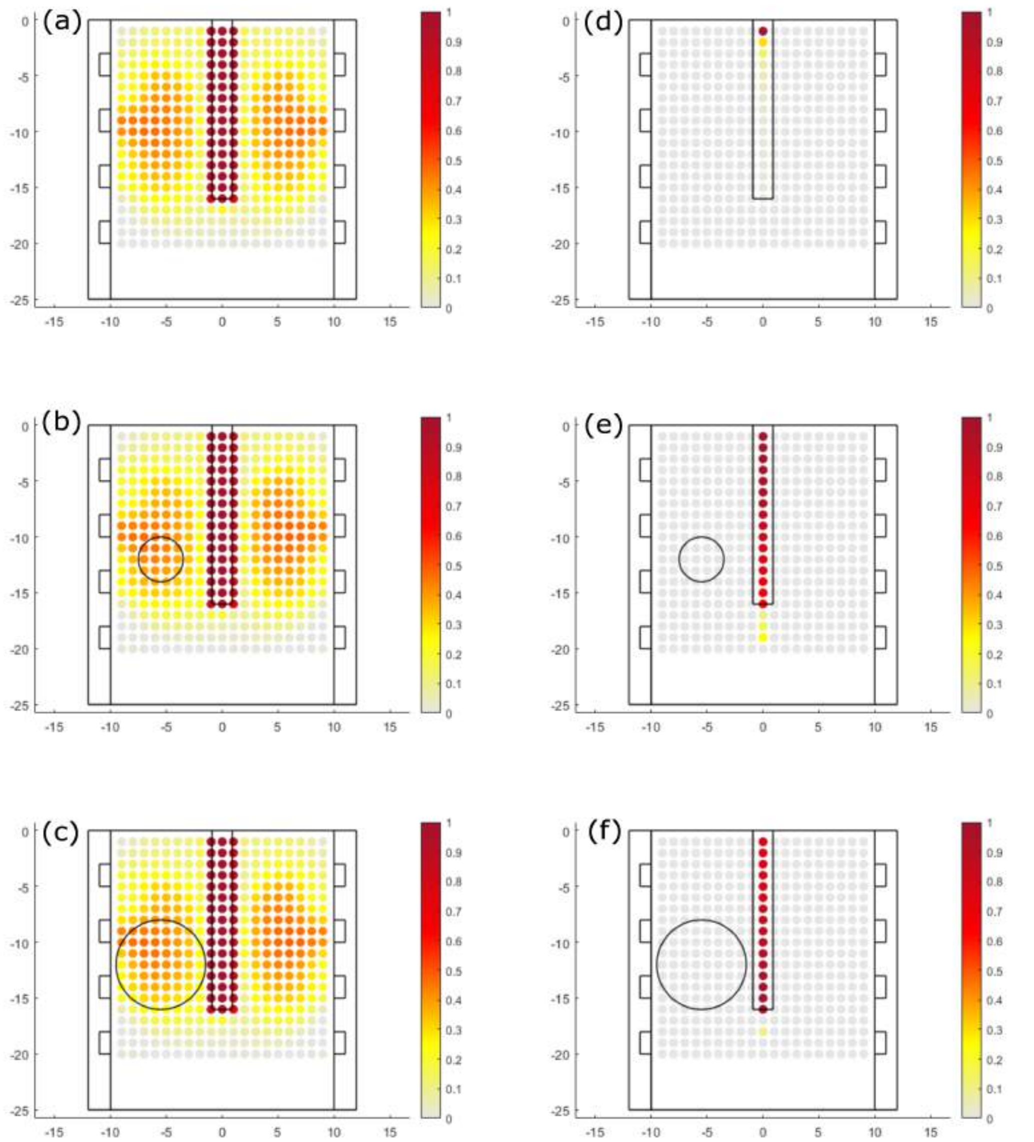

Figure 3.35: Results of Matched-Field Processors using monopole sources in replica data sets for 200 Hz. (a), (b), and (c) are obtained using the Linear Processor for healthy, 2 cm and 4 cm water pocket cases, respectively. (d), (e), and (f) are obtained using the MVDR for healthy, 2 cm, and 4 cm water pocket cases, respectively. Dimensions are given in cm.

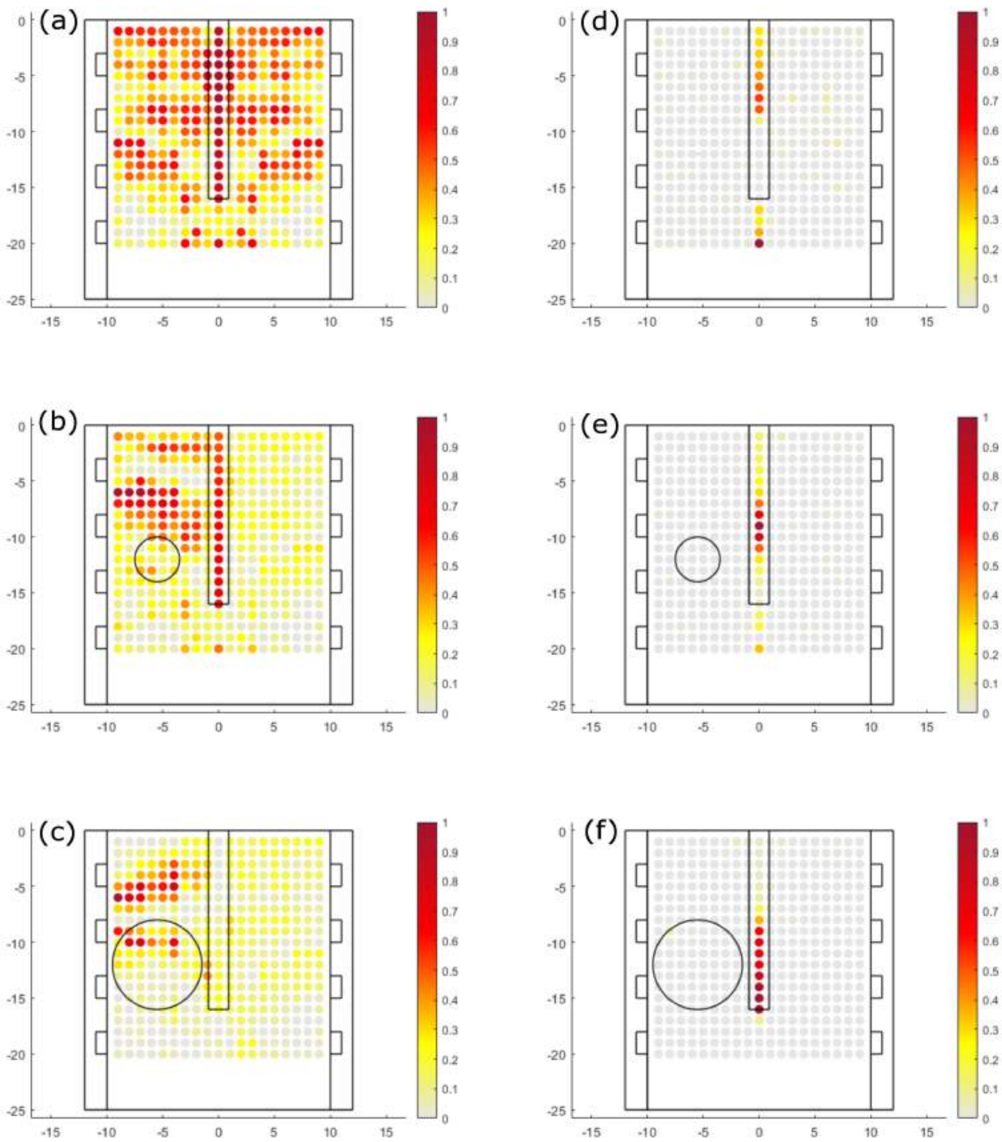

Figure 3.36: Results of Matched-Field Processors using monopole sources in replica data sets for 400 Hz. (a), (b), and (c) are obtained using the Linear Processor for healthy, 2 cm and 4 cm water pocket cases, respectively. (d), (e), and (f) are obtained using the MVDR for healthy, 2 cm, and 4 cm water pocket cases, respectively. Dimensions are given in cm.

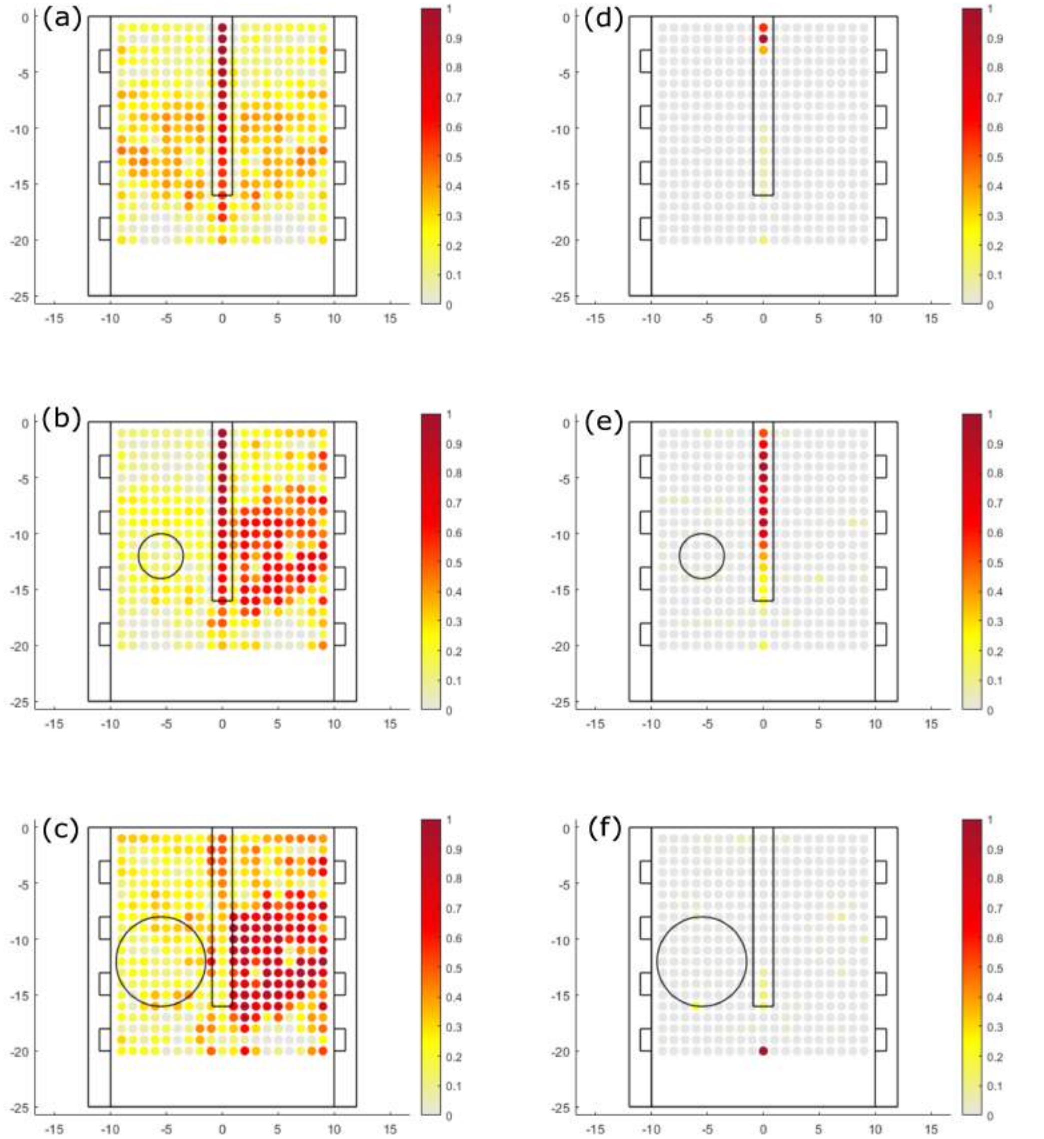

Figure 3.37: Results of Matched-Field Processors using monopole sources in replica data sets for 600 Hz. (a), (b), and (c) are obtained using the Linear Processor for healthy, 2 cm and 4 cm water pocket cases, respectively. (d), (e), and (f) are obtained using the MVDR for healthy, 2 cm, and 4 cm water pocket cases, respectively. Dimensions are given in cm.

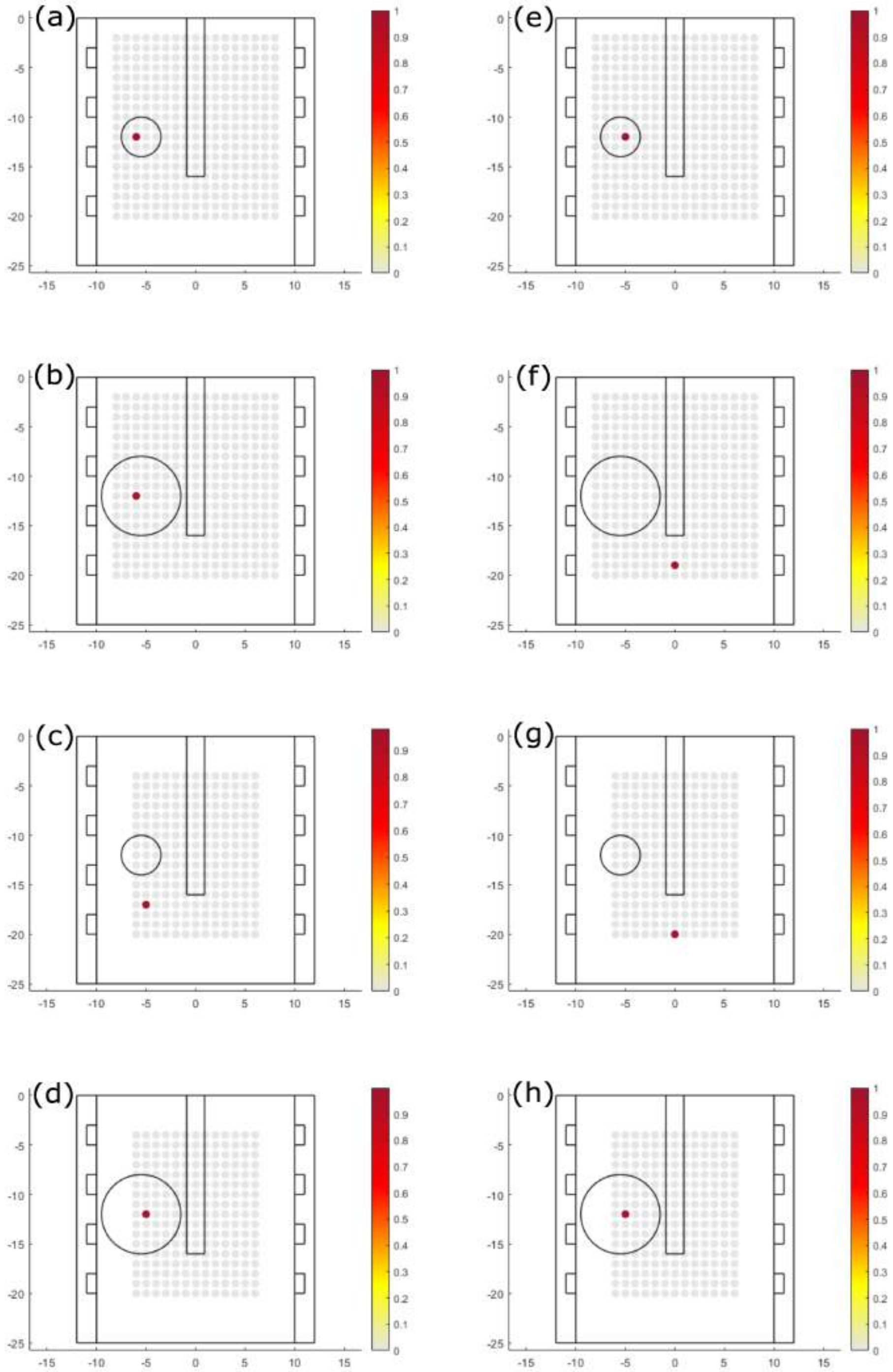

Figure 3.38: Results of Matched-Field Processors using water pockets in replica data sets for 200 Hz. (a), (b), (c), and (d) are obtained using the Linear Processor, (e), (f), (g), and (h) are obtained using the MVDR. Also, (a), (b), (e), and (d) present the results of 2 cm water pocket replica data sets, and (c), (d), (g), and (h) present the results of 4 cm water pocket replica data sets. Dimensions are given in cm.

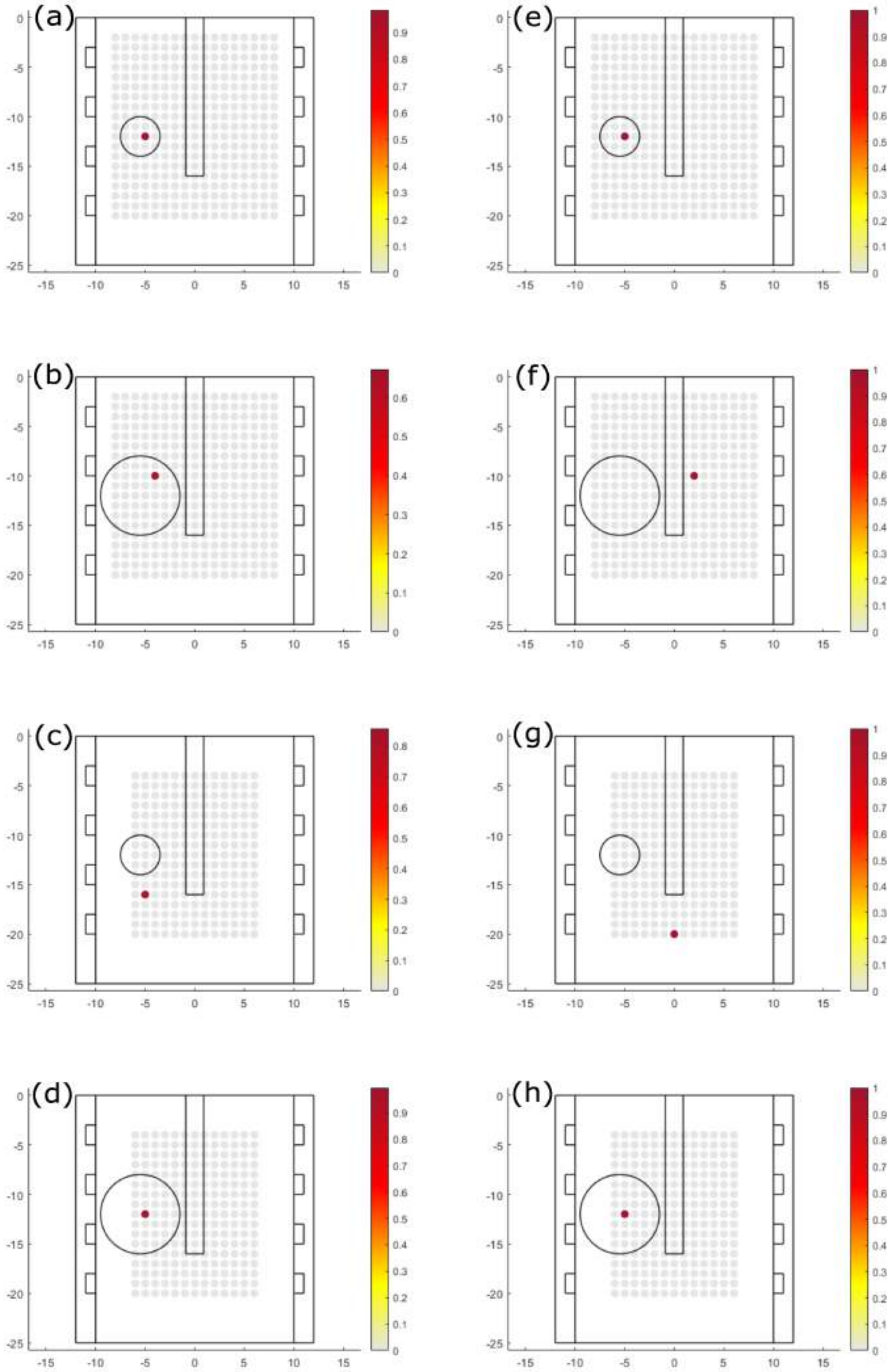

Figure 3.39: Results of Matched-Field Processors using water pockets in replica data sets for 400 Hz. (a), (b), (c), and (d) are obtained using the Linear Processor, (e), (f), (g), and (h) are obtained using the MVDR. Also, (a), (b), (e), and (d) present the results of 2 cm water pocket replica data sets, and (c), (d), (g), and (h) present the results of 4 cm water pocket replica data sets. Dimensions are given in cm.

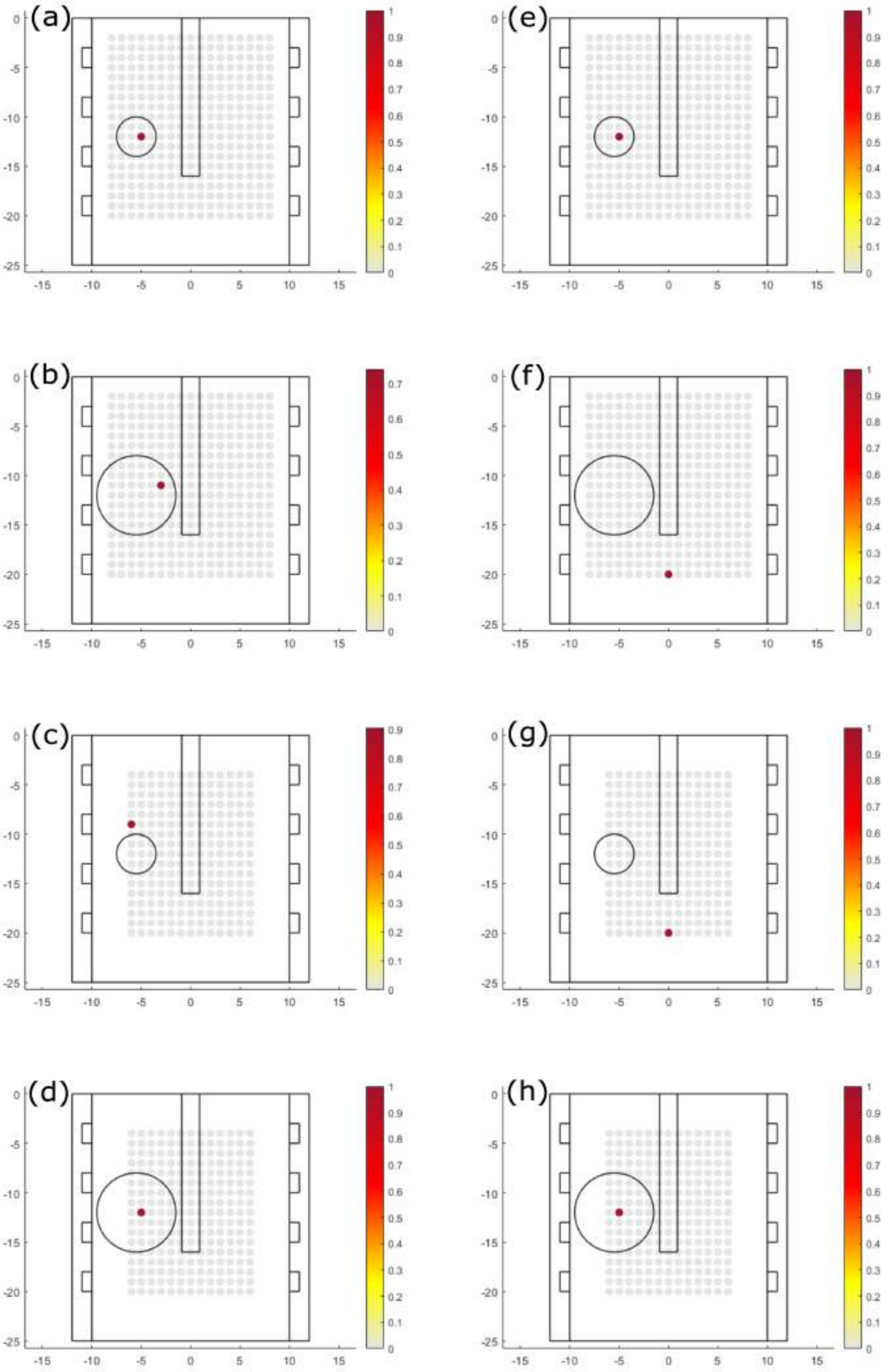

Figure 3.40: Results of Matched-Field Processors using water pockets in replica data sets for 600 Hz. (a), (b), (c), and (d) are obtained using the Linear Processor, (e), (f), (g), and (h) are obtained using the MVDR. Also, (a), (b), (e), and (d) present the results of 2 cm water pocket replica data sets, and (c), (d), (g), and (h) present the results of 4 cm water pocket replica data sets. Dimensions are given in cm.

For Case 1.1 and Case 1.2, we have employed a mismatch between replica and experimental data sets by changing the parenchyma's speed of sound, fat tissue thickness, and radius of the pocket. In terms of replica data sets, the only difference between Case 1.1 and Case 1.2 is the size of the water pockets. Figure 3.41 shows that for all cases except the 200 Hz results of Case 1.2 (subfigure (d)), we have obtained the center of the pocket with less than 1.5 cm error.

Table 3.3: Simulation parameters of Case 1.1

Replica Data Set		**Experimental Data Set**	
Speed of Sound	30 m/s	Speed of Sound	40 m/s
Fat Tissue Thickness	2 cm	Fat Tissue Thickness	3 cm
Attenuation	150 dB/m	Attenuation	150 dB/m
Radius of Pocket	2 cm	Radius of Pocket	3 cm
Material of Pocket	Water	Material of Pocket	Water

Table 3.4: Simulation parameters of Case 1.2

Replica Data Set		**Experimental Data Set**	
Speed of Sound	30 m/s	Speed of Sound	40 m/s
Fat Tissue Thickness	2 cm	Fat Tissue Thickness	3 cm
Attenuation	150 dB/m	Attenuation	150 dB/m
Radius of Pocket	4 cm	Radius of Pocket	3 cm
Material of Pocket	Water	Material of Pocket	Water

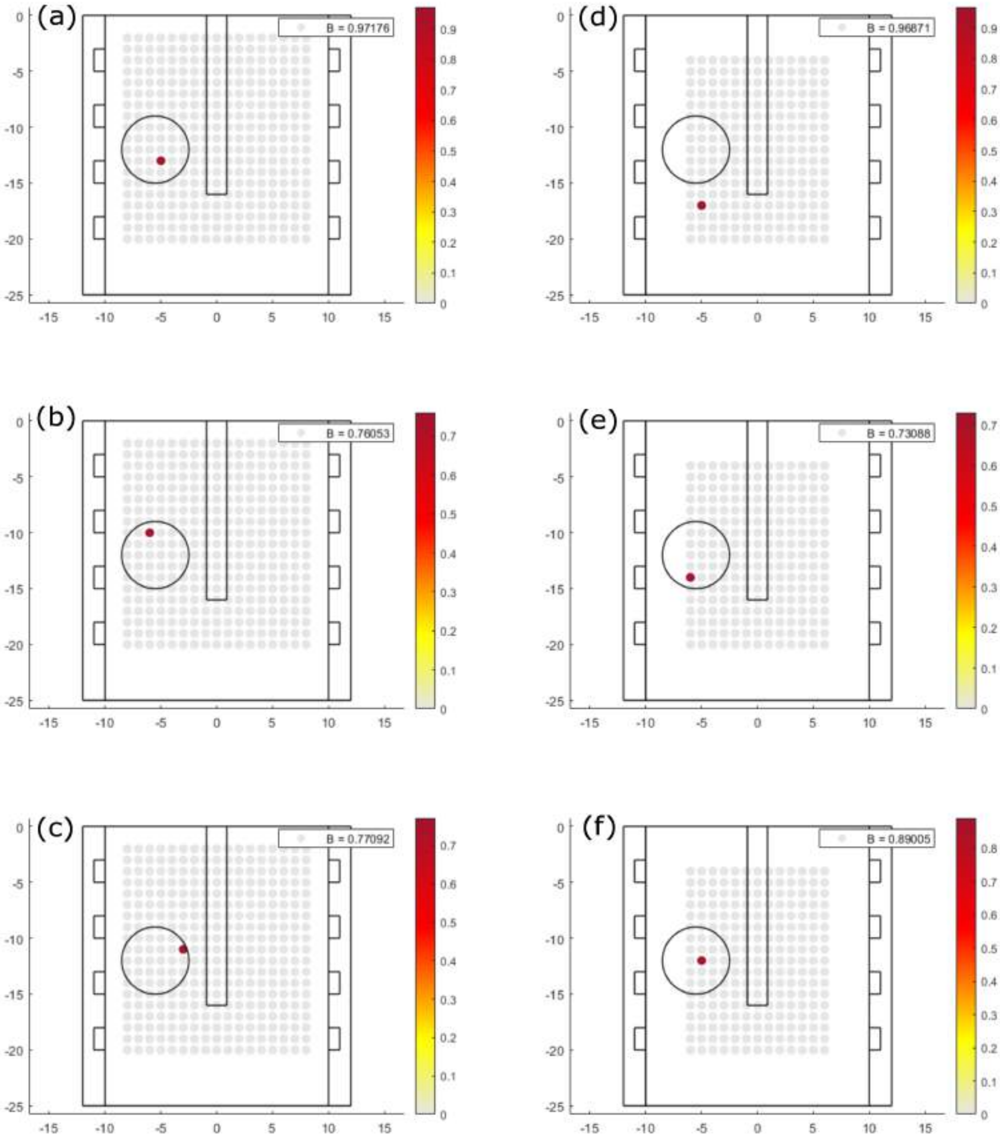

Figure 3.41: Results of Case 1.1 (left) for 200 Hz (a), 400 Hz (b), and 600 Hz (c) and results of Case 1.2 (right) for 200 Hz (d), 400 Hz (e), and 600 Hz (f). Dimensions are given in cm.

For Case 1.3 and Case 1.4, we have employed a mismatch between replica and experimental data sets by changing the fat tissue thickness, radius of the pocket, and parenchyma's speed of sound and attenuation. In terms of replica data sets, the only difference between Case 1.3 and Case 1.4 is the size of the water pockets. Figure 3.42 shows that for all cases except the 200 Hz results of Case 1.3 (subfigure (d)), we have obtained the center of the pocket with less than 1.5 cm error.

Table 3.5: Simulation parameters of Case 1.3

Replica Data Set		**Experimental Data Set**	
Speed of Sound	30 m/s	Speed of Sound	40 m/s
Fat Tissue Thickness	2 cm	Fat Tissue Thickness	3 cm
Attenuation	150 dB/m	Attenuation	120 dB/m
Radius of the Pocket	2 cm	Radius of the Pocket	3 cm
Material of the Pocket	Water	Material of the Pocket	Water

Table 3.6: Simulation parameters of Case 1.4

Replica Data Set		**Experimental Data Set**	
Speed of Sound	30 m/s	Speed of Sound	40 m/s
Fat Tissue Thickness	2 cm	Fat Tissue Thickness	3 cm
Attenuation	150 dB/m	Attenuation	120 dB/m
Radius of the Pocket	4 cm	Radius of the Pocket	3 cm
Material of the Pocket	Water	Material of the Pocket	Water

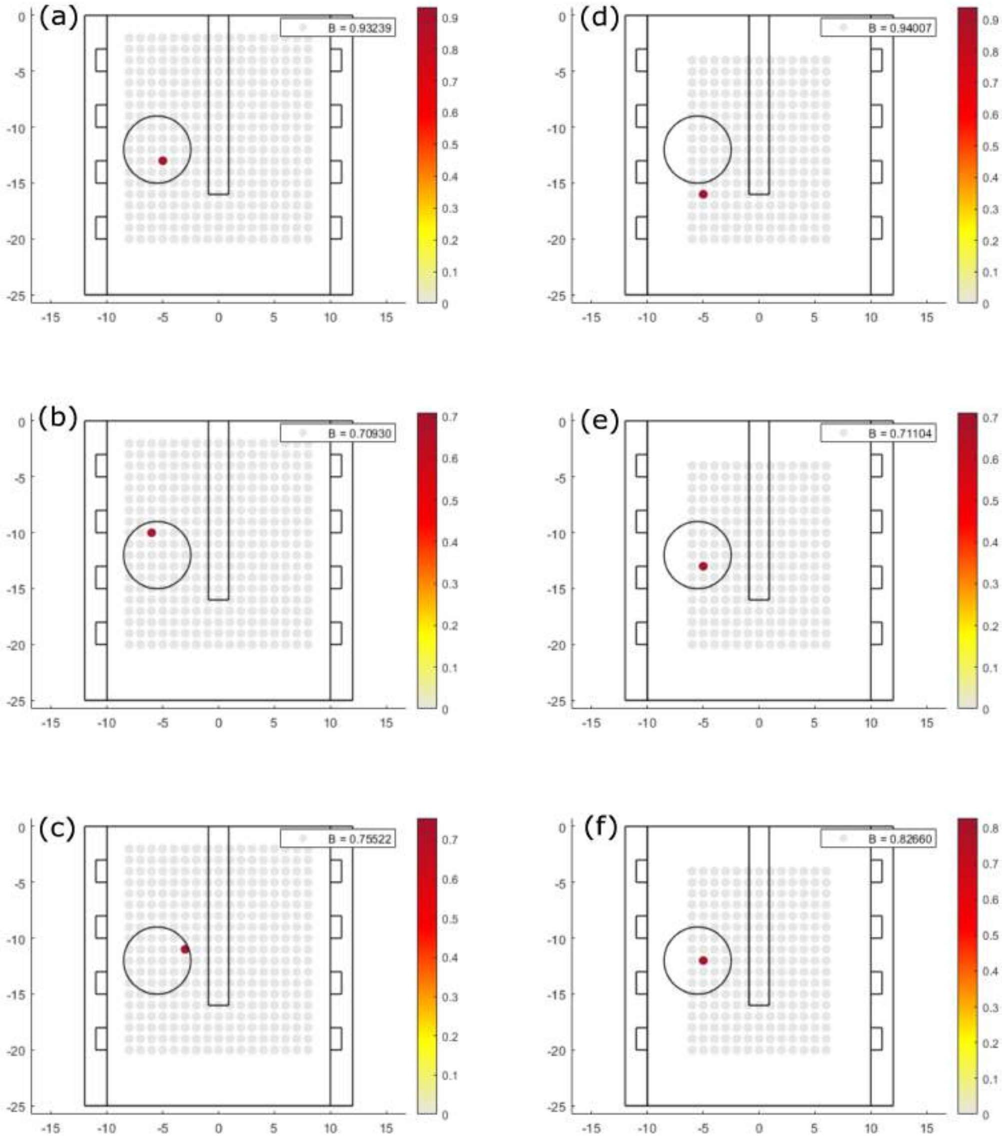

Figure 3.42: Results of Case 1.3 (left) for 200 Hz (a), 400 Hz (b), and 600 Hz (c) and results of Case 1.4 (right) for 200 Hz (d), 400 Hz (e), and 600 Hz (f). Dimensions are given in cm.

For Case 1.5 and Case 1.6, we have employed a mismatch between replica and experimental data sets by changing the fat tissue thickness, radius of the pocket, and parenchyma's speed of sound and attenuation. In addition to these changes, we have also used the air pocket instead of the water pocket. In terms of replica data sets, the only difference between Case 1.5 and Case 1.6 is the size of the water pockets. Figure 3.43 shows that for all cases except the 200 Hz results of Case 1.5 and 1.6 (subfigures (a) and (d)), we have obtained the center of the air pocket with less than 2 cm error.

Table 3.7: Simulation parameters of Case 1.5

Replica Data Set		**Experimental Data Set**	
Speed of Sound	30 m/s	Speed of Sound	40 m/s
Fat Tissue Thickness	2 cm	Fat Tissue Thickness	3 cm
Attenuation	150 dB/m	Attenuation	120 dB/m
Radius of the Pocket	2 cm	Radius of the Pocket	3 cm
Material of the Pocket	Water	Material of the Pocket	Air

Table 3.8: Simulation parameters of Case 1.6

Replica Data Set		**Experimental Data Set**	
Speed of Sound	30 m/s	Speed of Sound	40 m/s
Fat Tissue Thickness	2 cm	Fat Tissue Thickness	3 cm
Attenuation	150 dB/m	Attenuation	120 dB/m
Radius of Pocket	4 cm	Radius of Pocket	3 cm
Material of Pocket	Water	Material of Pocket	Air

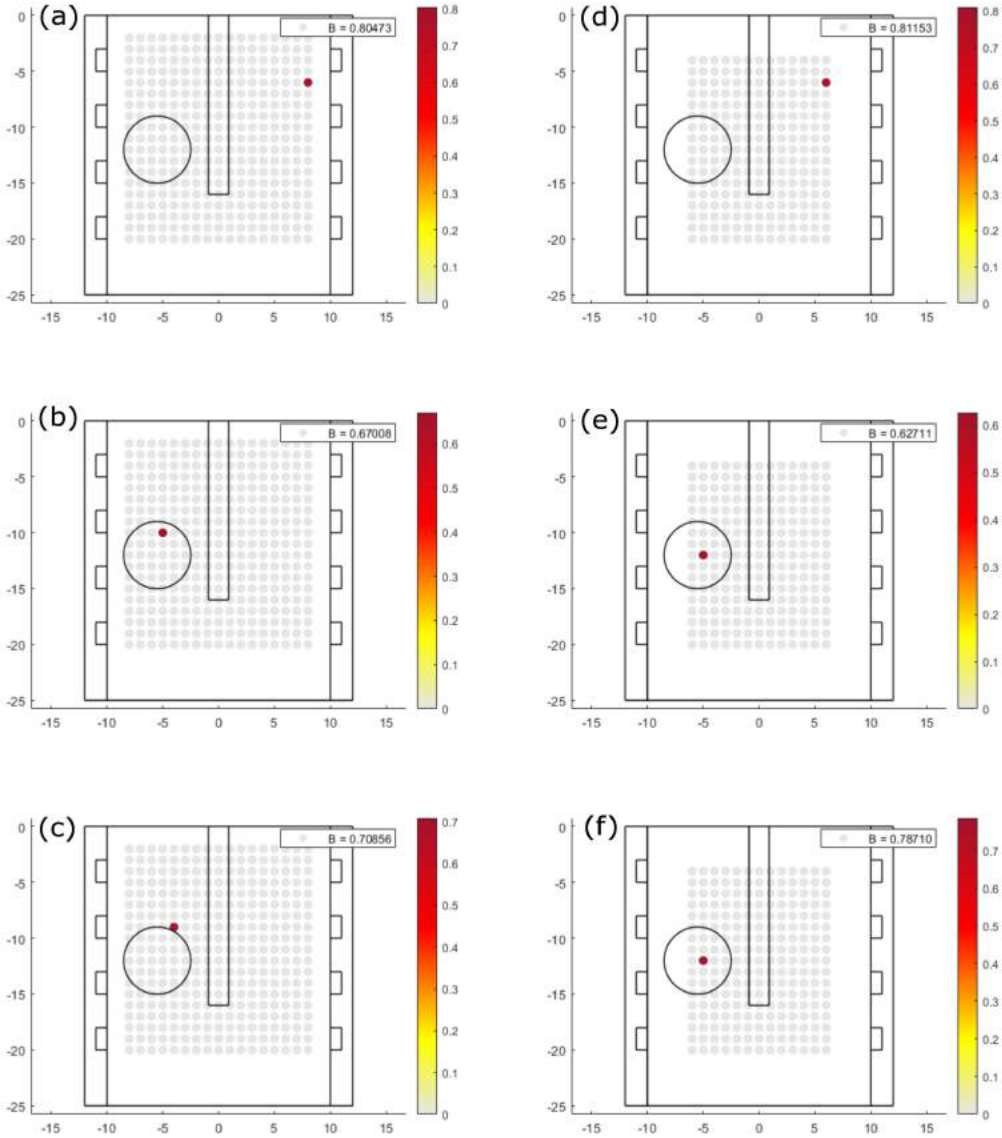

Figure 3.43: Results of Case 1.5 (left) for 200 Hz (a), 400 Hz (b), and 600 Hz (c) and results of Case 1.6 (right) for 200 Hz (d), 400 Hz (e), and 600 Hz (f). Dimensions are given in cm.

3.3.5 Concluding Remarks on 2D Model

Time domain analysis of the model (see Section 3.3.1) showed that the water pocket, especially for large pockets and relatively high frequencies, created a significant phase difference in the time arrivals of the signals. Another important thing was observed at the first signals reached the microphone, which had the closest location to the abnormality. This can be explained by the fact that the speed of sound of the abnormal region is much higher than the parenchymal tissue.

Section 3.3.2 showed that when we processed the signal with 0.1 seconds length using a Conventional Beamformer, an abnormal region appeared as a sound source in some cases, but not in all cases. The reason for this can be explained as the geometry is complex, so the sound propagation develops differently for each case. Another important remark is that Formulation I and Formulation IV presented inspectable acoustic fields while Formulation II and Formulation III gave only source strength, not a proper acoustic field. Also, when we process the signal that is almost equal to the two times of the excitation period, Formulation IV demonstrated the location of the abnormal region as the sound source for almost every case.

Frequency domain analysis of the model (see Section 3.3.4) showed that the water pocket acts as a sound barrier, especially for large pockets and high frequencies. In most of the results, the water pocket did not emerge as a region with high sound intensity.

In the following section (see Section 3.3.5), the results of two different Paired Field Processors are presented to question the assumption that we can express the water pocket with multiple monopole sound sources. Section 3.3.5 showed that this is not a valid assumption in every situation. Results also showed that the results of the Linear Processor were more meaningful than those of the MVDR. In the following part of the section, instead of expressing the abnormal region as multiple monopole sources, we sought an answer to the question of whether we can model it directly. Since we only have the numerical model, we measured the processor's performance by creating errors on the model parameters. The results showed that this region could be localized in 2D model despite the high error.

3.4 Acoustic Imaging Results for the 3D Configuration

In this section, results of the Conventional Beamformer and the Linear Processor for the 3D configuration are presented.

3.4.1 Results of the Conventional Beamformer

Figure 3.44, Figure 3.45, and Figure 3.46 show the acoustic fields obtained through the Conventional Beamformer by processing the signals received at 400 Hz over the 3D configuration for different pocket sizes. Formulation IV was used to create steering vectors. The main idea behind the 3D implementation of the Convention Beamformer was to generate cross-sectional images of the body on the z-axis. We have obtained 2D acoustic fields by "slicing" the model every 1 cm height. We have used two different configuration in terms of the location of the pocket.

Figure 3.44 shows that a water pocket (z=-6 cm) with a radius of 2 cm did not appear in the field as a source. On the other hand, Figure 3.45 and Figure 3.46 show that the beamformer provided an approximate location of the pockets when signals obtained for the water pockets with radii of 3 cm and 4 cm were processed. Figures do not show the exact position of the abnormal region. However, It can help us to narrow the region of interest. In acoustic images, no significant difference has been observed between 3 cm and 4 cm water pocket cases. Although we neglected the source strength, Figure 3.45 and Figure 3.46 show that increasing the pocket size decreased the maximum amplitude.

Figure 3.47, Figure 3.48, and Figure 3.49 show the acoustic fields obtained through the Conventional Beamformer for different pocket sizes (z=-10 cm). Acoustic fields obtained for z=-11 and z=-12 cm of Figure 3.47 show that a 2 cm radius water pocket affected the response significantly. However, the results were inaccurate in locating the abnormal region. Figure 3.48 and Figure 3.49 show that water pockets with 3 cm and 4 cm radii might be identified using the Conventional Beamformer. It can be seen from Figure 3.48 and Figure 3.49 that increasing pocket size created a broader region. This information can be used to determine the pocket size.

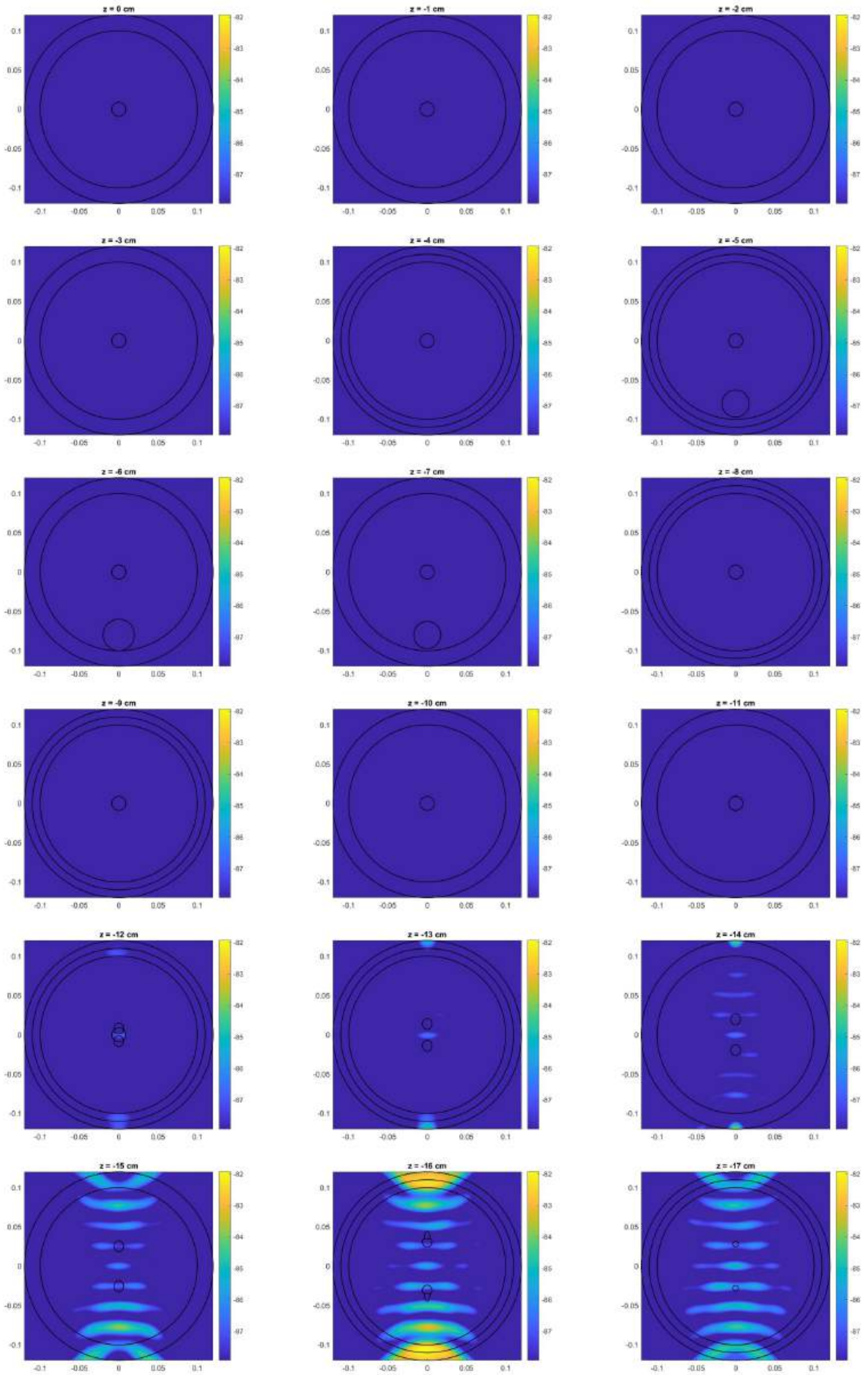

Figure 3.44: Acoustic fields (SPL [dB]) obtained by processing signals of 0.003 seconds length at 400 Hz through the Conventional Beamformer with Formulation IV for the 3D configuration. Radius of the pocket is 2 cm. Dimensions are given in m.

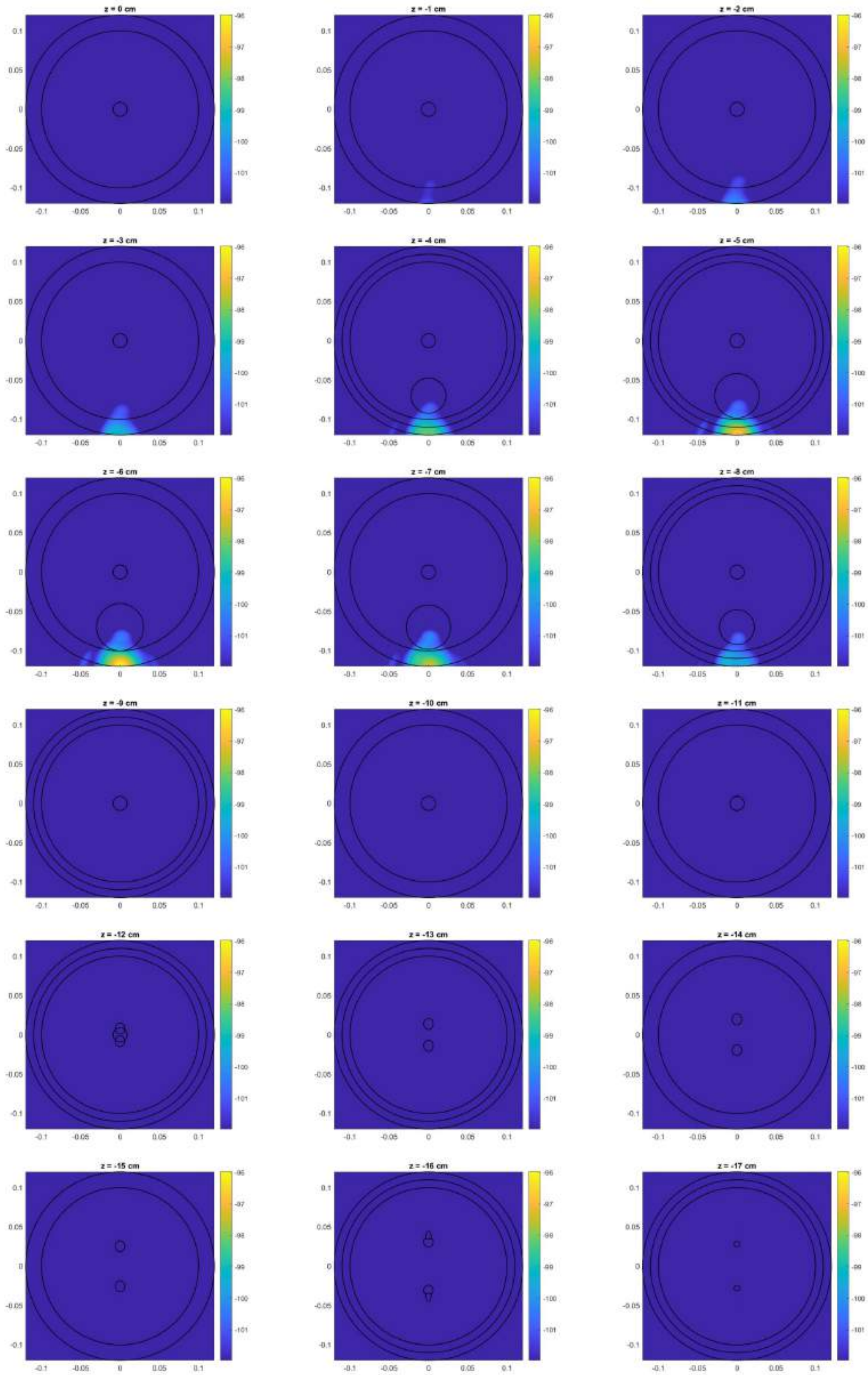

Figure 3.45: Acoustic fields (SPL [dB]) obtained by processing signals of 0.003 seconds length at 400 Hz through the Conventional Beamformer with Formulation IV for the 3D configuration. Radius of the pocket is 3 cm. Dimensions are given in m.

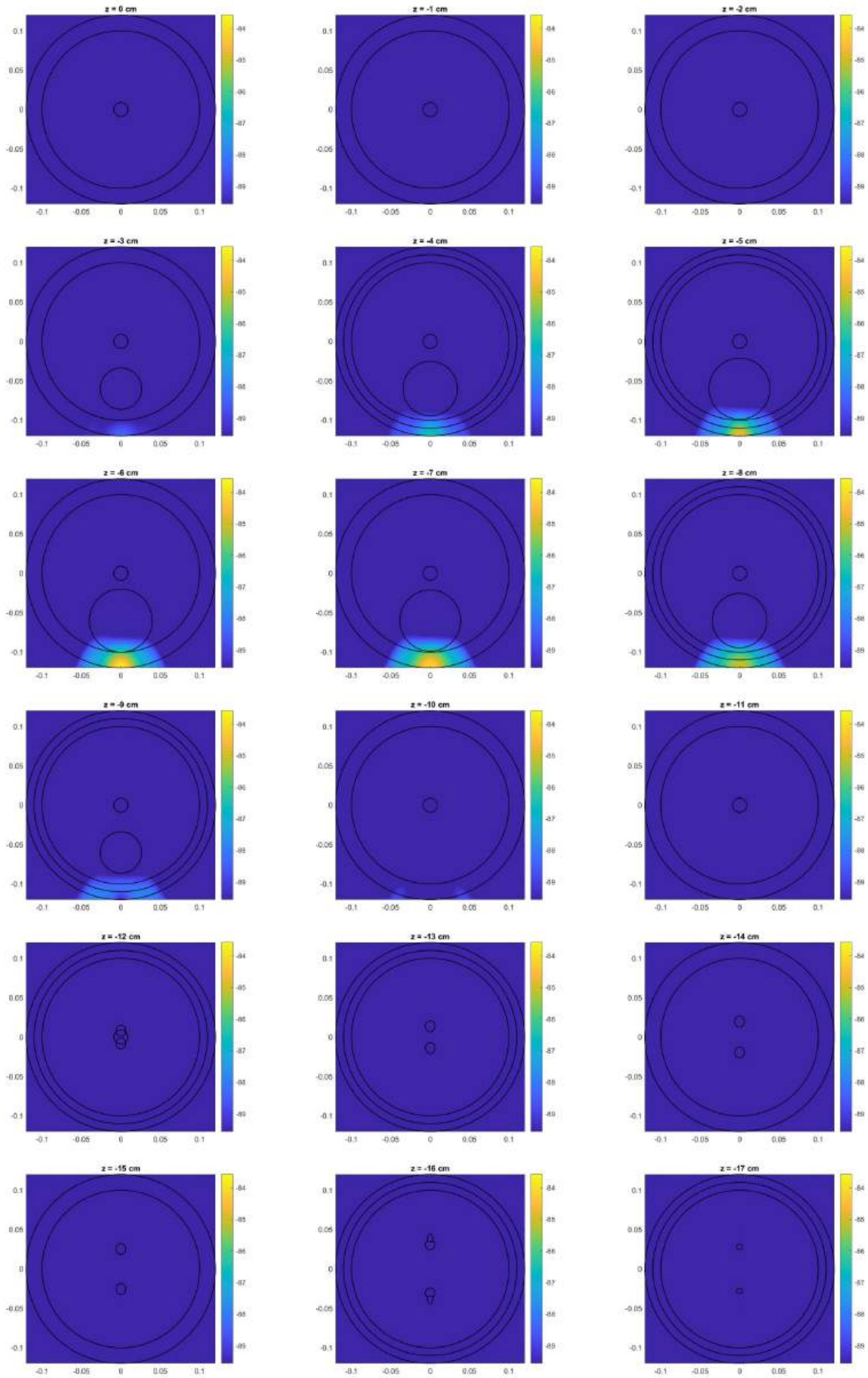

Figure 3.46: Acoustic fields (SPL [dB]) obtained by processing signals of 0.003 seconds length at 400 Hz through Conventional Beamformer with Formulation IV for the 3D configuration. Radius of the pocket is 4 cm. Dimensions are given in m.

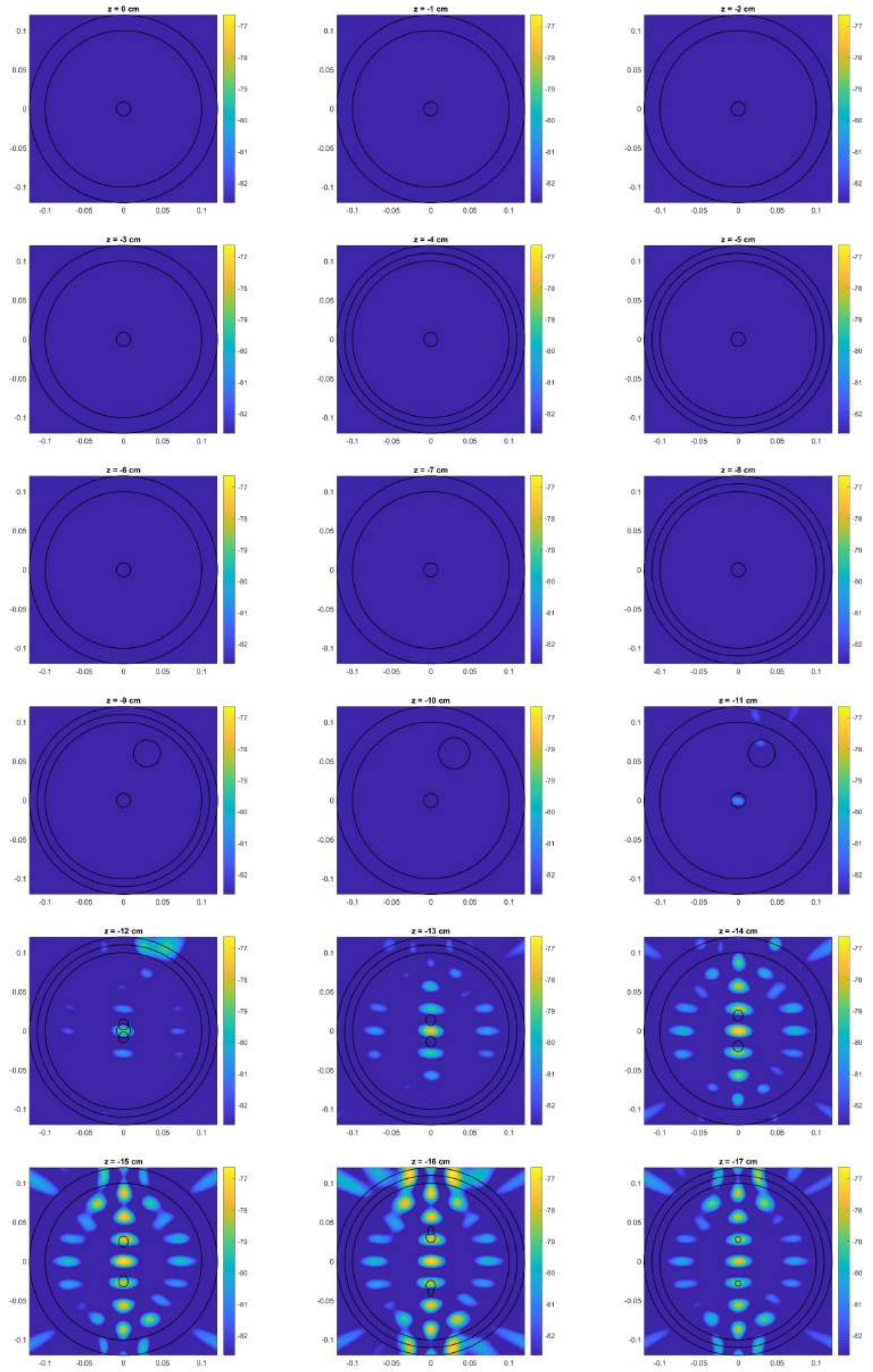

Figure 3.47: Acoustic fields (SPL [dB]) obtained by processing signals of 0.003 seconds length at 600 Hz through the Conventional Beamformer with Formulation IV for the 3D configuration. Radius of the pocket is 2 cm. Dimensions are given in m.

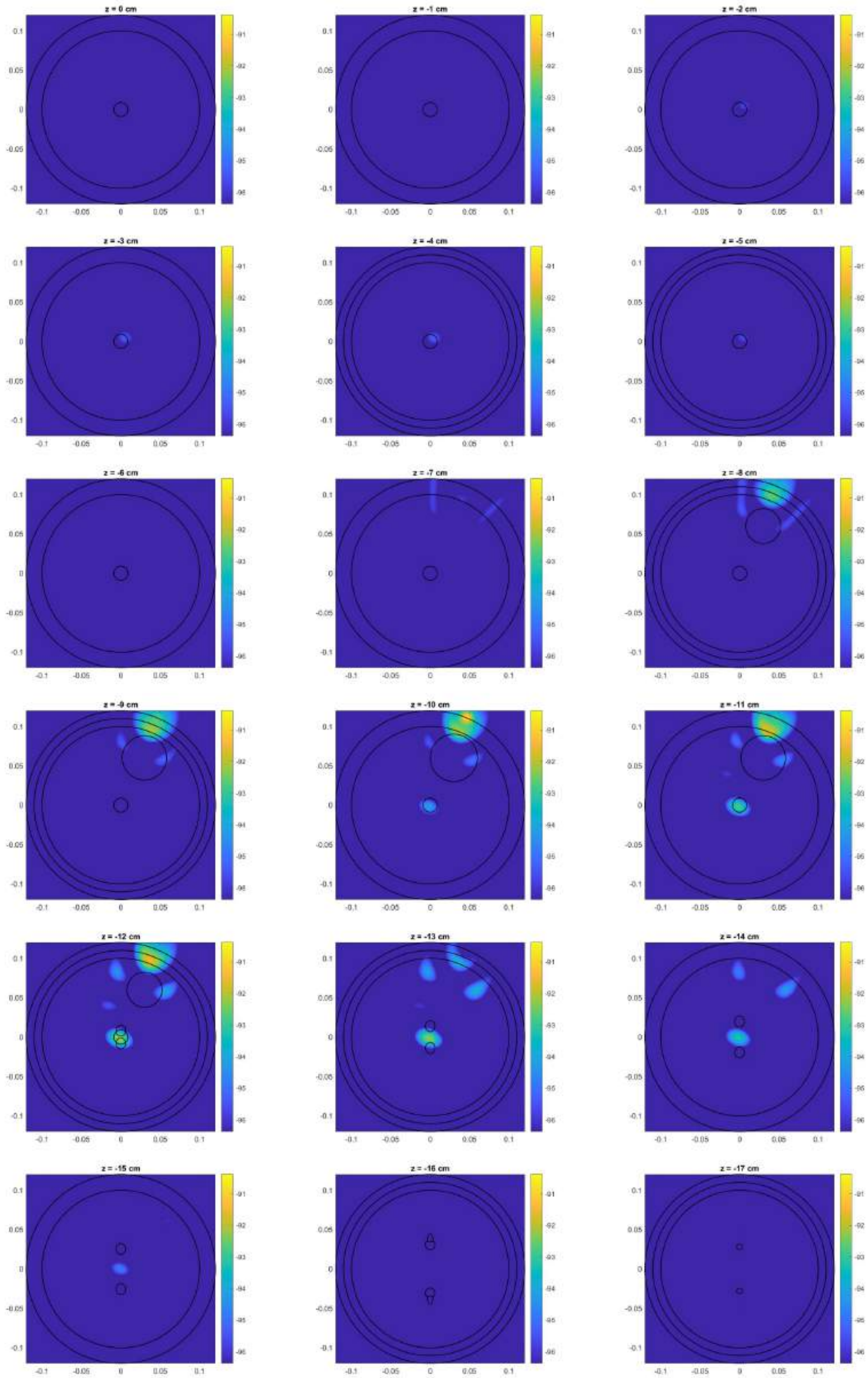

Figure 3.48: Acoustic fields (SPL [dB]) obtained by processing signals of 0.003 seconds length at 600 Hz through the Conventional Beamformer with Formulation IV for the 3D configuration. Radius of the pocket is 3 cm. Dimensions are given in m.

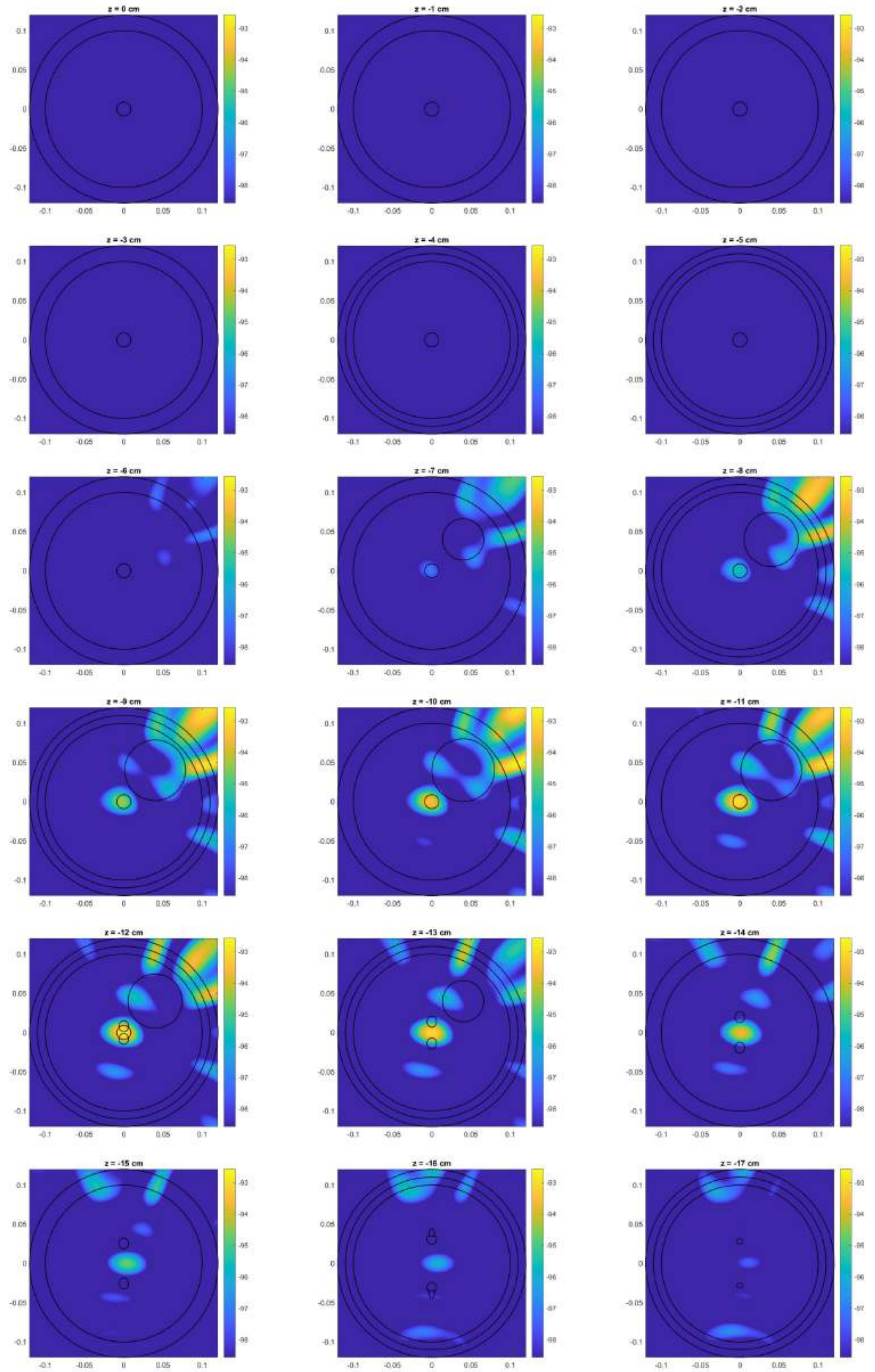

Figure 3.49: Acoustic fields (SPL [dB]) obtained by processing signals of 0.003 seconds length at 600 Hz through the Conventional Beamformer with Formulation IV for the 3D configuration. Radius of the pocket is 4 cm. Dimensions are given in m.

3.4.2 Results of the Linear Processor

In this section, we present the results obtained through the Linear Processor. Frequency domain analysis has been conducted for 400 and 600 Hz to obtain replica and experimental data sets. For each frequency, The Linear Processor has been employed for eight separate cases, and error in each case has been investigated. A single simulation parameter has been changed while others have been kept constant for each case. Simulation parameters of cases have shown in the following tables.

Table 3.9, Table 3.10, Table 3.11, and Table 3.12 show the simulation parameters applied to obtain replica and experimental data sets. Figure 3.50 shows the grid points used to generate replica data sets. Since Conventional Beamformer results obtained for 400 Hz (Figure 3.45 and Figure 3.46) have presented the approximate location of the water pocket, grid points were not created for the whole volume.

For all cases, the location of the experimental water pockets was determined at a point that is not a grid point of the replica data sets. In other words, we always have a mismatch between the location of the water pockets used for replica and experimental data sets for all cases. Also, for each case, we have employed a mismatch in the radius of the pockets.

For Case 2.1, none of the simulation parameters has been changed. Figure 3.51 shows that in both situations, we have obtained the pocket place with a 1.33 cm error. Also, the output of the processor was almost equal to one, which is the maximum case which shows that obtained velocity response was almost the same for both Case 2.1A and Case 2.1B.

In Case 2.2, besides the mismatch in the location and radius of the pockets, we have also increased the fat tissue thickness to create a different mismatch. Figure 3.52 shows that we have localized the water pocket almost at the opposite side of the domain for both cases. This might be due to the insufficient number of mesh since there was no such difference observed in the results of the 2D cases.

In Case 2.3; we have increased the speed of sound of the lung from 30 m/s to 40 m/s. Figure 3.53 shows that even if the output of the processor was low, we obtained the water pocket's location with a 2 cm error. Sound attenuation of the lung has been changed to create a mismatch in Case 2.4, and Figure 3.54 shows that the attenuation mismatch did not significantly affect the output of the processor and the localization of the water pocket when we compared with the first case.

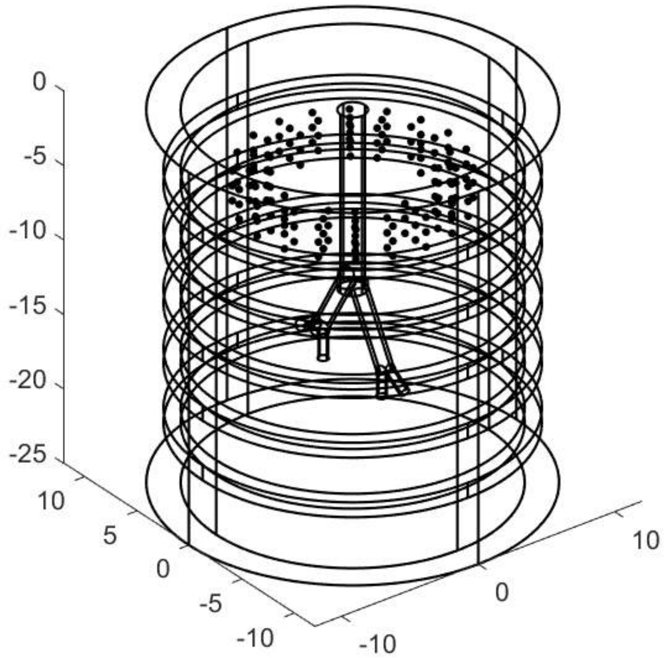

Figure 3.50: Grid points used to generate replica data sets for 400 Hz. Dimensions are given in cm.

Table 3.9: Simulation Parameters of Case 2.1 for 400 Hz

	Replica data set	**Case 2.1A**	**Case 2.1B**
Speed of sound	30 m/s	30 m/s	30 m/s
Fat tissue thickness	2 cm	2 cm	2 cm
Attenuation	150 dB/m	150 dB/m	150 dB/m
Radius of pocket	3 cm	2 cm	4 cm

Table 3.10: Simulation Parameters of Case 2.2 for 400 Hz

	Replica data set	**Case 2.2A**	**Case 2.2B**
Speed of sound	30 m/s	30 m/s	30 m/s
Fat tissue thickness	2 cm	3 cm	3 cm
Attenuation	150 dB/m	150 dB/m	150 dB/m
Radius of pocket	3 cm	2 cm	4 cm

Table 3.11: Simulation Parameters of Case 2.3 for 400 Hz

	Replica data set	**Case 2.3A**	**Case 2.3B**
Speed of sound	30 m/s	40 m/s	40 m/s
Fat tissue thickness	2 cm	2 cm	2 cm
Attenuation	150 dB/m	150 dB/m	150 dB/m
Radius of pocket	3 cm	2 cm	4 cm

Table 3.12: Simulation Parameters of Case 2.4 for 400 Hz

	Replica data set	**Case 2.4A**	**Case 2.4B**
Speed of sound	30 m/s	30 m/s	30 m/s
Fat tissue thickness	2 cm	2 cm	2 cm
Attenuation	150 dB/m	170 dB/m	170 dB/m
Radius of pocket	3 cm	2 cm	4 cm

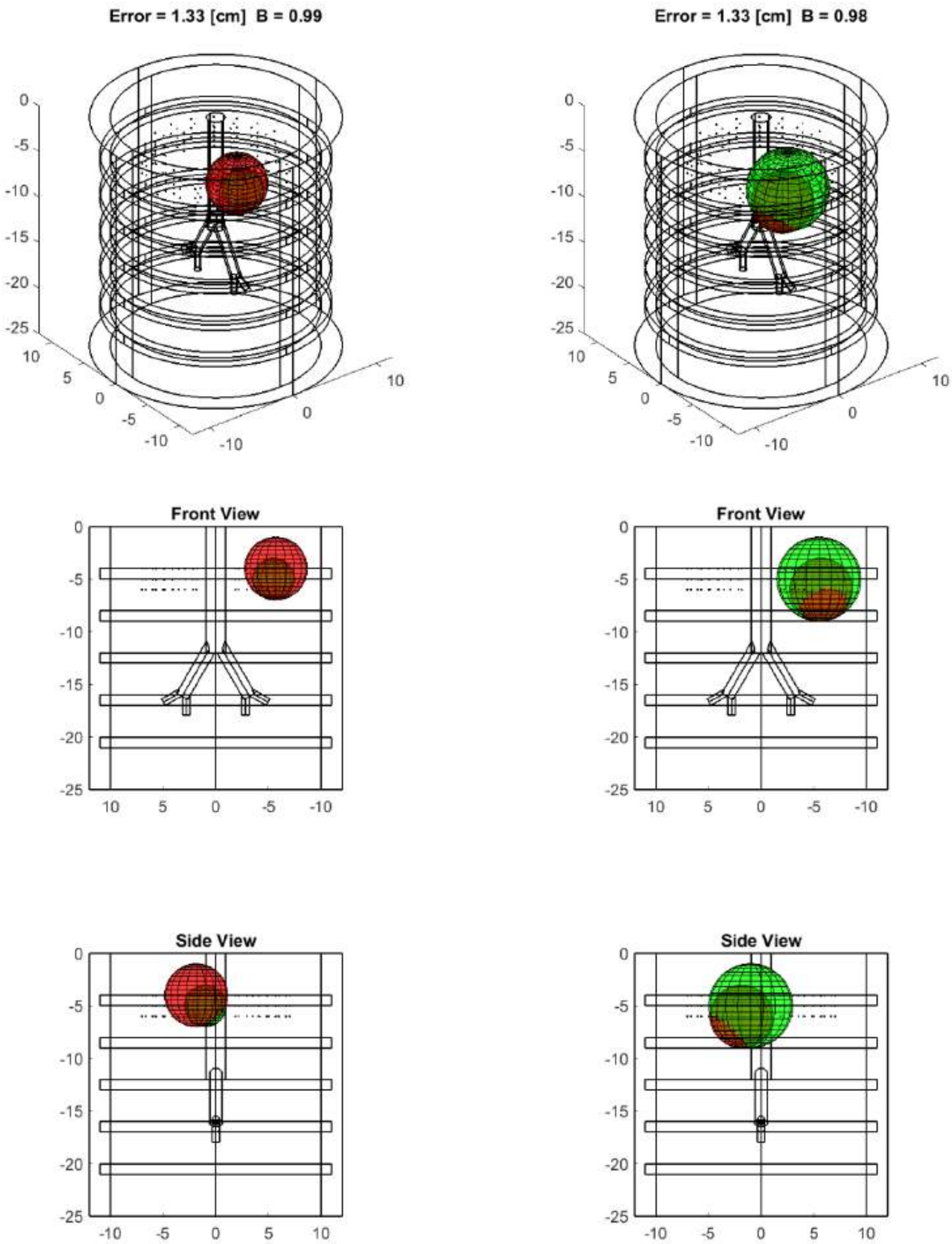

Figure 3.51: Results of the Linear Processor for Case 2.1A (left column) and Case 2.1B (right column) (red sphere represents the predicted pocket, green sphere represents the actual pocket, **Error** is the distance between the centers of the spheres, and **B** is the output of the processor). Dimensions are given in cm. Excitation frequency is 400 Hz.

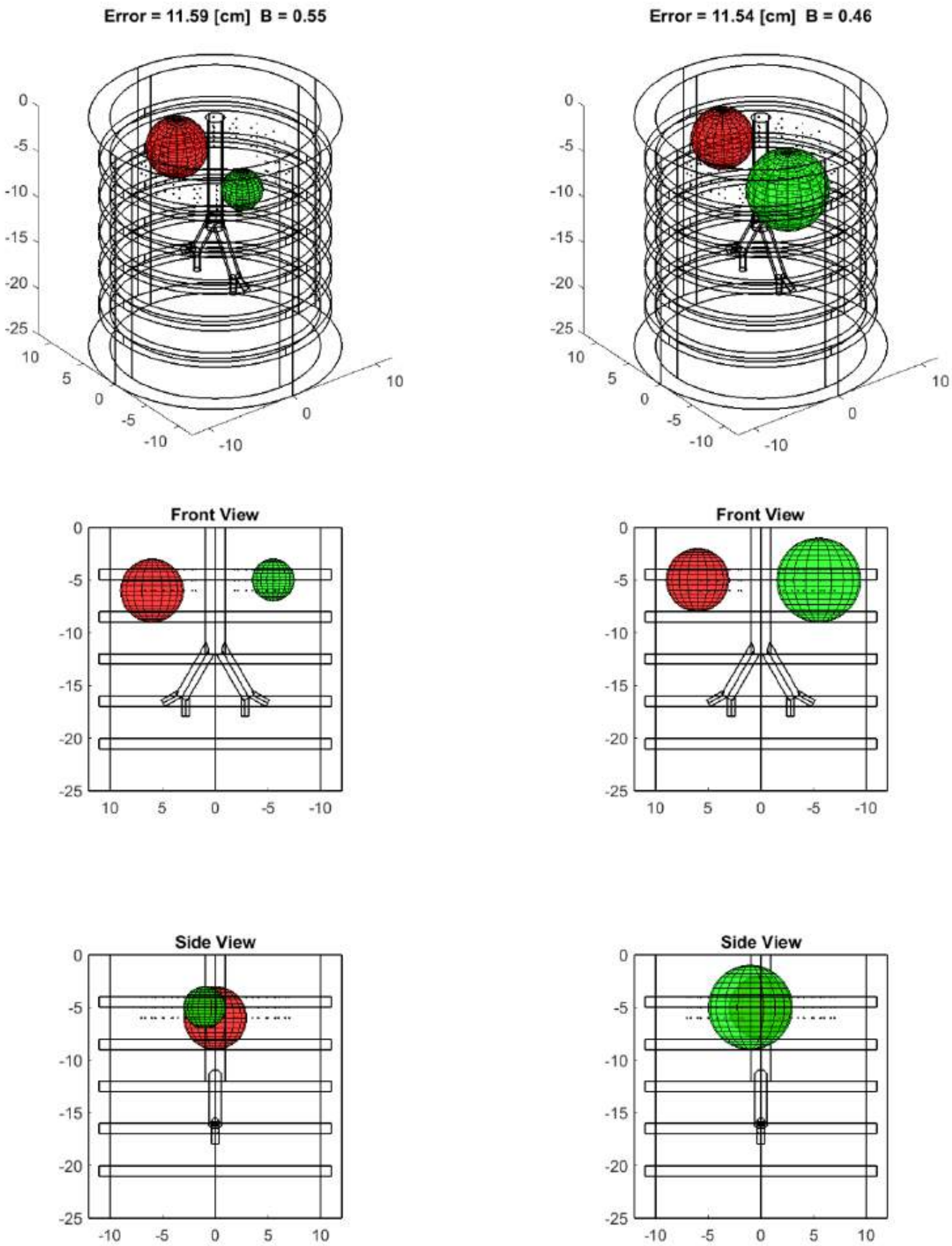

Figure 3.52: Results of the Linear Processor for Case 2.2A (left column) and Case 2.2B (right column) (red sphere represents the predicted pocket, green sphere represents the actual pocket, **Error** is the distance between the centers of the spheres, and **B** is the output of the processor). Dimensions are given in cm. Excitation frequency is 400 Hz.

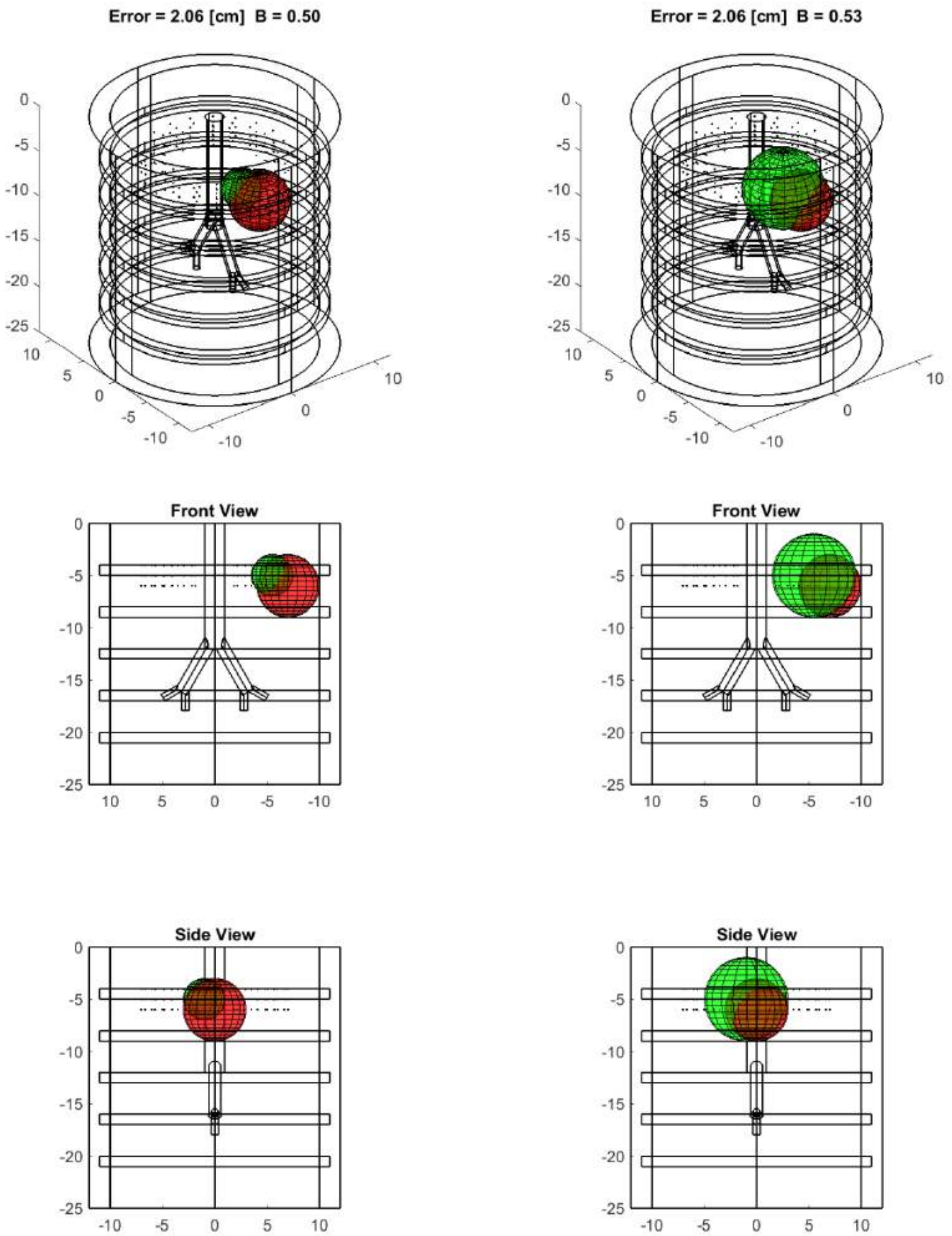

Figure 3.53: Results of the Linear Processor for Case 2.3A (left column) and Case 2.3B (right column) (red sphere represents the predicted pocket, green sphere represents the actual pocket, $\mathbf{Error}$ is the distance between the centers of the spheres, and $\mathbf{B}$ is the output of the processor). Dimensions are given in cm. Excitation frequency is 400 Hz.

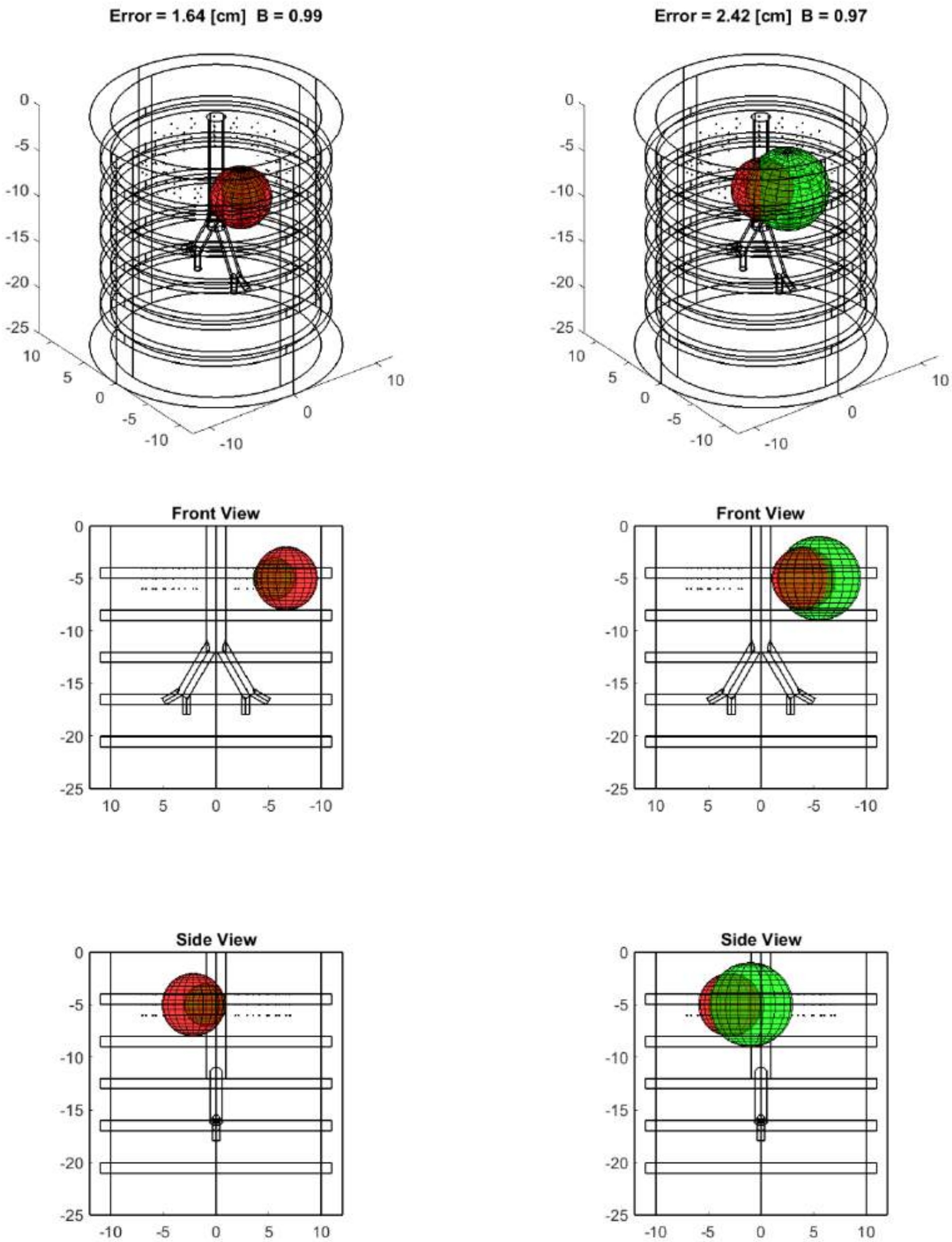

Figure 3.54: Results of the Linear Processor for Case 2.4A (left column) and Case 2.4B (right column) (red sphere represents the predicted pocket, green sphere represents the actual pocket, **Error** is the distance between the centers of the spheres, and **B** is the output of the processor). Dimensions are given in cm. Excitation frequency is 400 Hz.

Figure 3.48 and Figure 3.49 show the approximate locations of the water pocket for 600 Hz, so we have followed the same approach by creating the grid points in the specified region, which are shown in Figure 3.55. Table 3.13, Table 3.14, Table 3.15, and Table 3.16 show the simulation parameters applied to obtain replica and experimental data sets. We have employed mismatches in the location and in the radius of the pocket for all cases, like in the previous section. The only radius of the replica data set has been changed since Conventional Beamformer results show that increasing the frequency makes it easier and possible to localize the smaller pockets.

Figure 3.56 shows that we have obtained the pocket place with a 1.33 cm error for Case 3.1B. The result of Case 3.1A presented higher error when we compared it with Case 3.1B. However, it also gave a very high correlation. This can be explained by the fact that pockets with 1 cm and 2 cm radii did not significantly affect the obtained response. In other words, their influences on the responses were similar.

Figure 3.57 and Figure 3.58 show that the highest errors and lowest correlations have been obtained for Case 3.2 and Case 3.3. When we compared these results with the results of the 400 Hz study (see Figure 3.52 and Figure 3.53), it was seen that mismatches between fat tissue thicknesses and speed of sound affect the output of the processor more negatively.

Figure 3.59 shows similar results to the previous section for Case 3.4B: The mismatch in the sound attenuation did not affect the results remarkably. The obtained error and the processor output were the same as in Case 1B. However, for Case 3.4A, where we used the water pocket with a 1 cm radius for the experimental data set, an obtained error has been decreased compared to Case 3.1A. Also, it was observed that the correlation between data sets had increased.

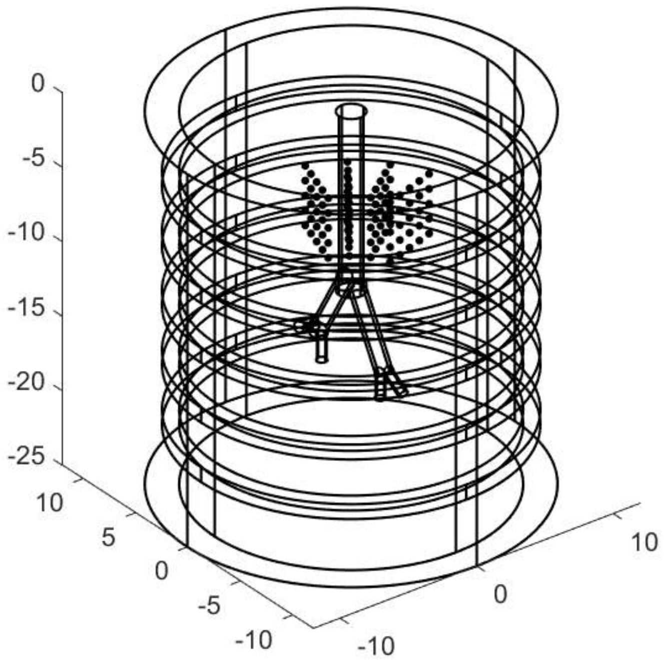

Figure 3.55: Grid points used to generate replica data sets for 600 Hz. Dimensions are given in cm.

Table 3.13: Simulation Parameters of Case 3.1 for 600 Hz

	Replica data set	**Case 3.1A**	**Case 3.1B**
Speed of sound	30 m/s	30 m/s	30 m/s
Fat tissue thickness	2 cm	2 cm	2 cm
Attenuation	150 dB/m	150 dB/m	150 dB/m
Radius of pocket	2 cm	1 cm	3 cm

Table 3.14: Simulation Parameters of Case 3.2 for 600 Hz

	Replica data set	**Case 3.2A**	**Case 3.2B**
Speed of sound	30 m/s	30 m/s	30 m/s
Fat tissue thickness	2 cm	3 cm	3 cm
Attenuation	150 dB/m	150 dB/m	150 dB/m
Radius of pocket	2 cm	1 cm	3 cm

Table 3.15: Simulation Parameters of Case 3.3 for 600 Hz

	Replica data set	**Case 3.3A**	**Case 3.3B**
Speed of sound	30 m/s	40 m/s	40 m/s
Fat tissue thickness	2 cm	2 cm	2 cm
Attenuation	150 dB/m	150 dB/m	150 dB/m
Radius of pocket	2 cm	1 cm	3 cm

Table 3.16: Simulation Parameters of Case 3.4 for 600 Hz

	Replica data set	**Case 3.4A**	**Case 3.4B**
Speed of sound	30 m/s	30 m/s	30 m/s
Fat tissue thickness	2 cm	2 cm	2 cm
Attenuation	150 dB/m	170 dB/m	170 dB/m
Radius of pocket	2 cm	1 cm	3 cm

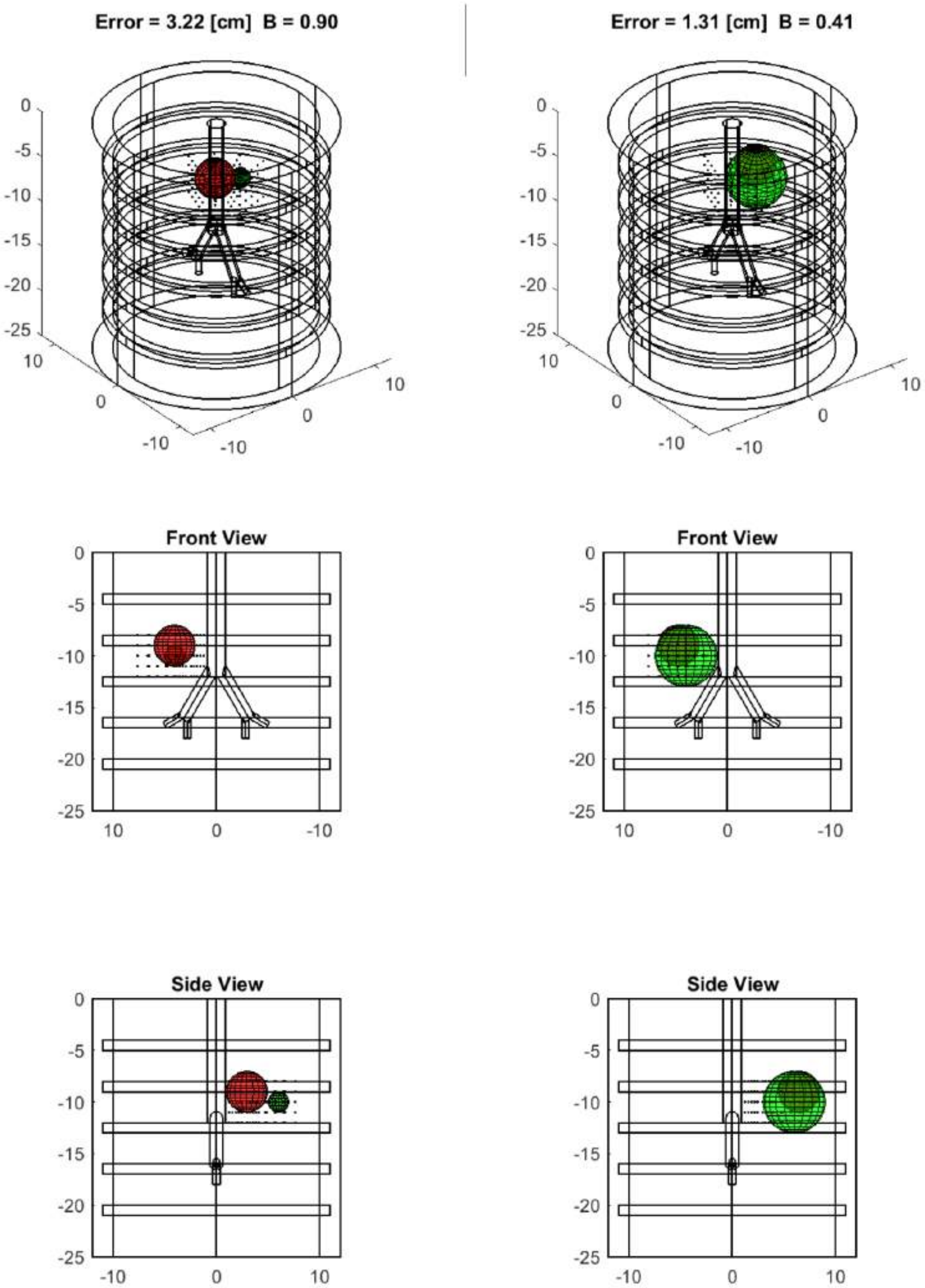

Figure 3.56: Results of the Linear Processor for Case 3.1A (left column) and Case 3.1B (right column) (red sphere represents the predicted pocket, green sphere represents the actual pocket, **Error** is the distance between the centers of the spheres, and **B** is the output of the processor). Dimensions are given in cm. Excitation frequency is 600 Hz.

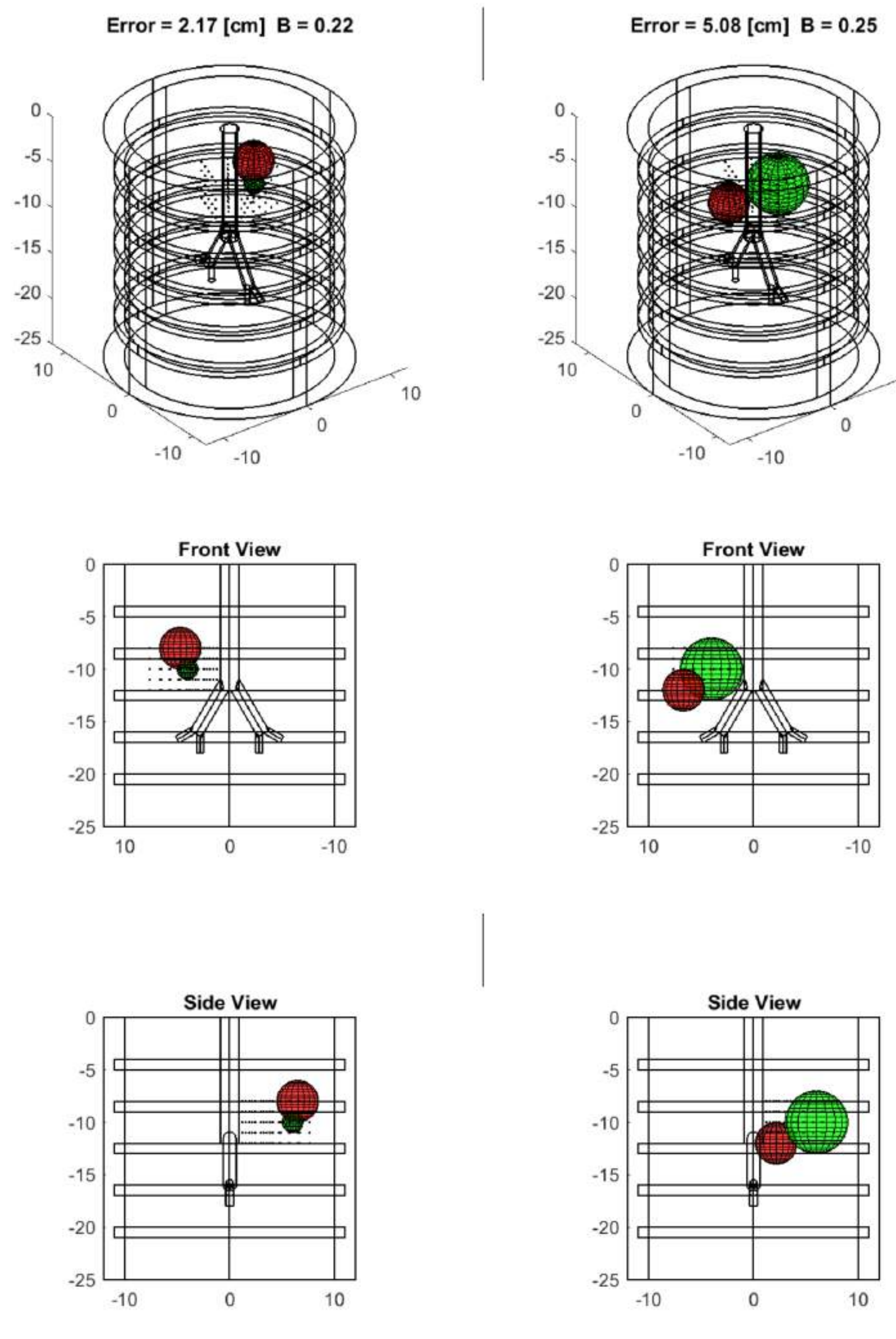

Figure 3.57: Results of the Linear Processor for Case 3.2A (left column) and Case 3.2B (right column) (red sphere represents the predicted pocket, green sphere represents the actual pocket, Error is the distance between the centers of the spheres, and B is the output of the processor). Dimensions are given in cm. Excitation frequency is 600 Hz.

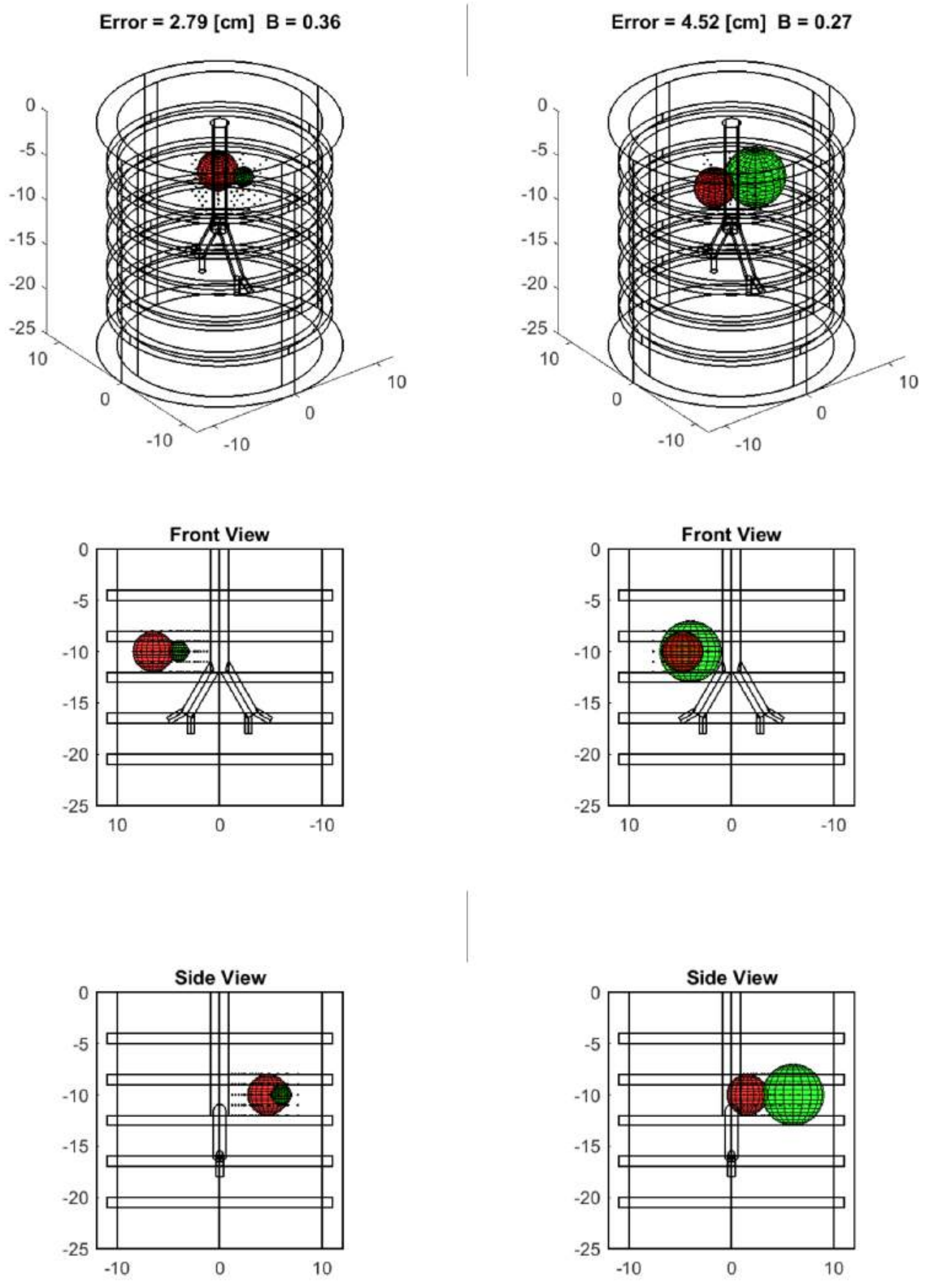

Figure 3.58: Results of the Linear Processor for Case 3.3A (left column) and Case 3.3B (right column) (red sphere represents the predicted pocket, green sphere represents the actual pocket, $\mathbf{Error}$ is the distance between the centers of the spheres, and $\mathbf{B}$ is the output of the processor). Dimensions are given in cm. Excitation frequency is 600 Hz.

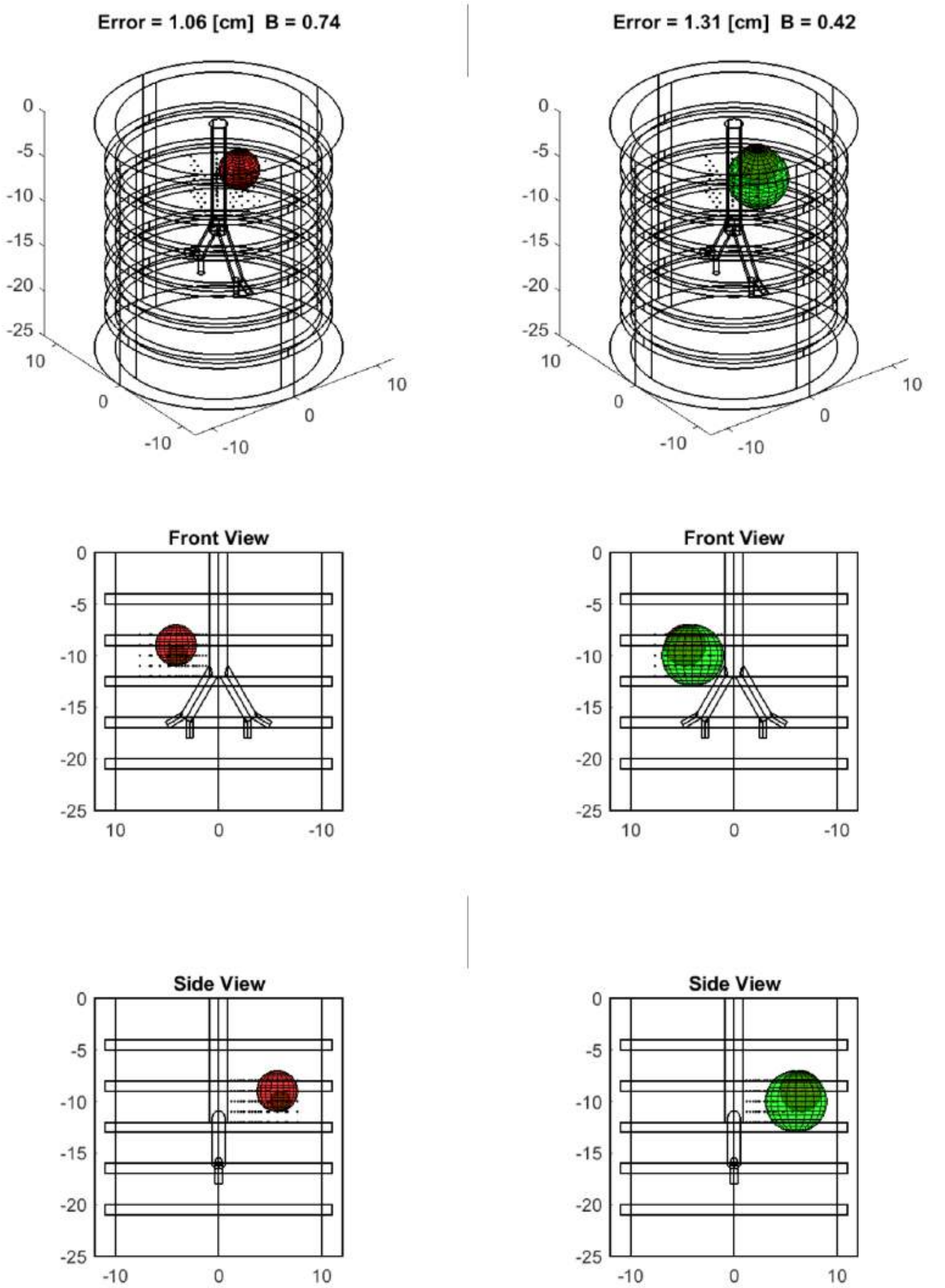

Figure 3.59: Results of the Linear Processor for Case 3.4A (left column) and Case 3.4B (right column) (red sphere represents the predicted pocket, green sphere represents the actual pocket, $\mathbf{Error}$ is the distance between the centers of the spheres, and $\mathbf{B}$ is the output of the processor). Dimensions are given in cm. Excitation frequency is 600 Hz.

3.4.3 Concluding Remarks on 3D Model

In Section 3.4.1, we performed acoustic imaging via Conventional Beamformer with Formulation IV using a short signals like previous section. For 400 Hz and 600 Hz, we identified the location of the abnormal region for two different positioning of the pocket. However, results did not provide the exact location of the water pocket, they only provided the approximate region of the abnormality. Although it is not possible to use this method as a definitive diagnosis, results showed that it could be used for the initial estimation of the region of interest for Matched-Field Processor. In other words, instead of placing the grid points, we use for the Matched-Field Processor everywhere and performing simulation for each location of the water pocket separately, we can greatly reduce the computation load by simply placing the grid points in the narrowed region pointed by the Conventional Beamformer.

Next section presented the results of Matched-Field Processor (see Section 3.4.2) for different cases. We used the processor by placing grid points not everywhere, but in the region indicated by the Conventional Beamformer. As with the 2D model, we evaluated the processor's tolerance for errors by creating inconsistencies between the experimental and replica data sets. The results showed that in most cases the abnormal area was located with considerably small errors.

CHAPTER 4

ACOUSTIC IMAGING OF THE HUMAN RESPIRATORY SYSTEM

In this chapter, details of the acoustic modeling of the human respiratory system and the acoustic imaging results are presented.

4.1 Acoustic Modeling of Human Respiratory System

It has been known in the literature for a long time that the respiratory system is modeled differently for acoustic analysis. In the first studies on this [15, 16], the respiratory system was modeled using simpler geometries, as we did in the third part. The image processing techniques that emerged with the developing technology made it possible to model more complex structures. In recent years, these techniques have been used in acoustic analysis studies and have yielded successful results [30, 3]. While creating the model we will analyze in this section, the methodology specified in these studies [30, 3] has been followed.

4.1.1 From Computed Tomography Images To 3D Model

Using CT images of a male human subject obtained online from the National Library of Medicine (NLM), Visible Human Project database repository [68], a complete 3D model of the human respiratory system was created. CT image sets were imported and processed using Mimics Innovation Suite 24.0 [69], a commercial image processing and 3D modeling software, to build 3D geometries from CT scans. Then, radiological sections were opened in axial, coronal, and sagittal image projections. Areas were determined by masking by assigning Hounsfield Unit (HU) values. Using the Segment module of Mimics software, the structures were segmented by following the anatomical border relationship of the related fat tissue, rib cage, parenchyma, and airway. For the detailed modeling of 3D models obtained from Mimics software, the design module in Mimics was transferred to 3-matic 16.0 [70]. Using design commands in 3-matic, the pattern model of the parenchyma was designed for the lumen of the airway model. The obtained numerical model was exported in .stl format.

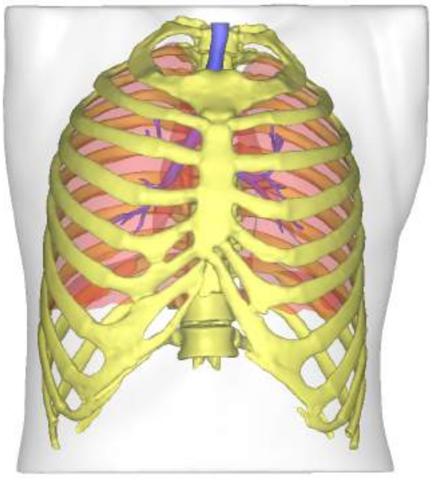

Figure 4.1: Obtained 3D model from the CT Images

4.1.2 Material Selection

The methodology determined in the third chapter has been followed in the assignment of the material properties to the each tissue (see section 3.1.2). Material selections are given in the Table 4.1.

4.1.3 Finite Element Modeling

Finite element analysis of the human respiratory system was conducted by using COMSOL Multiphysics [63]. Pressure Acoustics, Transient and Pressure Acoustics, Frequency Domain modules were used to simulate the acoustic wave propagation through the bronchial airway, parenchyma, and abnormal region for both time and frequency domains, respectively. Solid Mechanics module was used to simulate fat

Table 4.1: Acoustical and mechanical properties of the tissues

Bronchial airway		
Speed of sound	c_{air}	$343[m/s]$
Density	ρ_{air}	$1.2[kg/m^3]$
Parenchyma		
Speed of sound	c_{lung}	$30[m/s]$
Density	ρ_{lung}	$160[kg/m^3]$
Attenuation	α_{lung}	$150[dB/m]$
Fat tissue		
Speed of sound	c_{fat}	$1450[m/s]$
Density	ρ_{fat}	$970[kg/m^3]$
Young's Modulus	E_{fat}	$0.75[MPa]$
Poisson's ratio	ν_{fat}	0.49
Abnormal region		
Speed of sound	c_{water}	$1480[m/s]$
Density	ρ_{water}	$997[kg/m^3]$

Table 4.2: Selected physic modules for finite element analysis

Region	**Physic Module**	**Fluid/Solid Model**
Bronchial airway	Pressure Acoustics, Transient/Frequency	Linear elastic fluid
Parenchyma	Pressure Acoustics, Transient/Frequency	Linear elastic fluid
Abnormal region	Pressure Acoustics, Transient/Frequency	Linear elastic fluid
Fat tissue	Solid Mechanics	Isotropic solid

tissue. Rib cages were not included to simulations due to computational limitations. The Acoustic-Structure Interaction module was applied to couple the boundaries of the the Pressure Acoustics and Solid Mechanics physics. Details are given in Table 4.2.

4.1.3.1 Boundary Conditions

A free-free boundary condition was defined for the outside of the fat tissue where solid mechanical module was used [3]. For the acoustic excitation of the numerical model, a harmonic pressure wave with the magnitude of 1 Pascal was introduced to the bronchial airway inlet.

4.1.3.2 Mesh Generation

The 3D model of each part of the human respiratory system was imported into ANSYS ICEM CFD 14.5.7, a finite element meshing software [71], which was to generate the finite element model illustrated in Figure 4.2. The unstructured mesh consists of 492,506 tetrahedral elements and 59,393 triangular elements. Minimum mesh quality was obtained as 0.2, which is shown in Figure 4.3. Then, obtained numerical model was exported to the COMSOL Multiphysics [63] in NASTRAN format.

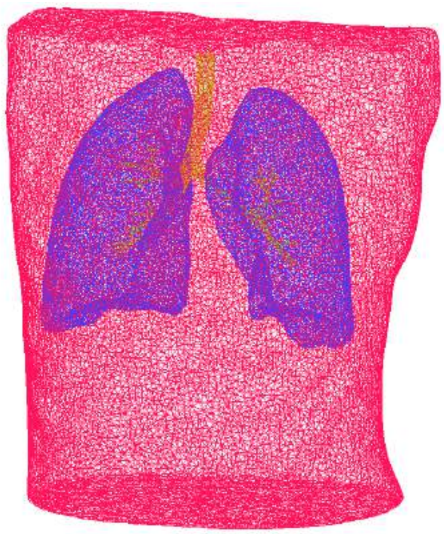

Figure 4.2: Mesh generated model

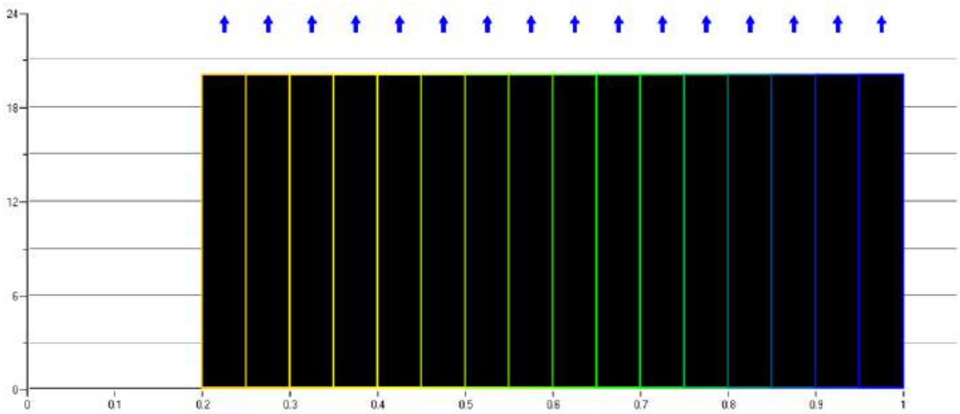

Figure 4.3: Mesh quality obtained from ANSYS ICEM CFD

4.1.3.3 Microphone Configuration

16 microphones were on arbitrarily determined points on the front side of the human chest to obtain the velocity data from the time analysis. It has been seen that the data obtained from 16 microphones is not sufficient for frequency analysis and the Linear Processor, so 16 extra measurement points were selected from the front side of the fat tissue. These measurement points are shown in Figure 4.4.

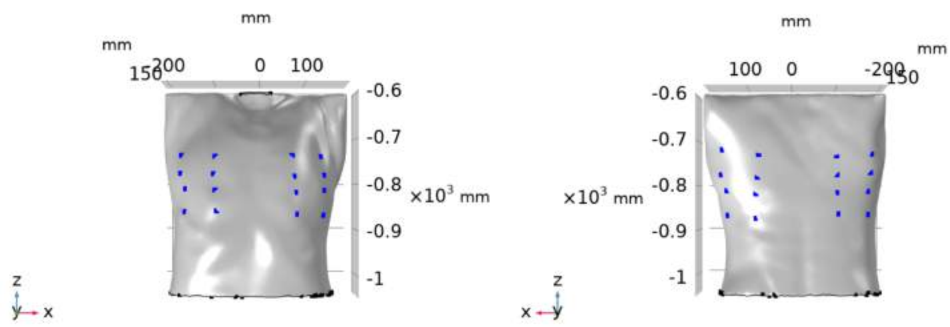

Figure 4.4: Selected measurement points from the front side (left), and the back side (right) of the fat tissue.

4.2 Results of the Conventional Beamformer

In this section, the results of the Conventional Beamformer are presented. We conducted two different simulations. In Case 4.1, we placed the water pocket with a 3 cm radius to the left lobe's upper side, shown in Figure 4.5 (left). Figure 4.5 (right) shows the second case (Case 4.2) where the pocket is located at the right lobe's bottom side. We have used the same approach as the previous chapter in implementing the beamformer; we obtained 2D acoustic images by slicing the numerical model at 1 cm intervals on the z-axis. For both cases, the insonification frequency was taken as 600 Hz.

Figure 4.6 and Figure 4.7 show the results of Case 4.1. Each sub-figure corresponds to each 2D acoustic image of the specified height. Sub-figures obtained for the heights between z=-710 mm and z=-770 clearly show the location of the water pocket. Any dominant side-lobe did not appear in the results.

For Case 4.2, Figure 4.9 shows the approximate position of the water pocket. However, Figure 4.8 presents the dominant side lobe, which has appeared as another water pocket located at the upper side of the parenchyma.

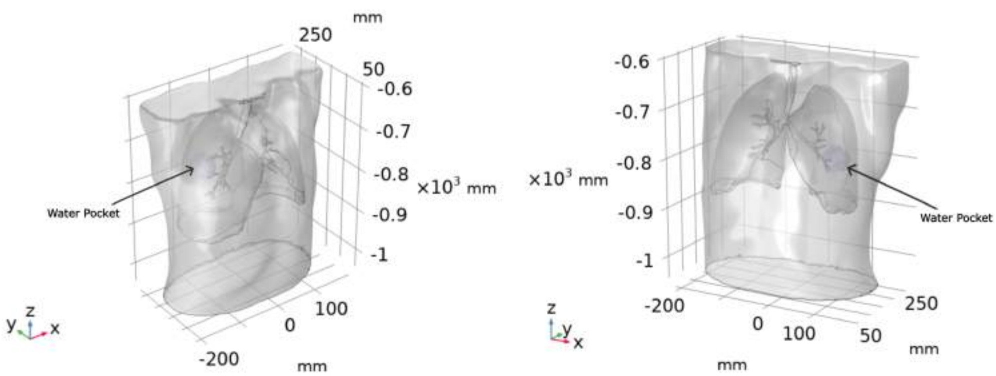

Figure 4.5: Case 4.1 (left) and Case 4.2 (right)

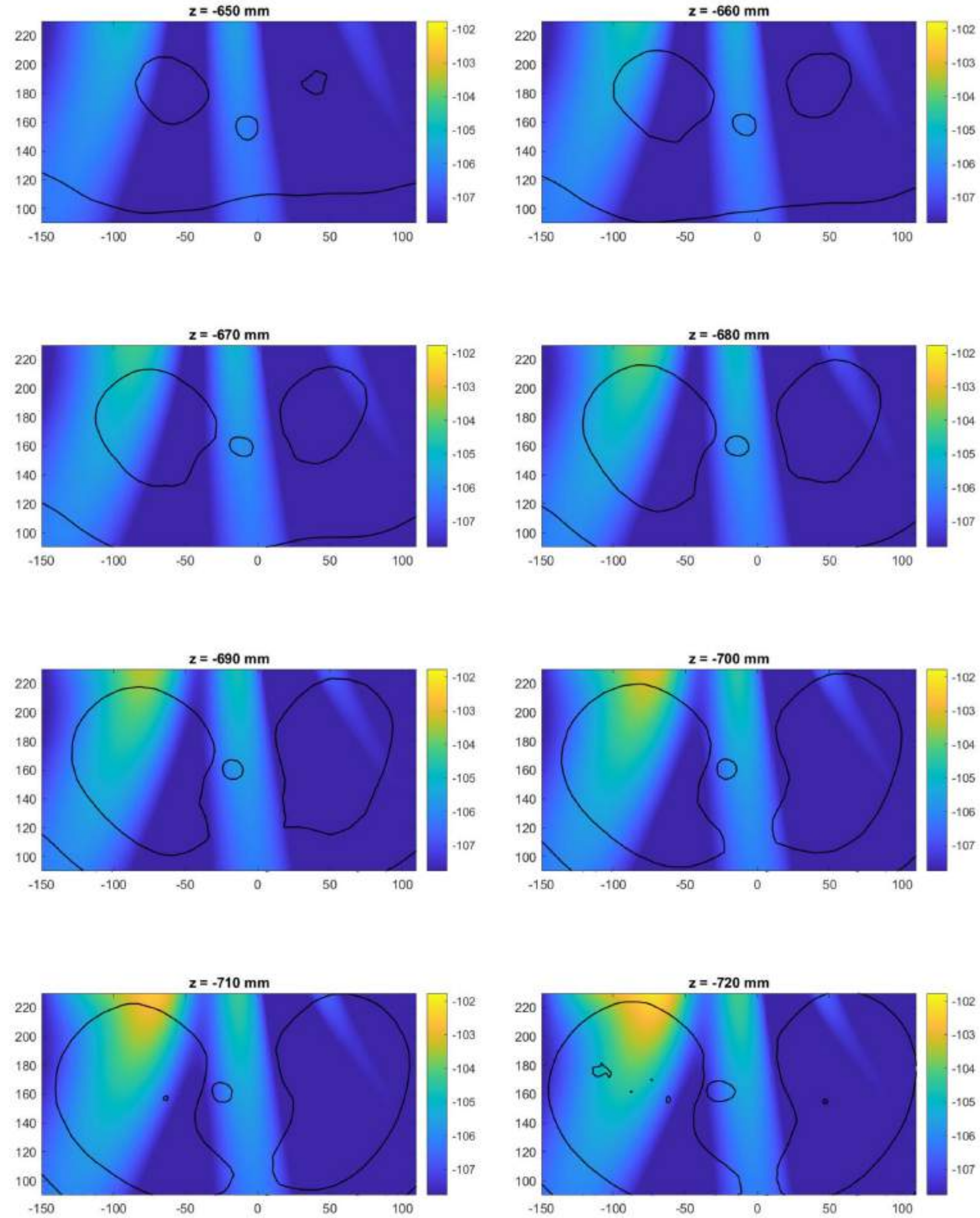

Figure 4.6: Acoustic pressure fields (SPL [dB]) obtained by processing signals of 0.002 seconds length at 600 Hz through the Conventional Beamformer with Formulation IV for the Case 4.1. Radius of the pocket is 3 cm. Dimensions are given in mm.

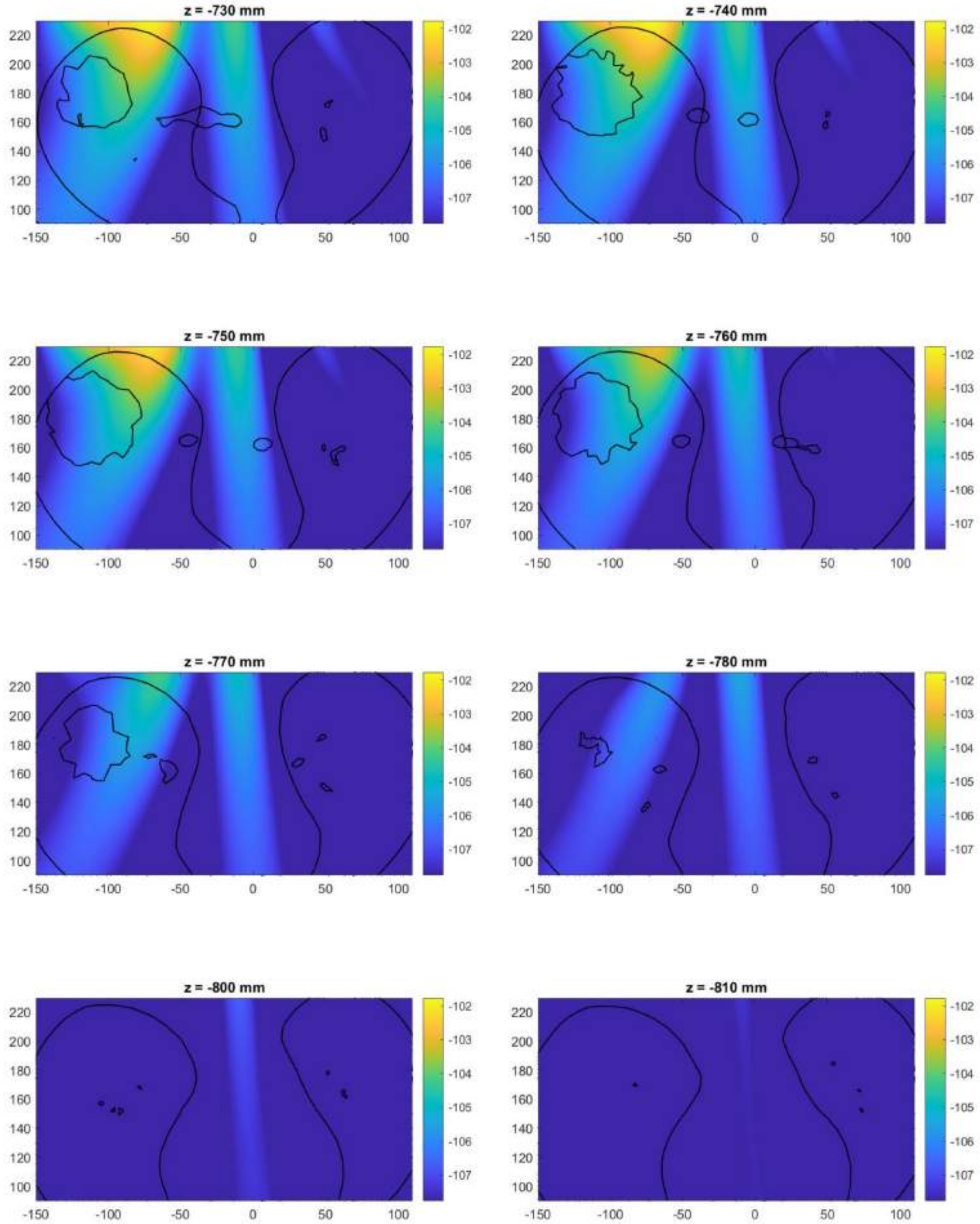

Figure 4.7: Acoustic pressure fields (SPL [dB]) obtained by processing signals of 0.002 seconds length at 600 Hz through the Conventional Beamformer with Formulation IV for the Case 4.1. Radius of the pocket is 3 cm. Dimensions are given in mm.

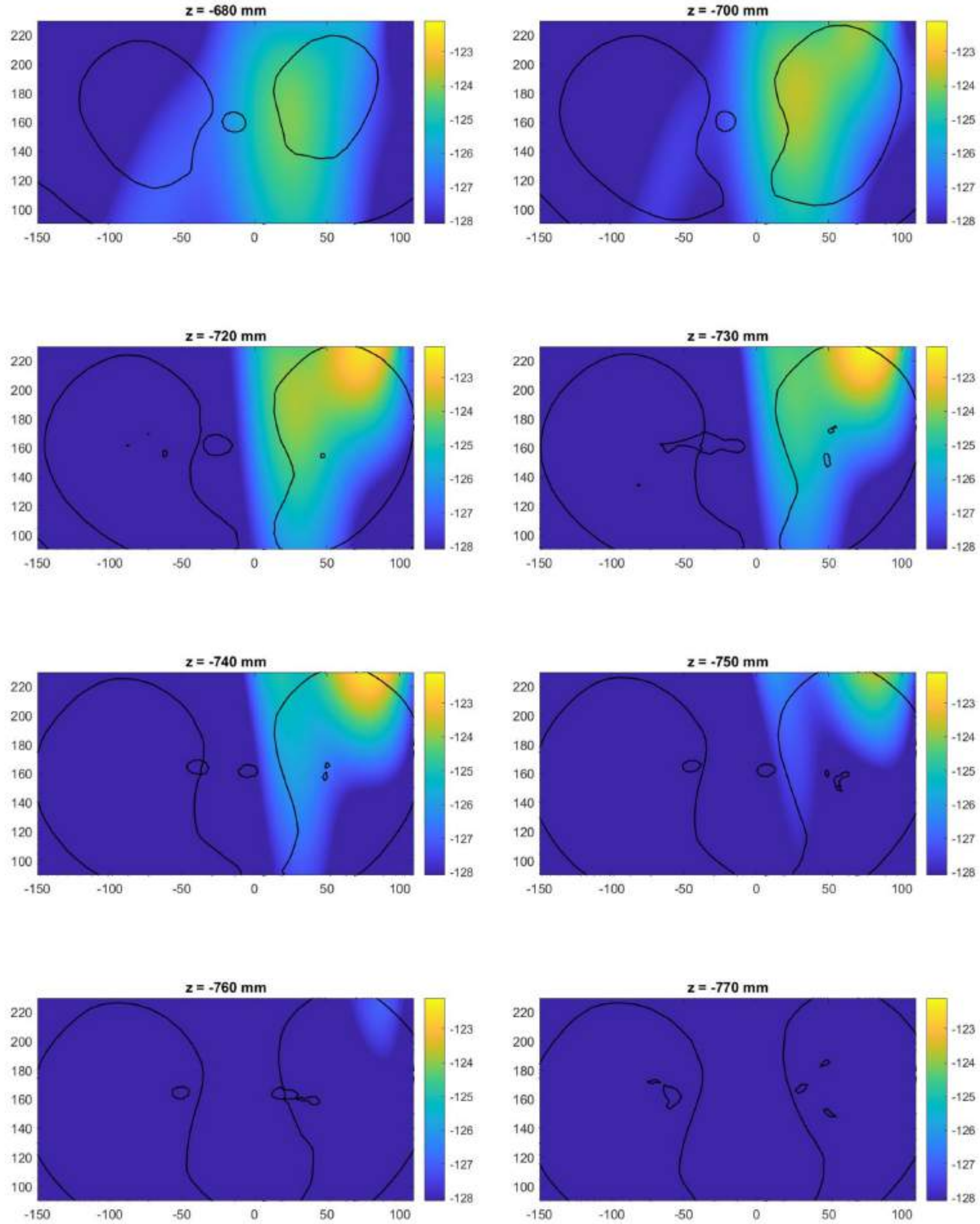

Figure 4.8: Acoustic pressure fields (SPL [dB]) obtained by processing signals of 0.002 seconds length at 600 Hz through the Conventional Beamformer with Formulation IV for the Case 4.2. Radius of the pocket is 3 cm. Dimensions are given in mm.

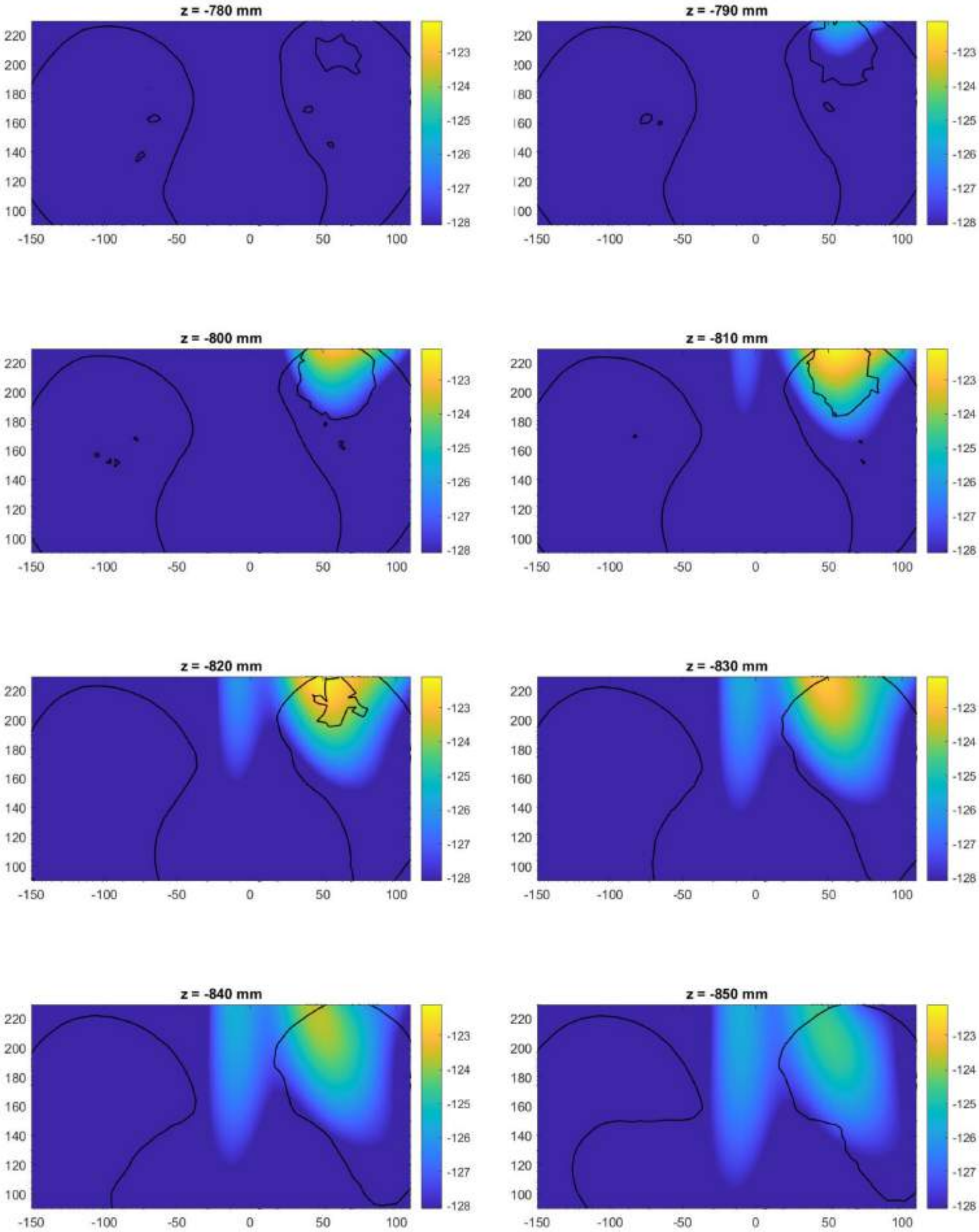

Figure 4.9: Acoustic pressure fields (SPL [dB]) obtained by processing signals of 0.002 seconds length at 600 Hz through the Conventional Beamformer with Formulation IV for the Case 4.2. Radius of the pocket is 3 cm. Dimensions are given in mm.

4.3 Results of the Linear Processor

The findings of the Linear Processor are presented in this section. To produce replica and experimental data sets, frequency domain analysis was performed at 600 Hz. Grid points are selected randomly from one lobe of the parenchymal tissue. We conducted six case studies to understand the tolerance of the method regarding mismatches.

In Case 5.1, we placed the pocket at a point that was also used as a grid point while generating replica data sets. Also, to verify the perfect case where the output of the processor should be equal to 1, we did not employ any mismatch between data sets. The left column of the Figure 4.10 shows that our processor presented the correct location and maximum output. In the following case (Case 5.2), we only reduced the radius of the particle without changing the pocket's location. The right column of the Figure 4.10 shows that a 0.5 cm reduction in the radius only created a one percent error in terms of the processor's output.

Figure 4.11 shows the results of Case 5.3 and Case 5.4. For Case 5.3, we created a pocket of water with a radius of 2 cm and placed it at a distance of 1 cm from the nearest point for the experimental data set. Left column of Figure 4.11 shows that Case 5.3 had the highest error among all cases in terms of pocket localization, predicting the pocket below the parenchymal lobe. This can be explained by the fact that the water pocket did not affect the wave propagation, so the processor gave almost maximum correlation with the lowest grid point, which should be the least effective location for the signals. It can also be concluded that the water pocket with a diameter of 3 cm in the lower part of the lung had almost no effect on wave propagation.

In Case 5.4, the same location was used for the experimental pocket, but the radius was increased from 2 cm to 3.5 cm. The right column of Figure 4.11 shows that localization was achieved with a 1 cm error which is the minimum error than can be obtained for this configuration of the grid points. The correlation level was also compatible with the localization results.

The experimental data set of Case 5.5 gave the second highest error and lowest correlation among all other cases, which is shown in the left column of Figure 4.12. In addition to mismatches employed in Case 5.4, we also changed the speed of sound from 30 m/s to 40 m/s while generating the experimental data set. Similar to the results of the previous section, we obtained the highest error in this situation. The right column of Figure 4.12 (Case 5.6) shows that when we employ mismatch between sound attenuation, we successfully predicted the location of the pocket with high correlation. This result is also consistent with the result obtained in Chapter 3 in the analysis of the 3D configuration.

Table 4.3: Simulation Parameters of Case 5.1 and Case 5.2 for 600 Hz

	Replica data set	**Case 5.1**	**Case 5.22**
Speed of sound	30 m/s	30 m/s	30 m/s
Attenuation	150 dB/m	150 dB/m	150 dB/m
Radius of pocket	3 cm	3 cm	2.5 cm
Dist. to closest grid point	-	0 cm	0 cm

Table 4.4: Simulation Parameters of Case 5.3 and Case 5.4 for 600 Hz

	Replica data set	**Case 5.3**	**Case 5.4**
Speed of sound	30 m/s	30 m/s	30 m/s
Attenuation	150 dB/m	150 dB/m	150 dB/m
Radius of pocket	3 cm	2 cm	3.5 cm
Dist. to closest grid point	-	1 cm	1 cm

Table 4.5: Simulation Parameters of Case 5.5 and Case 5.6 for 600 Hz

	Replica data set	**Case 5.5**	**Case 5.6**
Speed of sound	30 m/s	40 m/s	30 m/s
Attenuation	150 dB/m	150 dB/m	180 dB/m
Radius of pocket	3 cm	3.5 cm	3.5 cm
Dist. to closest grid point	-	1 cm	1 cm

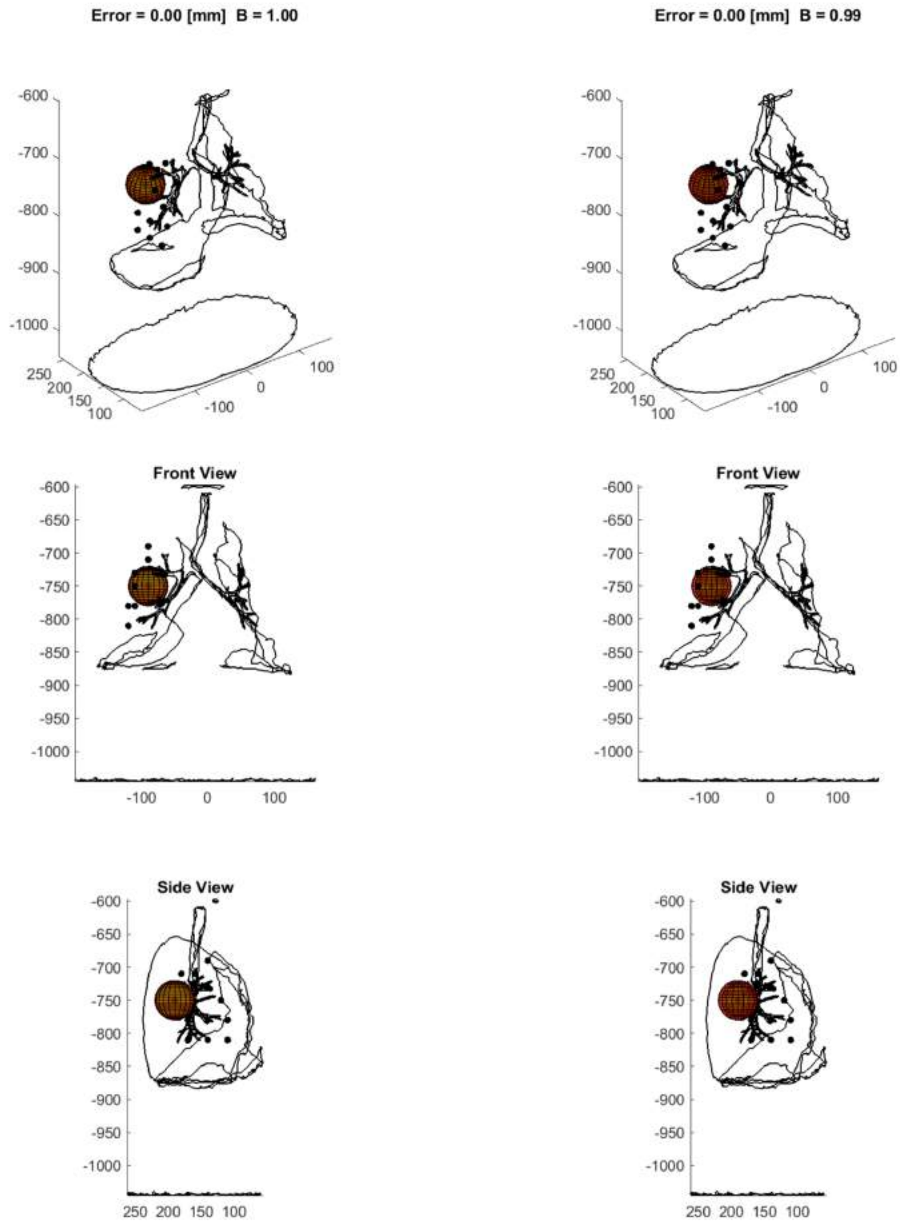

Figure 4.10: Results of the Linear Processor for Case 5.1 (left column) and Case 5.2 (right column) (red sphere represents the predicted pocket, green sphere represents the actual pocket, **Error** is the distance between the centers of the spheres, and **B** is the output of the processor). Dimensions are given in mm. Excitation frequency is 600 Hz.

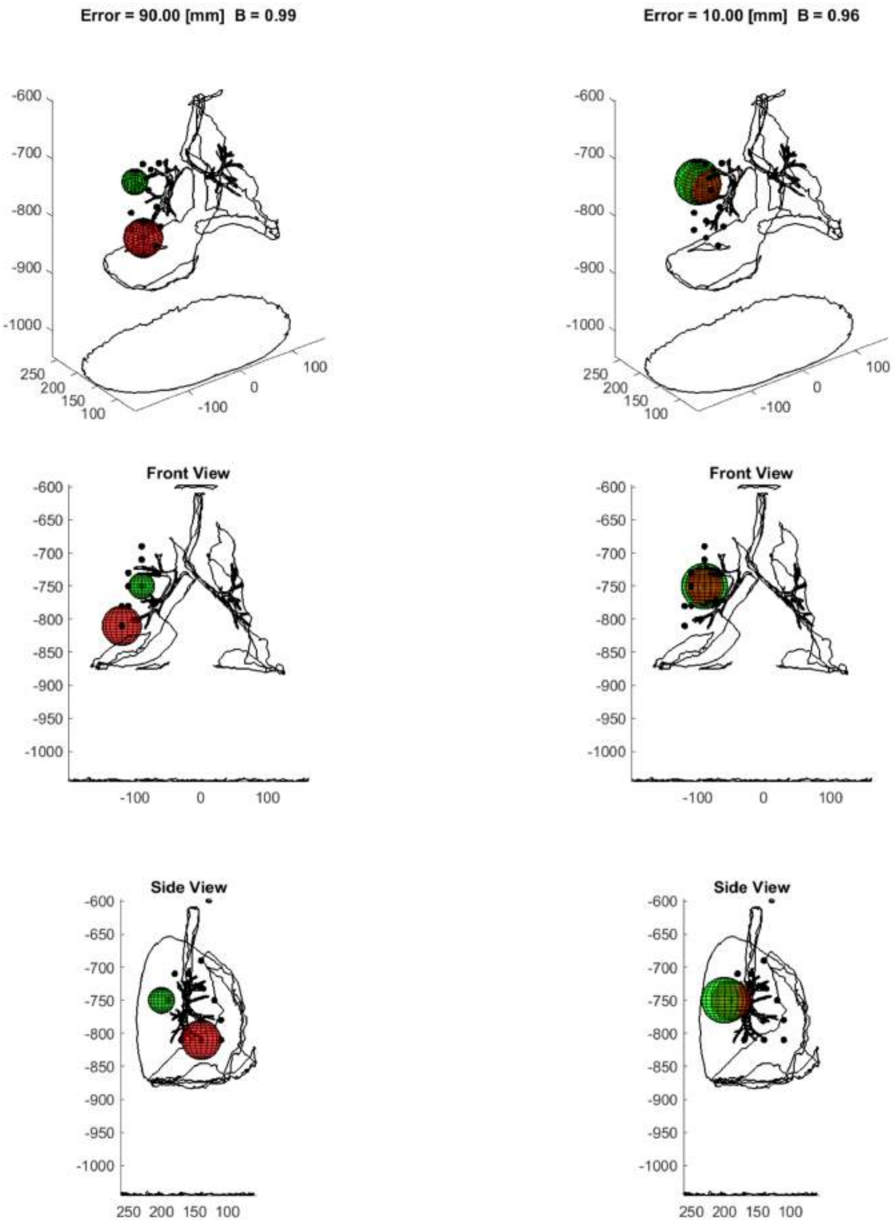

Figure 4.11: Results of the Linear Processor for Case 5.3 (left column) and Case 5.4 (right column) (red sphere represents the predicted pocket, green sphere represents the actual pocket, **Error** is the distance between the centers of the spheres, and **B** is the output of the processor). Dimensions are given in mm. Excitation frequency is 600 Hz.

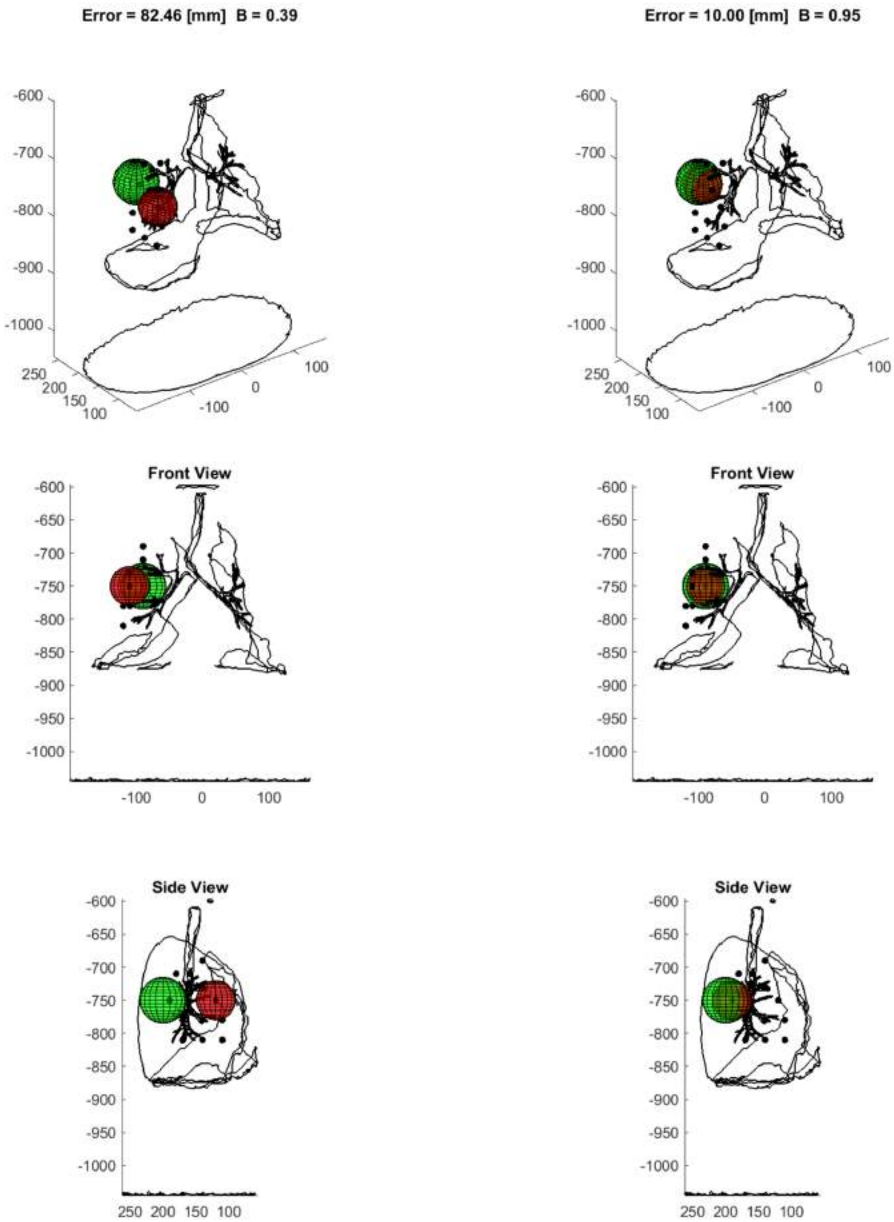

Figure 4.12: Results of the Linear Processor for Case 5.5 (left column) and Case 5.6 (right column) (red sphere represents the predicted pocket, green sphere represents the actual pocket, $\mathbf{Error}$ is the distance between the centers of the spheres, and $\mathbf{B}$ is the output of the processor). Dimensions are given in mm. Excitation frequency is 600 Hz.

CHAPTER 5

MANUFACTURING OF THE SYNTHETIC EXPERIMENTAL MODEL

One of the main objectives of this study is to produce the synthetic experimental model of the human respiratory system. Our motivation for the usage of this type of model was discussed in detail in Chapter 1. In this chapter, we have presented the details of the manufacturing of the experimental model.

5.1 Production Methodology

Since 3D printers allow us to produce more complex geometries than traditional production methods, we prefer additive manufacturing methods for most of the production process. Each part of the human respiratory system was produced separately. For the production of the bronchial airway, molds of the parenchymal tissue, and rib chest, Formlabs's Form 3+ 3D printer, which is shown in Figure 5.1, was used.

Figure 5.1: Formlabs's Form 3+ 3D Printer.

Form 3+ 3D printer relies on the technique called Low Force Stereolithography (LFS) which transforms the liquid resin into fresh, clean solid pieces using a flexible tank and linear lighting using a laser [72] . The technical specifications [72] of the Form 3+ have been given in Table 5.1. Considering the build volume of the 3D printer, the experimental model was scaled down by 2/3.

Table 5.1: Technical specifications of Form 3+

Specification	**Value**
Build volume	145 mm × 145 mm × 185 mm
Layer thickness	25 - 300 µm
XY resolution	25 µm
Laser power	250 mW

After obtainiing the 3D model of the airway, we fixed the damaged surfaces and made the model cleaner. The first version of the model and the final version used for fabrication are shown in Figure 5.2. We tried to minimize the wall thickness of the bronchial airway, since we neglected the thickness of the wall thickness in the simulations. Considering the resolution of the 3D printer, and ensuring the continuous flow within the airway, the wall thickness was taken as 1 mm.

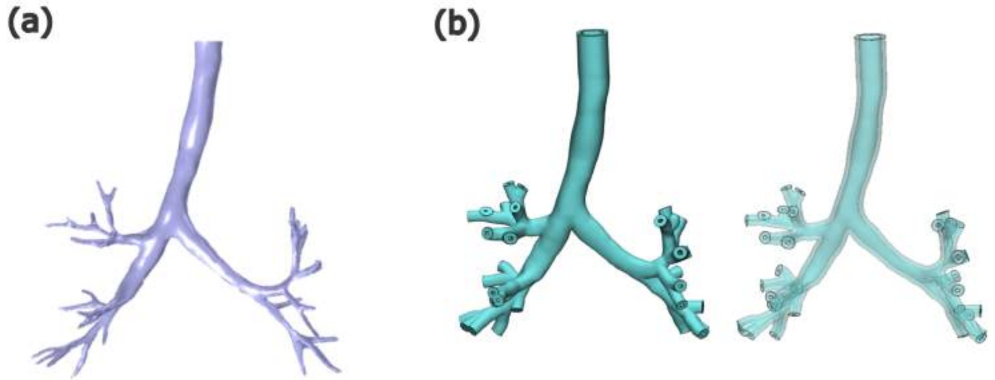

Figure 5.2: First model of the airway (left), and model used for the fabrication (right).

A lung mold was designed to produce lung tissue from polyurethane foam. By creating the lung mold in two parts, it was aimed to easily remove the foam tissue from the mold. The 3D model of the lung molds is shown in Figure 5.3. Two large holes were added to the top of the back molds to pour the liquid polyurethane mix into the mold. Extra small holes were created at the top of the front molds' surface to evacuate the excess foam. Support rods were added between them to prevent the molds from slipping and increase their stability. M3-sized bolt holes were created for connecting the front and back molds.

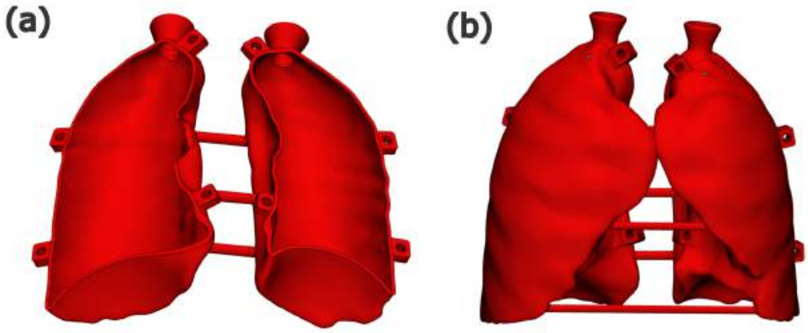

Figure 5.3: Lung molds.

The rib cage was produced using the 3D model shown in Figure 5.4. The rib cage was slightly enlarged to fit the lung mold inside the rib cage.

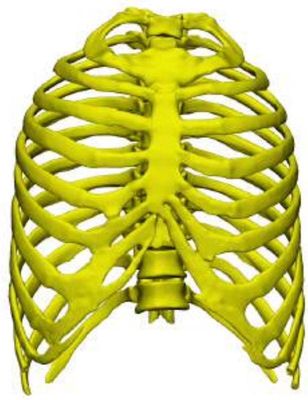

Figure 5.4: 3D model of the rib cage.

Figure 5.6 shows the arrangement of the lungs and the airway. The holes in the airway outlet were closed using tape. After the polyurethane was cured, the molds were separated from the foam part and placed in the rib cage together with the airway.

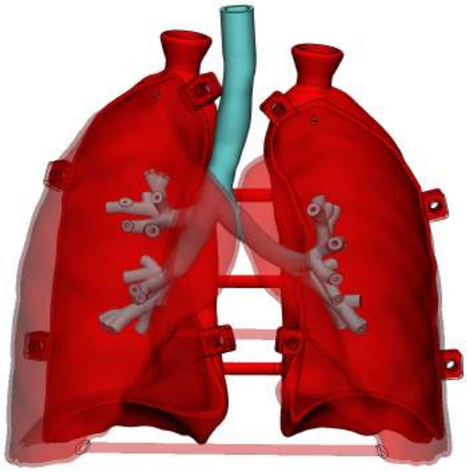

Figure 5.5: Arrangement of the lung and the bronchial airway.

5.2 Material Selection

Formlabs Flexible 50A Resin was selected due to the material's high elasticity for the bronchial airway. According to the datasheet of the manufacturer [73], Flexible 50A has the following properties: elongation at break 100%, tensile strength: 3.7 MPa, shore hardness: 70A, and tear strength: 11 kN/m. The rib cage and lung molds were manufactured using Formlabs Standard Gray Resine with the following properties [74]: elongation at break 6.2%, tensile strength: 2.8 GPa, and flexural modulus: 2.2 GPa. This material was chosen because it has mainly mechanical properties similar to PMMA.

We used molds to obtain the lung-shaped structure from the polyurethane foam. Ozer used Flex Foam-IT X [16] polyurethane foam with 160 kg/m^3 density as an experimental model due to its comparability with the parenchymal tissue in terms of speed of sound and attenuation. Since that material was out of stock, we used Flex Foam-IT III, where the material density is 50 kg/m^3.

According to Avigo's study [61], PDMS has similar acoustic properties to the adipose tissue and skeletal muscle, so to mimic the fat tissue, we decided to use PDMS Silicone oil. The density of the material is 1500 kg/m^3 and speed of sound is 1300 m/s. At this point, we have not manufactured the fat tissue, but PDMS will be used in future studies.

5.3 Manufacturing Process

As it was mentioned in the previous section, most of the parts have been produced by using Formlabs Form 3+. Only the rib cage was manufactured in Formlabs Form 3L which has a larger build volume. Other specifications of the printer are same with Form 3+. Layer thickness was taken as $100 \mu m$. In the post-manufacturing, the printed parts were washed with isopropyl alcohol and cured under UV. Curing was performed at $60°C$ for 15 minutes using Formlabs Form Cure. Details of the manufacturing process have been presented in the following figures.

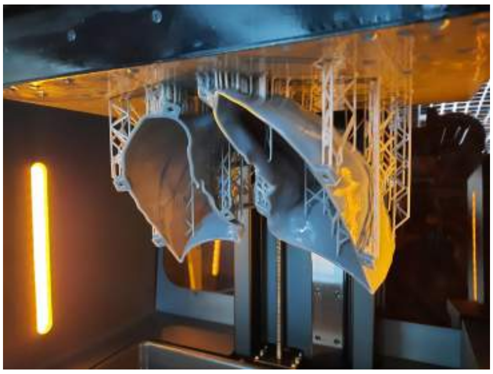

Figure 5.6: Lung molds in the 3D printer.

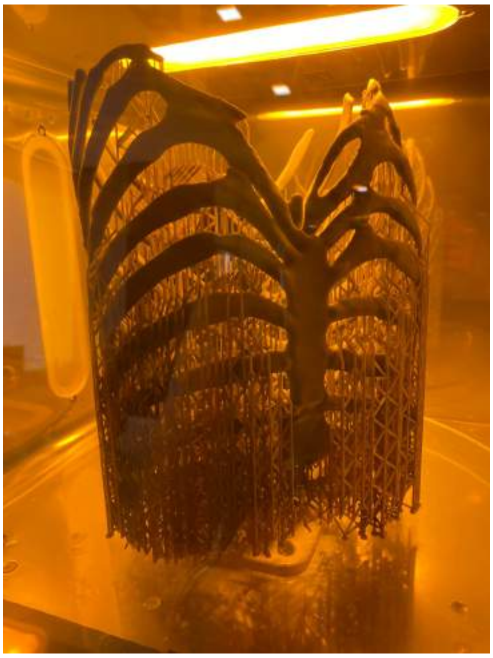

Figure 5.7: Curing process of the rib cage.

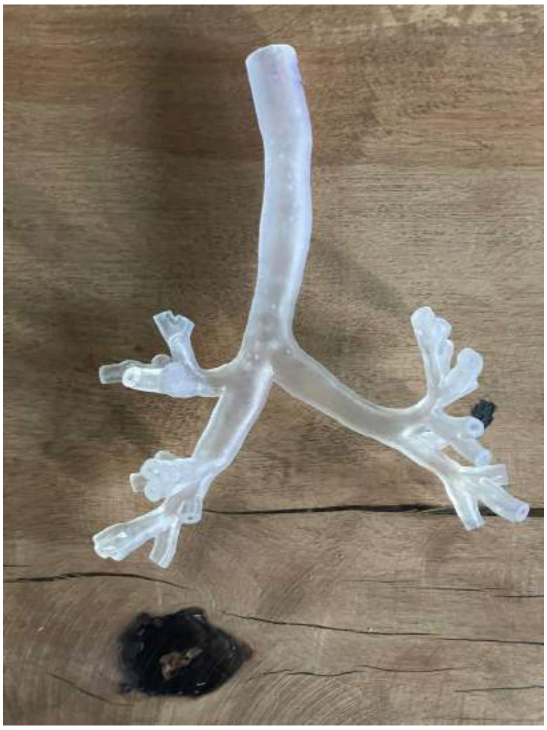

Figure 5.8: Manufactured bronchial airway.

Figure 5.9: Placement of the bronchial airway and back side of the lung mold.

In order to obtain a lung-shaped geometry from polyurethane foam, we placed the bronchial airway as in Figure 5.9 and closed the lung mold using bolts. In addition, silicone is drawn to all inner surfaces to prevent leakage. We mixed the polyurethane foam in the dimensions shown in Figure 5.10 and poured it into the mold in liquid form. It took about 3 hours for the polyurethane to cure.

Figure 5.10: Raw materials of the polyurethane in liquid form (mixture ratio: 1A:2B).

Figure 5.11: Curing process of the polyurethane foam within the lung mold.

Figure 5.12: Lung phantoms and bronchial airway.

Figure 5.13: Lung phantoms, bronchial airway and rib cage.

CHAPTER 6

CONCLUSION

6.1 Summary

In this study, we performed a numerical investigation of the two main acoustic imaging methods focusing on the potential use for diagnostic of the human respiratory system diseases. The first method, the Conventional Beamformer, was employed using responses obtained from the time-domain analysis, and the second method, Matched-Field Processor, was applied using frequency-domain responses. These methods were applied to the 2D simple model of the human respiratory system, and the results were presented at the beginning of Chapter 3 to evaluate their performances. We had four different steering vectors, which are used to create an acoustic image through the Conventional Beamformer. We compared the performances of steering vectors for each case of the 2D model. For Matched-Field Processor, we also employed two different approaches and compared their performances. In the continuation of the chapter, we verified the findings obtained from the 2D model with the 3D model. In Chapter 4, we generated the complete numerical model of the human respiratory system by processing the open-source CT images of the healthy human. The numerical model was used to verify the findings obtained from the previous chapter by employing acoustic imaging methods. Lastly, we provided the details of the fabrication process of the synthetic experimental model in Chapter 5.

6.2 Discussion

First of all, we used acoustic imaging methods at the beginning of this study, assuming that the abnormal region within the parenchymal tissue behaves like a high-intensity region. We applied the Conventional Beamformer and Matched-Field Processors separately to verify this assumption. The results obtained from the 2D model showed that this kind of assumption is not always correct and valid when we processed the long signals with the Conventional Beamformer. The same behavior was observed when we used the frequency domain responses of the 2D model to express the region with multiple monopole sources through Matched-Field Processors. However, one important finding obtained from the time-domain analysis of the 2D model was that the first signals reached the microphone closest to the water pocket, which reflected the behavior we expected from a sound source. When we used the signals obtained from about the first two periods with the Conventional Beamformer, we observed that this behavior was correct. The abnormal region usually appeared as a sound source in the output of Formulation IV. Other steering vector formulations did not provide meaningful and correct results regarding our assumption.

In using Matched-Field Processors with the 2D model, we sought an answer to whether we can create the abnormal region itself instead of expressing the field with multiple sound sources. Since we only have the numerical model, we created mismatches between the replica and experimental data sets we used and compared the performance of the Linear and MVDR Processors against these errors which were arised from the mismatches. As expected, the Linear Processor behaved more robust against these mismatched and presented the location of the abnormal region with a certain error in most cases.

For the 3D model, we employed the Conventional Beamformer with Formulation IV using short signals and obtained similar results regarding the localization of the abnormal region. However, acoustic images did not provide the exact location, they only presented specified regions. We decided to use this specified region to decrease the number of grid points we used for the Matched-Field Processor. In other words, we narrowed the region using the information obtained from the Conventional Beamformer to decrease the computational time required for the generation of the replica data sets used for the Linear Processor. The processor presented the location of the abnormal region with a certain error when we created the grid points in the narrowed region and employed environmental mismatches between data sets.

We performed studies by using the exact numerical model of the human respiratory system to verify findings obtained from simple models. For different cases, the Conventional Beamformer allowed us to narrow the region, and the Linear Processor provided the location of the water pocket. We also observed that results were better when we compared with the 3D simple model. We think that this is because the 3D model is symmetrical, and the asymmetry is more useful in obtaining a unique answer.

The results of this thesis provide a better understanding of acoustic imaging of the human respiratory system for diagnostic purposes. We hope that this study will help us to understand the sound generation and propagation within the human thorax, and to develop high resolution, cost-effective, safe, and non-invasive medical imaging technologies.

6.3 Future Work

As future work, we should concentrate on validating the results from acoustic imaging methods with a synthetic experimental model of the human respiratory system. In addition, by modeling the physics models and material choices used in the numerical model in a way similar to human biology, the same studies with actual human subjects should also be performed as an extension of this study.

In order to understand the effect of the environmental parameters on the results, a more parametric study using the numerical model with real geometry can be presented as another future work, as it will be beneficial for us to understand the lung acoustics and the potential of the acoustic imaging techniques.

As mentioned previously, Matched-Field Processors can be used to identify the mechanical and acoustical properties of the numerical model by processing the numerical results with experimental data set obtained from the real human/animal subjects.

By this way, we can obtain the closest values of the properties by trying to increase the correlation between the replica and experimental data sets.

Lastly, machine learning and image processing algorithms can be included in the proposed methodology as another future work. We can use these algorithms to understand the relations between models, model parameters, and acoustic images, and these relations can be used for diagnostic purposes.

REFERENCES

[1] R. L. Wilkins, J. E. Hodgkin, and B. Lopez, *Fundamentals of lung and heart sounds*. Mosby, 2004.

[2] R. T. H. Laennec, "A treatise on diseases of the chest and on mediate auscultation," *Translated by John Forbes*, 1819.

[3] H. Palnitkar, B. M. Henry, Z. Dai, Y. Peng, H. A. Mansy, R. H. Sandler, R. A. Balk, and T. J. Royston, "Sound transmission in human thorax through airway insonification: an experimental and computational study with diagnostic applications," *Medical & Biological Engineering & Computing*, vol. 58, no. 10, pp. 2239–2258, 2020.

[4] D. A. Rice, "Sound speed in pulmonary parenchyma," *Journal of Applied Physiology*, vol. 54, no. 1, pp. 304–308, 1983.

[5] K. N. Priftis, L. J. Hadjileontiadis, and M. L. Everard, *Breath sounds: from basic science to clinical practice*. Springer, 2018.

[6] J. L. Sutton, "Underwater acoustic imaging," *Proceedings of the IEEE*, vol. 67, no. 4, pp. 554–566, 1979.

[7] M. Bai and J. Lee, "Industrial noise source identification by using an acoustic beamforming system," 1998.

[8] S. Doclo, S. Gannot, M. Moonen, A. Spriet, S. Haykin, and K. R. Liu, "Acoustic beamforming for hearing aid applications," *Handbook on array processing and sensor networks*, pp. 269–302, 2010.

[9] T. Royston, X. Zhang, H. Mansy, and R. Sandler, "Modeling sound transmission through the pulmonary system and chest with application to diagnosis of a collapsed lung," *The Journal of the Acoustical Society of America*, vol. 111, no. 4, pp. 1931–1946, 2002.

[10] Y. Peng, Z. Dai, H. A. Mansy, B. M. Henry, R. H. Sandler, R. A. Balk, and T. J. Royston, "Sound transmission in porcine thorax through airway insonification,"

Medical & biological engineering & computing, vol. 54, no. 4, pp. 675–689, 2016.

[11] S. S. Kraman, "Determination of the site of production of respiratory sounds by subtraction phonopneumography," *American review of respiratory disease*, vol. 122, no. 2, pp. 303–309, 1980.

[12] G. Benedetto, F. Dalmasso, and R. Spagnolo, "Surface distribution of crackling sounds," *IEEE transactions on biomedical engineering*, vol. 35, no. 5, pp. 406–412, 1988.

[13] M. Kompis, H. Pasterkamp, Y. Oh, and G. R. Wodicka, "Distribution of inspiratory and expiratory respiratory sound intensity on the surface of the human thorax," in *Proceedings of the 19th Annual International Conference of the IEEE Engineering in Medicine and Biology Society.'Magnificent Milestones and Emerging Opportunities in Medical Engineering'(Cat. No. 97CH36136)*, vol. 5, pp. 2047–2050, IEEE, 1997.

[14] H. A. Mansy, S. J. Hoxie, W. H. Warren, R. A. Balk, R. H. Sandler, and H. A. Hassaballa, "Detection of pneumothorax by computerized breath sound analysis," *Chest*, vol. 126, no. 4, p. 881S, 2004.

[15] M. Kompis, H. Pasterkamp, and G. R. Wodicka, "Acoustic imaging of the human chest," *Chest*, vol. 120, no. 4, pp. 1309–1321, 2001.

[16] M. Ozer, S. Acikgoz, T. Royston, H. Mansy, and R. Sandler, "Boundary element model for simulating sound propagation and source localization within the lungs," *The Journal of the Acoustical Society of America*, vol. 122, no. 1, pp. 657–671, 2007.

[17] B. Henry and T. J. Royston, "Localization of adventitious respiratory sounds," *The Journal of the Acoustical Society of America*, vol. 143, no. 3, pp. 1297–1307, 2018.

[18] S. A. Salehin and T. D. Abhayapala, "Lung sound localization using array of acoustic sensors," in *2008 2nd International Conference on Signal Processing and Communication Systems*, pp. 1–5, IEEE, 2008.

[19] R. P. Dellinger, J. E. Parrillo, A. Kushnir, M. Rossi, and I. Kushnir, "Dynamic visualization of lung sounds with a vibration response device: a case series," *Respiration*, vol. 75, no. 1, pp. 60–72, 2008.

[20] T. M. Maher, M. Gat, D. Allen, A. Devaraj, A. U. Wells, and D. M. Geddes, "Reproducibility of dynamically represented acoustic lung images from healthy individuals," *Thorax*, vol. 63, no. 6, pp. 542–548, 2008.

[21] I. Sen, M. Saraclar, and Y. P. Kahya, "Acoustic mapping of the lung based on source localization of adventitious respiratory sound components," in *2010 Annual International Conference of the IEEE Engineering in Medicine and Biology*, pp. 3670–3673, IEEE, 2010.

[22] H. M. Zaeim, C. Scheffer, M. Blanckenberg, and K. Dellimore, "Evaluation of the use of frequency response in the diagnosis of pleural effusion on a phantom model of the human lungs," in *2014 36th Annual International Conference of the IEEE Engineering in Medicine and Biology Society*, pp. 3418–3421, IEEE, 2014.

[23] T. Royston, X. Zhang, H. Mansy, and R. Sandler, "Modeling sound transmission through the pulmonary system and chest with application to diagnosis of a collapsed lung," *The Journal of the Acoustical Society of America*, vol. 111, no. 4, pp. 1931–1946, 2002.

[24] K. Horsfield, G. Dart, D. E. Olson, G. F. Filley, and G. Cumming, "Models of the human bronchial tree.," *Journal of applied physiology*, vol. 31, no. 2, pp. 207–217, 1971.

[25] W. Park, E. A. Hoffman, and M. Sonka, "Segmentation of intrathoracic airway trees: a fuzzy logic approach," *IEEE transactions on medical imaging*, vol. 17, no. 4, pp. 489–497, 1998.

[26] D. Aykac, E. A. Hoffman, G. McLennan, and J. M. Reinhardt, "Segmentation and analysis of the human airway tree from three-dimensional x-ray ct images," *IEEE transactions on medical imaging*, vol. 22, no. 8, pp. 940–950, 2003.

[27] M. H. Tawhai, P. Hunter, J. Tschirren, J. Reinhardt, G. McLennan, and E. A. Hoffman, "Ct-based geometry analysis and finite element models of the human and ovine bronchial tree," *Journal of applied physiology*, vol. 97, no. 6, pp. 2310–2321, 2004.

[28] Y. Peng, Z. Dai, H. A. Mansy, R. H. Sandler, R. A. Balk, and T. J. Royston, "Sound transmission in the chest under surface excitation: an experimental and

computational study with diagnostic applications," *Medical & biological engineering & computing*, vol. 52, no. 8, pp. 695–706, 2014.

[29] H. Mansy, T. Royston, R. Balk, and R. Sandler, "Pneumothorax detection using pulmonary acoustic transmission measurements," *Medical and Biological Engineering and Computing*, vol. 40, no. 5, pp. 520–525, 2002.

[30] Z. Dai, Y. Peng, B. M. Henry, H. A. Mansy, R. H. Sandler, and T. J. Royston, "A comprehensive computational model of sound transmission through the porcine lung," *The Journal of the Acoustical Society of America*, vol. 136, no. 3, pp. 1419–1429, 2014.

[31] W. Whewell, *History of the inductive sciences: from the earliest to the present times*, vol. 1. D. Appleton, 1859.

[32] B. P. Hildebrand, *An introduction to acoustical holography*. Springer Science & Business Media, 2013.

[33] M. G. Beghi, *Acoustic Waves: From Microdevices to Helioseismology*. BoD–Books on Demand, 2011.

[34] Y.-H. Kim, *Sound propagation: an impedance based approach*. John Wiley & Sons, 2010.

[35] C. U. Guide, "Structural mechanics module user's guide," *COMSOL Multiphysics*, vol. 5, p. 247, 2013.

[36] J. N. Reddy, *An introduction to continuum mechanics*. Cambridge university press, 2013.

[37] T. Yang and T. Yates, *Matched-beam processing: A synthesis of conventional beamforming and matched-field processing*. PhD thesis, Acoustical Society of America, 1996.

[38] P. Chiariotti, M. Martarelli, and P. Castellini, "Acoustic beamforming for noise source localization–reviews, methodology and applications," *Mechanical Systems and Signal Processing*, vol. 120, pp. 422–448, 2019.

[39] E. Sarradj, "Three-dimensional acoustic source mapping with different beamforming steering vector formulations," *Advances in Acoustics and Vibration*, vol. 2012, 2012.

[40] A. Malgoezar, *High Resolution Imaging of Noise from Novel Integrated Propeller Systems*. PhD thesis, Delft University of Technology, 2019.

[41] D. H. Johnson and D. E. Dudgeon, *Array signal processing: concepts and techniques*. Simon & Schuster, Inc., 1992.

[42] M. Mosher, "Phased arrays for aeroacoustic testing-theoretical development," in *Aeroacoustics Conference*, p. 1713, 1996.

[43] T. Brooks and W. Humphreys, Jr, "Effect of directional array size on the measurement of airframe noise components," in *5th AIAA/CEAS Aeroacoustics Conference and Exhibit*, p. 1958, 1999.

[44] P. Stoica, R. L. Moses, *et al.*, *Spectral analysis of signals*, vol. 452. Pearson Prentice Hall Upper Saddle River, NJ, 2005.

[45] C. S. Allen, W. K. Blake, R. P. Dougherty, D. Lynch, P. T. Soderman, and J. R. Underbrink, *Aeroacoustic measurements*. Springer Science & Business Media, 2002.

[46] T. Suzuki, "A review of diagnostic studies on jet-noise sources and generation mechanisms of subsonically convecting jets," *Fluid Dynamics Research*, vol. 42, no. 1, p. 014001, 2010.

[47] G. Chardon, "Theoretical analysis of beamforming steering vector formulations for acoustic source localization," *Journal of Sound and Vibration*, vol. 517, p. 116, 2022.

[48] D. A. Tolstoy, *Matched field processing for underwater acoustics*. World Scientific, 1993.

[49] T. B. Sarıkaya, "A comparative analysis of matched field processors for underwater acoustic source localization," Master's thesis, Middle East Technical University, 2010.

[50] W. Kai-ming, L. Qing, and W. Lixin, "Positioning ability comparison research on several matched-field processing methods with increasing white noise," in *2011 IEEE International Conference on Signal Processing, Communications and Computing (ICSPCC)*, pp. 1–5, IEEE, 2011.

[51] G. Zhu, Y. Wang, and Q. Wang, "Matched field processing based on bayesian estimation," *Sensors*, vol. 20, no. 5, p. 1374, 2020.

[52] J. Capon, R. J. Greenfield, and R. J. Kolker, "Multidimensional maximum-likelihood processing of a large aperture seismic array," *Proceedings of the IEEE*, vol. 55, no. 2, pp. 192–211, 1967.

[53] A. Tolstoy, “Review of matched field processing for environmental inverse problems,” *International Journal of Modern Physics C*, vol. 3, no. 04, pp. 691–708, 1992.

[54] P. S. Maharaj, R. Maheswaran, and A. Vasanthanathan, “Numerical analysis of fractured femur bone with prosthetic bone plates,” *Procedia Engineering*, vol. 64, pp. 1242–1251, 2013.

[55] A. V. Maurer, D. P. Enfrun, C.-O. Zuber, and R. Rozsnyo, “Biologic tissues properties deduction using an opto-mechanical model of the human eye,” in *Proceedings of COMSOL conference 2017, 18-20 October 2017, Rotterdam, The Netherlands*, no. CONFERENCE, 18-20 October 2017, 2017.

[56] I. Vovk, V. Grinchenko, and V. Oleinik, “Modeling the acoustic properties of the chest and measuring breath sounds,” *Acoustical physics*, vol. 41, no. 5, pp. 667–676, 1995.

[57] E. R. Weibel, A. F. Cournand, and D. W. Richards, *Morphometry of the human lung*, vol. 1. Springer, 1963.

[58] B. Henry and T. J. Royston, “A multiscale analytical model of bronchial airway acoustics,” *The Journal of the Acoustical Society of America*, vol. 142, no. 4, pp. 1774–1783, 2017.

[59] F. Dunn and W. J. Fry, “Ultrasonic absorption and reflection by lung tissue,” *Physics in Medicine & Biology*, vol. 5, no. 4, p. 401, 1961.

[60] S. Acikgoz, M. Ozer, T. Royston, H. Mansy, and R. Sandler, “Experimental and computational models for simulating sound propagation within the lungs,” *Journal of vibration and acoustics*, vol. 130, no. 2, 2008.

[61] C. Avigo, N. Di Lascio, P. Armanetti, C. Kusmic, L. Cavigli, F. Ratto, S. Meucci, C. Masciullo, M. Cecchini, R. Pini, *et al.*, “Organosilicon phantom for photoacoustic imaging,” *Journal of biomedical optics*, vol. 20, no. 4, p. 046008, 2015.

[62] S. H. Marwan, A. R. Bahari, M. F. Idham, H. A. Rahman, and M. Radzuan, “Analysis of polymethylmethacrylate as bone substitute of frontal human skull via finite element analysis,” *ARPN Journal of Engineering and Applied Sciences*, vol. 11, pp. 6200–3, 2016.

[63] COMSOL AB, “Comsol multiphysics.” `https://comsol.com`, Accessed: 07-Aug-2022.

[64] T. Łodygowski and W. Sumelka, "Limitations in application of finite element method in acoustic numerical simulation," *Journal of theoretical and applied mechanics*, vol. 44, no. 4, pp. 849–865, 2006.

[65] Malgoezar, AMN, "Acoustic beamforming." https://github.com/Anwar-M/Acoustic-Beamforming, Accessed: 07-Aug-2022.

[66] A. Malgoezar, M. Snellen, P. Sijtsma, and D. Simons, "Improving beamforming by optimization of acoustic array microphone positions," in *Proceedings of the 6th Berlin Beamforming Conference*, pp. 1–24, 2016.

[67] The MathWorks Inc., "Matlab 2020b, version: 9.9.0.123456." https://www.mathworks.com/products/matlab.html, Accessed: 07-Aug-2022.

[68] The US National Library of Medicine, "The visible human project." https://www.nlm.nih.gov/databases/download/vhp.html, Accessed: 07-Aug-2022.

[69] Materialise, "Mimics innovation suite 24." https://www.materialise.com/en/medical/mimics-innovation-suite/24, Accessed: 07-Aug-2022.

[70] Materialise, "3-matic 16." https://www.materialise.com/en/software/3-matic, Accessed: 07-Aug-2022.

[71] ANSYS, Inc, "Ansys icem cfd 14.5.7." https://www.ansys.com/academic, Accessed: 07-Aug-2022.

[72] Formlabs, "Form 3+: Industrial-quality desktop sla 3d printer." https://formlabs.com/3d-printers/form-3/, Accessed: 07-Aug-2022.

[73] Formlabs, "Material data sheet - flexible 50a." https://formlabs-media.formlabs.com/datasheets/2001420-TDS-ENUS-0.pdf, Accessed: 07-Aug-2022.

[74] Formlabs, "Material data sheet - standard." https://formlabs-media.formlabs.com/datasheets/Standard-DataSheet.pdf, Accessed: 07-Aug-2022.